

TKK Dissertations 38
Espoo 2006

**THIN-FILM DEPOSITION USING LASER ABLATION:
APPLICATION TO FERROMAGNETIC SHAPE-MEMORY
MATERIALS AND METHODS FOR SPATIAL SHAPING
OF LASER BEAMS**

Doctoral Dissertation

Antti Hakola



**Helsinki University of Technology
Department of Engineering Physics and Mathematics
Laboratory of Advanced Energy Systems**

TKK Dissertations 38
Espoo 2006

**THIN-FILM DEPOSITION USING LASER ABLATION:
APPLICATION TO FERROMAGNETIC SHAPE-MEMORY
MATERIALS AND METHODS FOR SPATIAL SHAPING
OF LASER BEAMS**

Doctoral Dissertation

Antti Hakola

Dissertation for the degree of Doctor of Science in Technology to be presented with due permission of the Department of Engineering Physics and Mathematics for public examination and debate in Auditorium F1 at Helsinki University of Technology (Espoo, Finland) on the 8th of September, 2006, at 12 noon.

**Helsinki University of Technology
Department of Engineering Physics and Mathematics
Laboratory of Advanced Energy Systems**

**Teknillinen korkeakoulu
Teknillisen fysiikan ja matematiikan osasto
Energiateet**

Distribution:

Helsinki University of Technology
Department of Engineering Physics and Mathematics
Laboratory of Advanced Energy Systems
P.O.Box 4100
FI - 02015 TKK
FINLAND
URL: <http://www.tkk.fi/Units/AES/>
Tel. +358-9-451 3198
Fax. +358-9-451 3195
E-mail: antti.hakola@tkk.fi

© 2006 Antti Hakola

ISBN 951-22-8282-8
ISBN 951-22-8283-6 (PDF)
ISSN 1795-2239
ISSN 1795-4584 (PDF)
URL: <http://lib.tkk.fi/Diss/2006/isbn9512282836/>

TKK-DISS-2161

Otamedia Oy
Espoo 2006



HELSINKI UNIVERSITY OF TECHNOLOGY P.O. BOX 1000, FI-02015 TKK http://www.tkk.fi	ABSTRACT OF DOCTORAL DISSERTATION
Author	
Name of the dissertation	
Date of manuscript	Date of the dissertation
Monograph	Article dissertation (summary + original articles)
Department	
Laboratory	
Field of research	
Opponent(s)	
Supervisor (Instructor)	
Abstract	
Keywords	
ISBN (printed)	ISSN (printed)
ISBN (pdf)	ISSN (pdf)
ISBN (others)	Number of pages
Publisher	
Print distribution	
The dissertation can be read at http://lib.tkk.fi/Diss/	



TEKNILLINEN KORKEAKOULU PL 1000, 02015 TKK http://www.tkk.fi		VÄITÖSKIRJAN TIIVISTELMÄ	
Tekijä Antti Hakola			
Väitöskirjan nimi Thin-Film Deposition Using Laser Ablation: Application to Ferromagnetic Shape-Memory Materials and Methods for Spatial Shaping of Laser Beams			
Käsikirjoituksen jättämispäivämäärä 13.3.2006		Väitöstilaisuuden ajankohta 8.9.2006	
<input type="checkbox"/> Monografia		<input checked="" type="checkbox"/> Yhdistelmäväitöskirja (yhteenvedo + erillisartikkelit)	
Osasto	Teknillinen fysiikka ja matematiikka		
Laboratorio	Energiatieteet		
Tutkimusala	Ohutkalvojen kasvatus laserablaatiolla sekä lasersäteiden muokkaus		
Vastaväittäjä(t)	Professori Peter E. Dyer		
Työn valvoja	Professori Rainer Salomaa		
(Työn ohjaaja)	TkT Timo Kajava		
Tiivistelmä Ferromagneettiset muistimetalliyhdisteet, ennen kaikkea Ni-Mn-Ga-metalliseokset, ovat aktiivisesti tutkittuja materiaaleja, koska ne pystyvät muuttamaan palautuvasti muotoaan jopa 10 % ulkoisessa magneettikentässä. Tämä mahdollistaa uudentyyppisten toimilaitteiden ja anturien toteuttamisen. Tutkimus on tähän mennessä keskittynyt Ni-Mn-Ga:n bulkkiominaisuuksiin, mutta mikromekaanisten komponenttien tai jopa mikroskooppisten koneiden valmistamiseksi näistä materiaaleista olisi valmistettava ohutkalvoja. Laserablaatio on tehokas tapa kasvattaa hyvälaatuisia ohutkalvoja monikomponenttisista materiaaleista kuten Ni-Mn-Ga:sta. Laserablaatioon käytetään suuritehoisia laserpulseja siirtämään ainetta stoikiometrisesti kohtiolta kasvatusalustan pinnalle ohueksi kalvoksi. Väitöskirjassa kasvatettiin muutamien sadan nanometrin paksuisia Ni-Mn-Ga-kalvoja eri alustoille kuten piille, NaCl:lle ja pienille Ni-Mn-Ga-paloille ja optimoitiin kasvatusparametrit kuten alustan lämpötila ja laserpulssien energiatiheys kohtiolla, jotta syntyvät kalvot olisivat ferromagneettisia, kiderakenteeltaan halutunlaisia ja pinnaltaan mahdollisimman tasaisia. Lisäksi kehitettiin menetelmiä kalvon ja alustan irrottamiseksi toisistaan, jotta havaittaisiin muistimetalli-ilmiön kannalta välttämätön faasimuutos matalissa lämpötiloissa. Erityisen lupaavia tuloksia saatiin NaCl-alustoja käyttämällä: magnetoituma oli lähes 70 % bulkkiväitöskirjasta, alustan poistaminen onnistui helposti etsaamalla sitä isotrooppisesti vedellä ja vapautetuissa kalvoissa havaittiin merkkejä faasimuutoksesta noin -100 °C:ssa. Myös piille kasvatetut kalvot olivat voimakkaan ferromagneettisia, ja optimiparametreja käytettäessä pisararoiskeiden määrä kalvon pinnalla oli vähäinen. Tulokset osoittavat, että laserablaatio yhdistettynä kalvojen litografiseen kuviointiin on kilpailukykyinen teknologia ohutkalvopohjaisen muistimetallirakenteiden valmistuksessa. Laserablaatiota varten lasersäteiden intensiteettijakauman kohtiolla on oltava tasainen ja jyrkkäreunainen. Väitöskirjassa tämä toteutettiin diffraktiivisen optiikan avulla: periodiset diffraktiiviset elementit muuttivat käyttämämme eksimeerilaserin säteen halutunlaiseksi jakaumaksi positiivisen linssin polttotasoon. Tämä uudenlainen tapa muokata lasersäde pienentää merkittävästi laserablaatiolaitteistomme tehohäviöitä. Diffraktiivista optiikkaa käytettiin myös lähes hajaantumattomien, ns. Bessel-Gauss-säteiden tuottamiseen suoraan laserresonaattorissa. Lisäksi Bessel-tyyppisiä säteitä saatiin synnytettyä myös tietynlaisessa nestekiteessä tapahtuvan itseisfokusoitumisen seurauksena. Hajaantumattomat lasersäteet tarjoavat mahdollisuuden tarkkaan laserablaatioon sekä pienten rakenteiden kuvioimiseen ohutkalvoihin.			
Asiasanat laserablaatio, ferromagneettiset muotomuistimateriaalit, flat-top-jakauma, Bessel-Gauss-säde			
ISBN (painettu)	951-22-8282-8	ISSN (painettu)	1795-2239
ISBN (pdf)	951-22-8283-6	ISSN (pdf)	1795-4584
ISBN (muut)		Sivumäärä	116 s. + liit. 27 s.
Julkaisija Teknillinen korkeakoulu			
Painetun väitöskirjan jakelu Energiatieteet			
<input checked="" type="checkbox"/> Luettavissa verkossa osoitteessa http://lib.tkk.fi/Diss/2006/isbn9512282836			

Preface

The research summarized in this thesis has been carried out in the Advanced Energy Systems Laboratory at Helsinki University of Technology. The work has been made in close collaboration with the Optics and Molecular Materials Laboratory, the Laboratory of Physical Metallurgy and Materials Science, and the Laboratory of Biomedical Engineering of Helsinki University of Technology as well as with the Department of Physics of University of Joensuu.

I would like to thank my supervisor, Professor Rainer Salomaa, for providing me the possibility to work in the laboratory and continue experimental research work with lasers after I had completed my master's thesis and had only a vague thought of obtaining a doctoral degree some day. Dr. Timo Kajava has been my instructor ever since I came to Miilu as a summer student in 1999. I warmly thank Timo for his guidance and support during all these years. I am particularly indebted to him for our long discussions which provided us with several interesting ideas and new directions into which we could proceed.

I am also grateful to Professor Jari Turunen and Dr. Kari Ullakko for their contributions to this work: they are both men full of ideas that just wait for their realization. I acknowledge Professor Matti Kaivola for organizing me funding from the Graduate School of Modern Optics and Photonics for my doctoral studies and giving me the opportunity to use the experimental facilities in Micronova after the Optics and Molecular Materials Laboratory moved there in 2004. I also thank all my colleagues and friends with whom I have had the pleasure to work during the past six years: Scott Buchter, Henna Elfström, Oleg Heczko, Antti Jaakkola, Ville Kekkonen, Andriy Shevchenko, Outi Söderberg, and all the other people, present and former, working in Miilu and in Micronova. Furthermore, I express my gratitude to all the members of the Advanced Energy Systems Laboratory, especially to Taina Kurki-Suonio, for the pleasant working atmosphere and the opportunity to be involved in teaching and course planning.

Financial support from the Graduate School of Modern Optics and Photonics, Jenny and Antti Wihuri Foundation, the Finnish Academy of Science and Letters, Vilho, Yrjö, and Kalle Väisälä Foundation, Tekniikan Edistämmissäätiö, the Finnish Society of Sciences and Letters, Magnus Ehrnrooth Foundation, and Artturi and Aina Helenius Foundation of the Finnish Cultural Foundation is gratefully acknowledged.

Finally, I acknowledge the support and encouragement that I have received from my parents and sisters.

Espoo, March 2006

Antti Hakola

List of publications

This thesis is a review of the author's work on pulsed laser deposition of Ni–Mn–Ga thin films and laser-beam shaping. It consists of an overview and the following selection of the author's publications in peer-reviewed journals:

- I. A. Hakola, O. Heczko, A. Jaakkola, T. Kajava, and K. Ullakko, "Pulsed laser deposition of Ni–Mn–Ga thin films on silicon," *Applied Physics A* **79**, 1505–1508 (2004).
- II. A. Hakola, O. Heczko, A. Jaakkola, T. Kajava, and K. Ullakko, "Ni–Mn–Ga films on Si, GaAs, and Ni–Mn–Ga single crystals by pulsed laser deposition," *Applied Surface Science* **238**, 155–158 (2004).
- III. A. Hakola, O. Heczko, A. Jaatinen, V. Kekkonen, and T. Kajava, "Substrate-free structures of iron-doped Ni–Mn–Ga thin films prepared by pulsed laser deposition," Report TKK-F-A844 (2006), submitted to *Journal of Physics, Conference Series* (peer-reviewed, recommended for publication).
- IV. A. Hakola, T. Kajava, H. Elfström, J. Simonen, P. Pääkkönen, and J. Turunen, "Diffractive shaping of excimer-laser beams for pulsed laser deposition," Report TKK-F-A843 (2006), accepted for publication in *Optics Communications*.
- V. A. Hakola, S. C. Buchter, T. Kajava, H. Elftröm, J. Simonen, P. Pääkkönen, and J. Turunen, "Bessel–Gauss output beam from a diode-pumped Nd:YAG laser," *Optics Communications* **238**, 335–340 (2004).
- VI. A. Hakola, A. Shevchenko, S. C. Buchter, M. Kaivola, and N. V. Tabiryan, "Creation of a narrow Bessel-like laser beam using a nematic liquid crystal," *Journal of the Optical Society of America B* **23**, 637–641 (2006).

Author's contribution

The research presented in this thesis is the result of the work carried out in the laser group of the Advanced Energy Systems Laboratory at Helsinki University of Technology during the years 2001–2006. The research work was made in close collaboration with the Optics and Molecular Materials Laboratory, the Laboratory of Physical Metallurgy and Materials Science, and the Laboratory of Biomedical Engineering of Helsinki University of Technology as well as with Professor Turunen's group at the Department of Physics of University of Joensuu. Therefore, all the selected publications have one or more co-authors but the author has played a central role in each of them.

The author has been responsible for the planning and implementation of the research in Papers I—III. Together with his co-authors, he has made all the deposition experiments and measurements reported in these Papers, and his role has been crucial in analyzing the results. He has taken part in the design and construction of the beam-shaping systems, laser resonators, and imaging setups described in Papers IV–VI, and he has carried out the measurements and the analysis of the experimental data. He has written Papers I—III and VI and has significantly contributed to the writing of Papers IV and V. He has also presented the work covered in this thesis in several international conferences.

Other publications by the author or to which the author has contributed:

- A. Shevchenko, A. Hakola, S. C. Buchter, M. Kaivola, and N. V. Tabiryan, "Laser beam shaping using self-focusing in a nematic liquid crystal," *Mol. Cryst. Liq. Cryst.* **454**, 217[619] (2006).
- A. Hakola and T. Kajava, "Finger on the pulse in thin film," *Physics World* **19** (6), supplement issue on Vacuum Challenges and Solutions: Advanced Materials, pp. 11–12 (2006).
- A. Hakola, S. C. Buchter, T. Kajava, H. Elfström, J. Simonen, P. Pääkkönen, and J. Turunen, "CW and pulsed operation of a diode-pumped Bessel–Gauss laser," *Proc. CLEO/Europe-EQEC 2005 Int. Conf., Europhysics Conference Abstracts* **29B** (Munich, Germany, 2005), p. CA7-3-THU.

Abbreviations

AR	Anti reflection
bcc	Body-centered cubic
CW	Continuous wave
DC	Direct current
EDS	Energy dispersive spectroscopy
fcc	Face-centered cubic
FSM	Ferromagnetic shape memory
FWHM	Full width half maximum
GSM	Gaussian Schell model
HR	High reflectivity
IR	Infrared
LED	Light emitting diode
MBE	Molecular beam epitaxy
MFIS	Magnetic field induced strain
Ni–Mn–Ga	$\text{Ni}_{2+x-y}\text{Mn}_{1-x}\text{Ga}_{1-y}$
PLD	Pulsed laser deposition
sc	Simple cubic
SEM	Scanning electron microscope
SM	Shape memory
T_C	Curie temperature
T_M	Martensitic transformation temperature
TEM	Transmission electron microscope
UV	Ultraviolet
VSM	Vibrating sample magnetometer
YAG	$\text{Y}_3\text{Al}_5\text{O}_{12}$, yttrium aluminium garnet
YBCO	$\text{YBa}_2\text{Cu}_3\text{O}_{7-\delta}$, yttrium barium copper oxide
YLF	YLiF_4 , yttrium lithium fluoride
YVO_4	Yttrium orthovanadate

Contents

1	Introduction	1
2	Ferromagnetic shape-memory materials	5
2.1	Fundamentals of magnetism and magnetic materials	5
2.2	Shape-memory effect	12
2.3	Ferromagnetic shape-memory effect	16
2.4	Properties of ferromagnetic shape-memory alloys	19
2.4.1	Ni–Mn–Ga alloys	19
2.4.2	Ni–Mn–Ga–Fe alloys	22
2.5	Applications of FSM alloys	23
2.6	Thin films of Ni–Mn–Ga	24
3	Pulsed laser deposition of Ni–Mn–Ga films	27
3.1	Interaction of laser pulses with matter	28
3.2	Plume formation and propagation	31
3.3	Film condensation	32
3.3.1	Different growth modes	32
3.3.2	Particulates on the film surface	34
3.4	Laser-beam shaping for the PLD process	35
3.5	Experimental	38
3.5.1	Equipment	38
3.5.2	Deposition process	40
3.5.3	Film characterization	42
3.5.4	Results	43

4	Laser-beam shaping	55
5	Diffractive shaping of excimer-laser beams	57
5.1	Theoretical basis	57
5.2	Periodic beam-shaping elements	61
5.3	Experimental results	63
6	Creation of propagation-invariant laser beams	69
6.1	Propagation-invariant beams	69
6.2	Methods to realize propagation-invariant beams	71
6.3	Bessel–Gauss beams from a laser resonator	73
6.3.1	Resonator design	73
6.3.2	Experimental setup	74
6.3.3	Results	77
6.4	Generation of Bessel-like laser beams in liquid crystals	81
6.4.1	Theory	81
6.4.2	Experimental	83
7	Conclusions	87

Chapter 1

Introduction

The invention of laser in 1960 has had a huge impact on many branches of science but also on everyday life. Just 20 years ago, few people had heard anything of CD and DVD players, laser pointers, bar-code readers, or broadband internet networks — things that we now take for granted. Lasers have become so common that most of us are unaware of the original meaning of the word itself and what actually makes laser such a versatile tool. "Laser" is an acronym for Light Amplification by Stimulated Emission of Radiation. These words imply that when a material having a suitable energy-level scheme is enclosed in a resonating cavity, the radiation incident on it is coherently amplified by an induced interaction process. The output radiation of a laser has several interesting properties that differentiate it from conventional light beams [1].

Laser beams are monochromatic, coherent, and bright, and typically they have a Gaussian transverse intensity distribution. Furthermore, the beam is highly directional, and it can be focused to a spot whose size is of the order of the laser wavelength. This makes it possible to obtain high energy or power densities in a small volume, which are necessary requirements for efficient processing of materials. In particular, by using short laser pulses with a duration ranging from nanoseconds to only a few femtoseconds and focusing them into a μm^2 -sized spot, the power density can be $10^5 - 10^{13} \text{ W/cm}^2$ [2]. Such values are sufficient for melting and vaporizing most materials, which has made high-power lasers attractive alternatives in drilling, welding, and cutting applications [2]. By using petawatt lasers, even higher peak irradiances, $10^{20} - 10^{21} \text{ W/cm}^2$, are possible [3]. By comparison, the laser pulses used in this work had a power density of $10^8 - 10^9 \text{ W/cm}^2$.

Melting and vaporization are two examples of the many ways how laser beams can interact with materials. If the energy density of the applied laser pulses, fluence (J/cm^2), exceeds a certain material-dependent threshold value, the absorption of the

laser-beam energy leads to an ejection of particles from a thin surface layer. This interaction process is called ablation, and the whole technique to remove material in a layer-by-layer fashion is known as laser ablation [2,4]. At the moment, the most actively studied application areas of laser ablation include eye surgery and surgery in general [5], micromachining in engineering and in biology [5–7], micro- and nano-structuring and accurate lithographic patterning of, e.g., glass and thin films [8–10], conservation of old paintings and sculptures [11], cleaning of surfaces for component fabrication [12], synthesis of novel materials such as carbon nanotubes [13], and deposition of thin films of different materials [14–16].

The preparation of thin films using laser ablation is referred to as pulsed laser deposition (PLD). In PLD, the emitted particles are collected on the surface of a substrate, and after a few hundreds or thousands of laser pulses, a thin film with a thickness of the order of a hundred nanometers is formed. A proper film growth requires that the ablation process takes place in a vacuum chamber where the emitted particle jet can freely expand or where its velocity distribution can be shaped in a controlled way. The main advantage of PLD over conventional techniques to prepare thin films is that the material is stoichiometrically transferred from the target to the substrate. In addition, the technique can be applied to a wide variety of materials — metals, insulators, superconductors, polymers, bones and teeth, and even soft biomaterials such as living cells and proteins — and it is possible to use background gases, e.g., O₂ with oxide materials, during the deposition process [14]. Pulsed laser deposition is particularly attractive in the case of multi-component materials that are difficult to process into thin-film form by other methods. Examples of these materials include ceramic high-temperature superconductors such as YBa₂Cu₃O_{7-δ} (YBCO) discussed, e.g., in Ref. [17], and ferromagnetic shape-memory materials such as Ni–Mn–Ga alloys. Ni–Mn–Ga represents a new class of "smart" materials that have recently gained much research interest, in particular in thin-film form.

In the first part of this thesis, the preparation of thin films of Ni–Mn–Ga alloys by the PLD technique is discussed. Chapter 2 deals with the fundamentals of ferromagnetism and the shape-memory effect, and presents the key physical properties of Ni–Mn–Ga. Chapter 3 concentrates on the deposition of the films. At first, the different phases of the PLD process — interaction of laser pulses with the target material, plume formation and propagation, and film condensation — are reviewed. The rest of chapter 3 (section 3.5) is devoted to the actual deposition experiments and the discussion of the achieved results. The main goal is to show that it is possible to use PLD to prepare smooth, ferromagnetic Ni–Mn–Ga films with the desired crystal structure and a saturation magnetization comparable to that of bulk Ni–Mn–Ga. Different substrate materials are studied to find out the best one for proper film growth. In addition, methods to release the film and the substrate totally or partially from each other are developed and tested in practice. All the above-mentioned as-

pects are necessary pre-requirements for the occurrence of the ferromagnetic shape-memory effect and for the future fabrication of microscopic shape-memory devices. The most important results of this research have been reported in Papers I–III.

The Gaussian transverse intensity profile is one of the advantageous properties of laser beams: the intensity is peaked at the center, the divergence is low, and the beam propagation can be described by rather simple formulae. However, there are a number of applications that would benefit from non-Gaussian beams. Some require uniform intensity distribution over a large area (so-called flat-top profiles) whereas others benefit from a narrow beam which spreads negligibly upon propagation. Laser ablation is a good example of an application where a narrow and homogeneous intensity distribution with steep edges is preferred to a focused Gaussian beam. In PLD, this guarantees a constant and well-defined fluence over the whole laser spot on the target, leads to stoichiometric removal of material, but also eliminates the detrimental effect of spatial pulse-to-pulse fluctuations on the surface roughness and composition of the deposited films [18–20]. Improving the homogeneity of laser pulses has attracted much research interest during the past few years, and good approximations of the desired flat-top distributions have been obtained. Techniques based on diffractive optics are perhaps the most efficient alternatives to realize flat-top and other non-Gaussian profiles, especially in the case of a partially coherent source such as an excimer laser [21].

The narrow propagation-invariant beams, so-called Bessel beams, have been in the frontier of optics since their discovery in the late 1980's [22]. Ideal Bessel beams have exactly the same intensity distribution in every transverse plane but since they are infinite in size and by their energy content, only finite-range approximations of such beams can be realized in practice. Several methods to create approximate Bessel fields such as Bessel-Gauss beams have been suggested but so far only a few experimental demonstrations have been reported and no commercial applications for the beams have emerged, yet [22–24]. Diffractive optics provides a solution also to this beam-shaping problem in the form of a laser resonator whose output beam is the exact Bessel-Gauss beam [25]. An equally competitive alternative is the creation of almost propagation-invariant beams in certain liquid crystals as a result of the self-focusing of Gaussian laser beams [26]. When the technical problems related to the production of Bessel-type fields have been solved, such beams will be of interest in precise alignment and metrology [27], manipulating the motion of small particles, e.g., in optical tweezers [28], and in laser machining of materials [29]. Thus, the beam-shaping techniques presented in this paragraph have a close connection with laser ablation.

The second part of this work is devoted to laser-beam shaping. In chapter 4, beam shaping is discussed in general and in chapter 5, the production of flat-top profiles from an excimer-laser beam using periodic diffractive elements is discussed both

in theory and in practice. The aim is to show that diffractive optics provides an effective way to realize the desired intensity distribution in the target plane. The promising results have been published in Paper IV. In addition, in Paper III, the generated flat-top beams are applied to pattern small structures in the deposited Ni–Mn–Ga films. Chapter 6 deals with the creation of propagation-invariant beams both directly in a laser resonator (Paper V) and in liquid crystals (Paper VI). The main goals are to demonstrate that both methods are equally competitive in generating Bessel-type beams and Q -switched pulses with a long propagation-invariant range and that the studied techniques make it possible to adjust the properties of the beams such as the width of the central region and the length of the focal line.

Chapter 2

Ferromagnetic shape-memory materials

This chapter gives a review of ferromagnetism and shape-memory materials. The concepts and definitions introduced below are needed when analyzing the experimental data, in particular, the measured magnetization curves of Ni–Mn–Ga films deposited by the PLD technique.

2.1 Fundamentals of magnetism and magnetic materials

The word "magnet" comes from *Magnesia*, an ancient town in Asia Minor, which was famous for the magnetic ores, such as *magnetite* (Fe_3O_4), it supplied for the whole world of Antiquity. The Chinese, however, are considered to be the first ones who actually made use of the magnetic properties of these *lodestones* and discovered the first magnetic phenomena: lodestones attracted iron but not tiles or copper. They also constructed the first compasses, which consisted of a spoon- or fish-shaped piece of magnetic material ("directional spoon" or "directional fish") balancing on a brass plate [30].

During the centuries several observations of magnetism and magnetic phenomena were made, e.g., that a magnet has two poles and that electric current can be used to generate magnetic fields. But it was only in 1865 that James Clerk Maxwell combined electricity and magnetism into a single theory, electromagnetism, by formulating a set of equations that coupled the electric and magnetic fields and the charge and current densities to each other. However, one had to wait the advent of quantum mechanics in the beginning of the 20th century before a microscopic

theory for magnetism was developed and the difference between, e.g., *dia-*, *para-* and *ferromagnetic* materials could be explained.

The key concept in describing the magnetic properties of materials is their magnetic dipole moment. An atom can be considered a small magnetic dipole, whose dipole moment \mathbf{m} is proportional to its total electronic angular momentum \mathbf{J} and the spectroscopic g factor, which depends on the quantum numbers of the orbital, spin, and total angular momenta. The quantity that describes to what extent a certain material is affected by an external magnetic field is called *magnetization*, and it is defined by the relation $\mathbf{M} = n\mathbf{m}$, where n is the density of magnetic dipole moments in a volume V . The magnetic dipole moments couple to the magnetic field and induce a torque $\boldsymbol{\tau} = \mathbf{m} \times \mathbf{B}$, where \mathbf{B} is the magnetic flux density. This shows that the dipole moments are preferably aligned with the magnetic field.

In vacuum, the relation between the flux density and the magnetic field, denoted by \mathbf{H} , is $\mathbf{B} = \mu_0\mathbf{H}$, where $\mu_0 = 4\pi \times 10^{-7} \text{ NA}^{-2}$ is the vacuum permeability. In a magnetic medium, one has to take into account also the magnetization, and the above-mentioned relation changes to $\mathbf{B} = \mu_0(\mathbf{H} + \mathbf{M})$. The permeability $\mu = \mu_0\mu_r$ of the material is defined such that $\mathbf{B} = \mu\mathbf{H}$. Assuming that the field and the magnetization are directly proportional to each other, i.e., $\mathbf{M} = \chi\mathbf{H}$, where χ is the magnetic susceptibility of the material, the relative permeability becomes $\mu_r = 1 + \chi$. The sign of χ determines whether the material is diamagnetic ($\chi < 0$) or paramagnetic ($\chi > 0$). Note that the field inside the material is different from the external field \mathbf{H}_0 , i.e., the total field is $\mathbf{H} = \mathbf{H}_0 + \mathbf{H}_d$, where $\mathbf{H}_d = -N\mathbf{M}$ is the demagnetizing field and N is the demagnetization factor.

In anisotropic materials, χ and N are generally tensors such that $\mathbf{M} = \overleftrightarrow{\chi} \mathbf{H}$ and $\mathbf{H}_d = -\overleftrightarrow{N} \mathbf{M}$. In the case of a uniformly magnetized ellipsoid, the demagnetization tensor \overleftrightarrow{N} is diagonal and the sum of the tensor components in the three orthogonal directions is $N_x + N_y + N_z = 1$ [31]. For a very prolate ellipsoid — which represents a thin film parallel to the magnetic field — the component $N_z \rightarrow 0$ along the major axis whereas for an extremely oblate ellipsoid — a film perpendicular to the magnetic field — $N_z \rightarrow 1$ along the short axis [31]. When this demagnetizing correction is taken into account, one obtains for the magnetization:

$$\mathbf{M} = \frac{\chi}{1 + N_z\chi} \mathbf{H}_0. \quad (2.1)$$

This formula is used when comparing the measured responses of thin films in the parallel and perpendicular directions with respect to the applied field.

For diamagnetic materials, the susceptibility is negative and typically very small: of the order of 10^{-5} . Actually, quantum mechanics predicts that diamagnetism

is present in any material but usually it is masked by the stronger forms of magnetism, paramagnetism and spontaneous magnetism such as ferromagnetism; only superconductors show perfect diamagnetism with $\chi = -1$. Diamagnetic materials do not have a net magnetic dipole moment but the response to the magnetic field is due to the non-vanishing expectation value of the second-order term in the electronic Hamiltonian and the corresponding second-order correction to the total energy. For paramagnetic materials, the susceptibility is positive but still relatively small: $10^{-5} - 10^{-3}$. Paramagnetic materials show a net magnetic dipole moment in an external magnetic field. However, Curie's law states that χ is inversely proportional to the temperature T [32]. The alignment of the magnetic dipoles is thus opposed by their thermal motion but favored by the field. At high fields but at moderate temperatures, a *saturation value* for the magnetization, M_S , is reached when all the dipole moments have been oriented with the field.

Ferromagnetic materials, on the other hand, favor long-range ordering of the magnetic dipoles even in the absence of the external field. Magnetic ordering is fundamentally caused by a quantum-mechanical exchange interaction between the spins of the neighboring atoms [30–32] and it is best manifested by the saturation of the magnetization at much more moderate fields than in the case of paramagnetic materials. *Magnetically soft materials* reach the saturation quickly at low fields whereas *magnetically hard materials* require much stronger fields to complete the magnetization process. Hard ferromagnets may also have a significant *remanent magnetization* M_r after the field is removed, and they are totally demagnetized only by applying a magnetic field oppositely oriented to the original field. The reverse field needed to restore M (or, more precisely, B) to zero is called the *coercive field* H_C ¹. For magnetically soft materials, $H_C \ll M_S$ implying that the magnetization processes such as the rotation of the magnetic dipoles occur at weak fields and the permeability $\mu = B/H$ as well as the magnetic susceptibility χ are high ($\chi \gg 1$). Magnetically hard materials, for their part, have a high coercive field H_C (and a high intrinsic coercivity H_{iC} as well). By cyclically varying the magnetic field between the extreme values $\pm H$ where $|H| > H_C$ (or, to be more accurate, $|H| > H_{iC}$), a hysteresis loop is formed as shown in Fig. 2.1. One should note, however, that the $M(H)$ curve of the material has a strong dependence on temperature as demonstrated in Fig. 2.2. As T increases, the curve becomes more and more linear and the saturation is reached at higher and higher fields until above a certain critical temperature, the *Curie temperature* T_C , the material has transformed to the paramagnetic state.

In some magnetically ordered material, the magnetic dipoles can couple in an anti-parallel configuration rather than in the parallel structure in ferromagnets. Macro-

¹Actually, the field that is required to restore M to zero is called the intrinsic coercive field H_{iC} . The two coercive fields differ from each other only in magnetically hard materials.

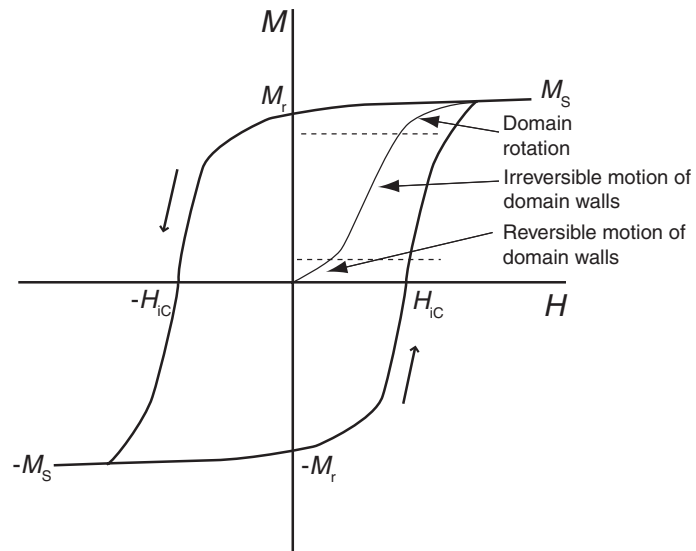


Figure 2.1: Hysteresis loop of a ferromagnetic material and the initial magnetization curve of a demagnetized specimen (thin line).

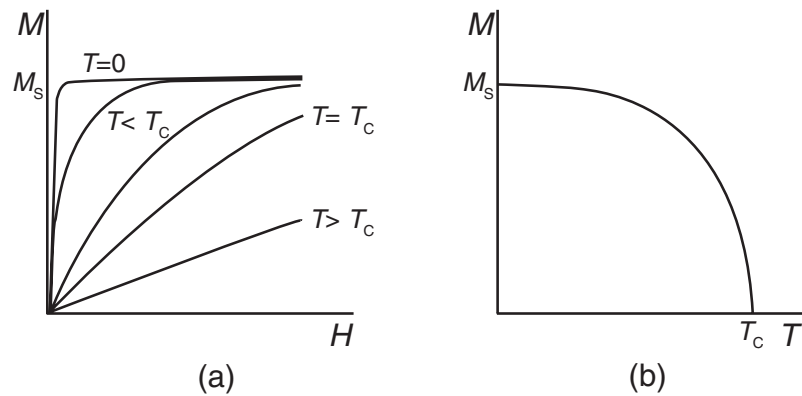


Figure 2.2: (a) Magnetization as a function of applied field at different temperatures. (b) Temperature dependence of the saturation magnetization.

scopically, these *antiferromagnetic* materials are similar to paramagnets but in the microscopic level, the negative exchange interaction between the neighboring spins opposes the aligning effect of the external magnetic field at low temperatures. This is manifested by an increase of $1/\chi$ as T decreases. Above the so-called *Néel temperature*, thermally induced disorder overcomes the exchange interaction and a paramagnetic state results. If the two sublattices are antiferromagnetically coupled but show unequal magnetizations, the material has a net magnetic dipole moment. At temperatures below the Curie temperature, these *ferrimagnetic* materials behave similarly to ferromagnets albeit the temperature dependence of $1/\chi$ is somewhat different.

Ferromagnetic materials spontaneously divide into *domains*. The density and size of these domains in a material is mainly determined by the balance between the magnetic dipolar energy E_M and the exchange-interaction energy E_{ex} of the atom spins of the sample². The former results from the interaction between the magnetic dipoles and it tends to demagnetize the sample: fewer aligned magnetic dipole moments minimize the energy of this dipolar interaction process. On the other hand, the exchange interaction favors dipoles that are parallel to each other. Since E_M dominates at large distances and E_{ex} is significant for neighboring atoms only, the total energy is minimized when the sample consists of μm -sized regions with a well-defined magnetization vector, i.e., in each domain the spontaneous magnetization has reached its saturation value. The magnetization vector points in the direction of some preferred crystallographic axis of the material but this direction changes from domain to domain.

The domains are separated by *domain walls* where the direction of the magnetization vector progressively changes from one orientation to another in order to minimize the cost in the exchange energy. If this was the only process one has to consider, the domain walls would broaden out to a thickness limited only by the dipolar interaction. However, the exchange interaction is not perfectly isotropic but depends also on the absolute orientations of the spins with respect to the crystal axes and to each other. Both the *anisotropy energy* connected to this interaction process and the exchange-interaction energy have to be taken into account when determining the wall thickness.

Suppose now that at zero field a ferromagnetic sample is initially in a demagnetized state. When the magnetic field is switched on, the domain walls start to move such that the volume of the domain in a favorable orientation with respect to the field increases. In magnetically soft materials, this process requires only a small amount of energy and, as a result, if the field is oriented along the so-called *easy axis of*

²In the case of closure domains, located close to the sample surface, the domain size is determined by the balance between the surface energy of the domain walls and the magnetoelastic energy of the domain.

magnetization, the saturation is reached at a very weak field. For any other direction, the domain-wall motion is followed by the rotation of the magnetization vector as illustrated in Fig. 2.1. The material has still a significant proportion of regions where the dipole moments are not parallel to the field, and to minimize the dipolar energy, the dipole moments are rotated away from the original easy directions of these regions. In particular, the rotation can be seen from the $M(H)$ curves measured along the *hard axes of magnetization*: initially, M increases rapidly due to the domain-wall motion but strong fields are required to complete the saturation. Hard ferromagnets reach the saturation at much higher fields than soft ferromagnets, and when the field is returned to zero, they also exhibit a large remanent magnetization as mentioned earlier in this section. This is due to the fact that the large number of defects in permanent magnets prevents the domain walls from moving back to their original configuration resulting in the hysteresis behavior observed in Fig. 2.1.

As stated in the previous paragraph, the magnetization vector tends to point in certain easy directions of magnetization. The magnetocrystalline anisotropy energy tells how much work is required to rotate \mathbf{M} away from one of these axes. In a uniaxial crystal the anisotropy energy is [30, 31]

$$E_{\text{anis}} = \sum_n K_{u,n} \sin^{2n} \theta \approx K_{u,0} + K_{u,1} \sin^2 \theta + K_{u,2} \sin^4 \theta, \quad (2.2)$$

where the coefficients $K_{u,n}$ are called the uniaxial anisotropy constants and θ is the angle with respect to the crystal axis, commonly referred to as the c axis. In a material with cubic symmetry, the expression for the anisotropy energy is [30, 31]

$$E_{\text{anis}} \approx K_0 + K_1 (\alpha_1^2 \alpha_2^2 + \alpha_2^2 \alpha_3^2 + \alpha_3^2 \alpha_1^2) + K_2 (\alpha_1^2 \alpha^2 \alpha_3^2), \quad (2.3)$$

where K_i :s are the cubic anisotropy constants and α_i :s are the direction cosines of the magnetization along the coordinate axes. The anisotropy constants can be used to characterize the magnetic properties of materials. For example, if in a cubic material $K_1 > 0$, the easy axis of magnetization is parallel to the $(1\ 0\ 0)$ direction whereas in the case $K_1 < 0$, $(1\ 1\ 1)$ is the easy direction; the other directions in the family $(1\ 0\ 0)$, $(1\ 1\ 0)$, and $(1\ 1\ 1)$ are called the medium and the hard axes. In uniaxial materials, the condition $K_{u,1} > 0$ means that the c axis is the easy direction.

Materials with uniaxial symmetry represent the simplest class of magnetically anisotropic materials. When $K_{u,1} > 0$, the field applied along the easy c axis leads to the disappearance of the domain structure at low fields whereas in the case $\mathbf{H} \perp c$, the magnetization vector first rotates until the whole sample is in a single-domain state. The field required to complete this rotation is called the anisotropy field H_A (see Fig. 2.3), and it is thus a good measure for the strength of the magnetocrystalline anisotropy. This field can be solved by minimizing the total free energy

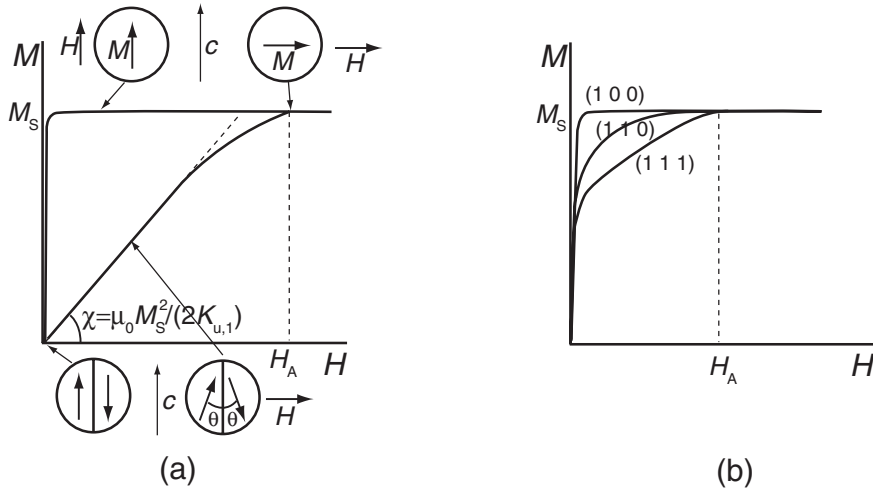


Figure 2.3: (a) Field dependence of magnetization in a uniaxial ferromagnetic material, where the c axis is the easy direction of magnetization. (b) Magnetization curves for a ferromagnetic material with cubic symmetry.

density of the material with respect to the angle θ . One obtains [30, 31]:

$$H_A = \frac{2K_{u,1} + 4K_{u,2}}{\mu_0 M_S} \approx \frac{2K_{u,1}}{\mu_0 M_S}. \quad (2.4)$$

This relation tells us that the anisotropy constants can be determined from the area between the $M(H)$ curves for the parallel and the perpendicular directions with respect to the field; the area is equal to $K_{u,1} + K_{u,2}$. The curves can also be used to determine the low-field susceptibility, and according to Ref. [30] it is $\chi = \mu_0 M_S^2 / (2K_{u,1})$.

In a cubic material, the area between the curves measured in the medium and the hard directions is $K_1/4$ and the anisotropy field is [30, 31]

$$H_A = \frac{2K_1}{\mu_0 M_S}. \quad (2.5)$$

A magnetic sample can change its size and shape slightly when subjected to a magnetic field. This effect is known as *magnetostriction*, and it is responsible, e.g., for the humming sound of transformers: pieces of iron elongate and contract at 50-Hz frequency. In the microscopic level, the phenomenon is due to the deformation of the crystal lattice when the field is turned on. The magnetostriction coefficient $\lambda = \Delta l/l$ depends on the direction of the applied field with respect to the magnetization but also on the measurement direction and the material anisotropy. Thus, generally λ is a tensor proportional to the stress tensor of the studied sample. The

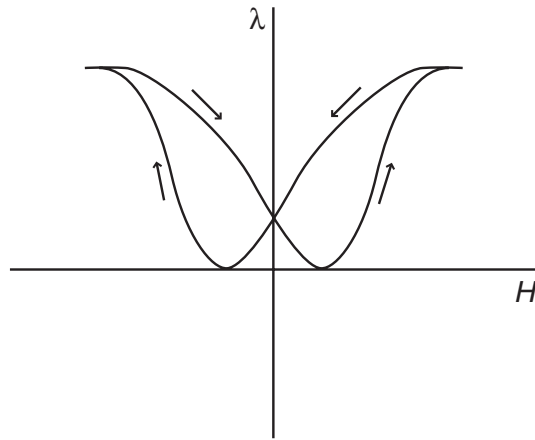


Figure 2.4: The hysteresis loop for the magnetostriction coefficient in the case $\lambda > 0$.

distortion is typically very small — of the order of $10^{-5} - 10^{-3}$ [31] — and it has a significant temperature dependence. The field dependence of λ is shown in Fig. 2.4 for an isotropic material and in the case $\lambda > 0$.

2.2 Shape-memory effect

Certain materials can exhibit large strains without plastic deformations when an external force is applied to them. In addition, the materials revert to their original state when the perturbation is removed [33]. A necessary condition for this *shape-memory effect* is that the so-called martensitic transformation of the crystal lattice takes place. In this phase transformation, the crystal structure changes from the parent, usually cubic *austenitic* phase to a lower-symmetry, often tetragonal or orthorhombic *martensitic* phase. If a shape-memory sample in the martensitic state is now deformed, its original shape can be restored by the reverse transformation process back to the parent phase. In other words, the material remembers what its shape was before the transformation process.

The martensitic transformation can be induced by decreasing the temperature of the material below a certain critical point, exerting stress on the sample, or subjecting it to an electromagnetic field; the last one applies for ferroelectric or ferromagnetic materials. This phase transformation is diffusionless, i.e., the chemical composition of the material does not change: only structural rearrangements occur in the crystal lattice. Thus, the process is reversible.

The transformation starts by the formation of martensitic regions in the parent phase. Since the lattice constants of the two phases are different, these regions

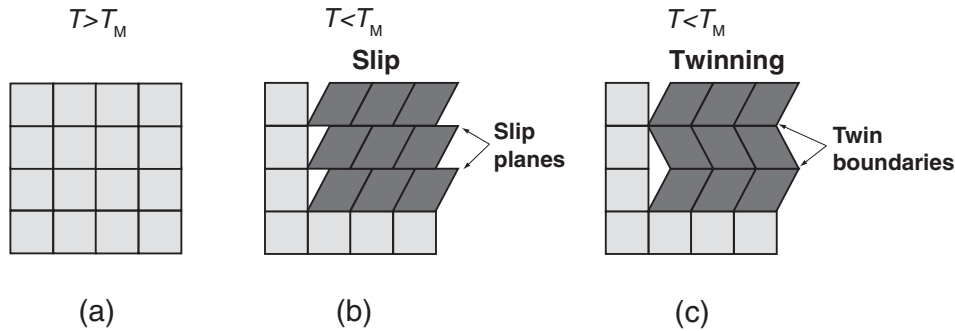


Figure 2.5: Schematic illustration of the nucleation of a martensitic region in the parent austenitic phase in (a). The strain associated with the martensitic transformation can be relieved by a slip (b) or by the formation of twin variants (c).

are distorted with respect to the surrounding lattice. This leads to a local strain — elongation or contraction — along some crystallographic direction. The martensitic planes may slip plastically or, more importantly, an ensemble of twin variants — or domains — separated by mobile twin boundaries is formed as illustrated in Figs. 2.5 and 2.6 [33, 34]. The latter process can also be regarded as a mirror-like stacking fault of neighboring atom layers. Usually, the motion of the twin boundaries is the easiest way for the sample to deform since, contrary to slipping, this process involves breaking fewer chemical bonds in the lattice and provides the clearest explanation to the macroscopic shape change [34].

In the temperature-driven shape-memory effect, the transformation begins at a temperature $T_{M,s}$ and ends at $T_{M,f}$; the start and finish temperatures for the reverse process are $T_{A,s}$ and $T_{A,f}$, respectively. As one clearly notices in Fig. 2.7, the transformation is hysteretic, i.e., $T_{A,f} > T_{M,s}$ implying that the reverse process occurs at a slightly different temperature than the original transformation. The width of this thermal-hysteresis loop depends on the amount of elastic and surface energies stored during the transformation and, generally, the narrower the loop, the easier it is to switch from one phase to another upon cooling or heating. Typically, the thermal hysteresis is of the order of 10 – 20 °C but for some alloys it can be almost 50 °C [33]. The transformation process is usually characterized by a single temperature $T_M = (T_{A,f} + T_{M,s}) / 2$, which corresponds to the thermodynamic point where the Gibbs' free energies of the different phases are equal.

The shape-memory behavior is manifested by first cooling the studied sample such that the transformation to the martensitic state takes place and then deforming it. After the sample is heated above $T_{A,f}$, its original shape is restored as illustrated in Fig. 2.8. This one-way shape-memory effect was discovered in 1951 in a gold alloy containing 47.5 at-% of cadmium but became of active interest only after similar

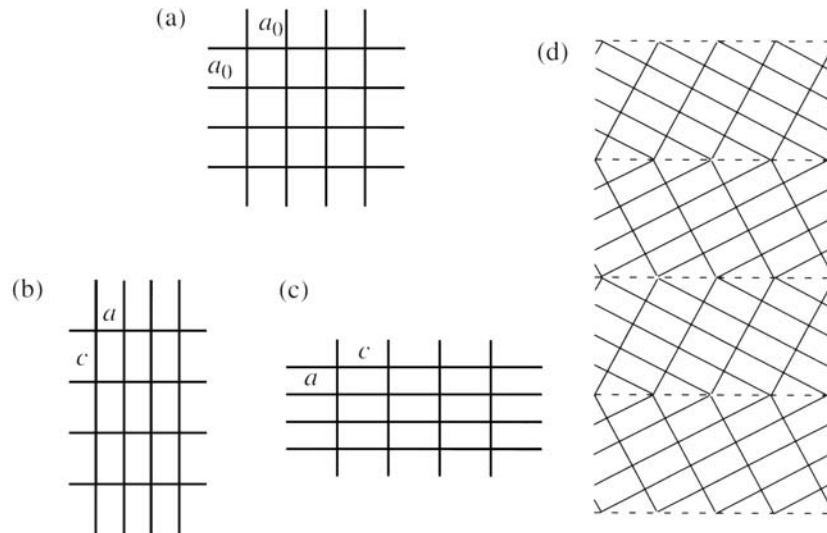


Figure 2.6: Formation of the twin structure in two dimensions. (a) The parent austenitic phase, (b),(c) two different martensitic variants, (d) regions of martensitic variants separated by twin boundaries [36].

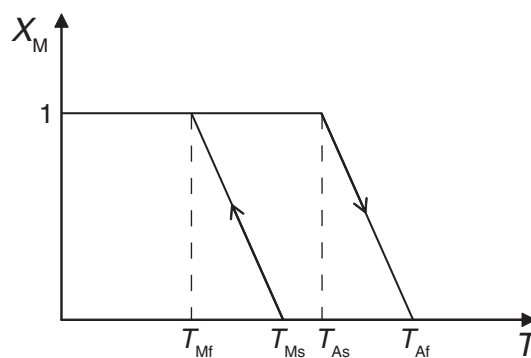


Figure 2.7: The molar fraction of the martensitic phase as a function of temperature.

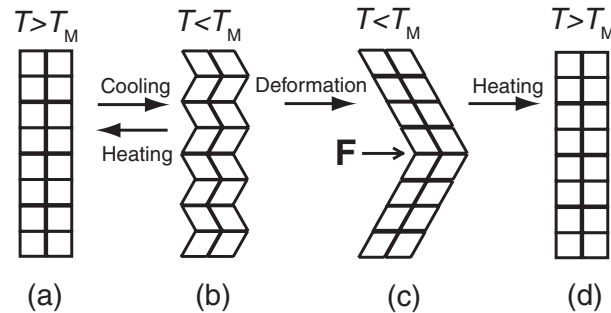


Figure 2.8: Schematic illustration of the temperature-driven shape-memory effect. (a) The parent phase, (b) formation of the twin structure below the martensitic transformation temperature, (c) deformation of the sample by an external force, (d) the original shape is restored upon heating to the parent phase.

behavior had been observed in Ni–Ti alloys [35]. Some shape-memory alloys under specific conditions can also return to the modified shape when recooled below the transformation temperature. This phenomenon is known as the two-way shape-memory effect [33].

In the stress-driven shape-memory effect, also known as superelasticity, a sufficiently strong external stress can induce transformation to the martensitic phase at temperatures well above T_M and lead to a macroscopic strain in the material (see Fig. 2.9). The reason for this behavior is that stress is most easily relieved by the formation of a twinned martensitic microstructure. When the stress is removed, the martensite transforms back to the parent phase and the original shape is restored [33,36].

The twin boundaries in the martensitic phase are highly mobile, which makes it possible to deform the sample easily. During the deformation process, the volume fraction of the twin variant exhibiting the largest strain in the direction of the external force grows at the expense of other variants. As the stress applied to the sample reaches a certain critical value, the twin boundaries start to move and, as a result, large strains are achieved with an approximately constant stress. The twin-boundary motion preserves the topological structure of the lattice, which also explains why in the temperature-driven shape-memory effect it is possible to return to the original state upon heating. The observed strains can be large, up to 8 % in Ni–Ti alloys, but the operating frequency is limited to 100 Hz due to the mechanical or thermal nature of the phenomenon [33,37,38]. Therefore, several attempts have been made to discover materials with a fast response to the external force and a high operating frequency.

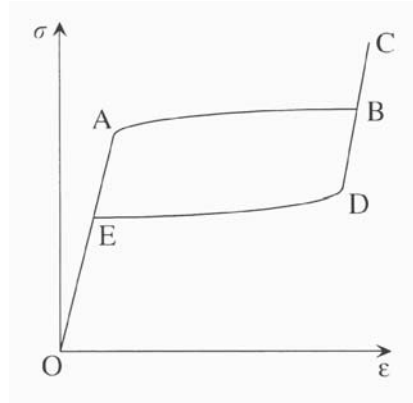


Figure 2.9: The stress–strain (σ – ϵ) curve of a superelastic material [36]. First, the strain increases as the external stress is increased. When the stress reaches its critical value at point A, the material transforms to the martensitic state and a large strain results (between A and B). When the stress is relieved, the martensite transforms back to the austenitic phase and the original shape of the sample is restored (between D and E). Similarly to the temperature-driven shape-memory effect, superelastic materials exhibit hysteretic behavior.

2.3 Ferromagnetic shape-memory effect

Ferromagnetic shape-memory (FSM) effect differs from the other shape-memory phenomena in that the rearrangement of the twin variants occurs in the martensitic phase: no phase transformations are required to induce the macroscopic shape changes. The FSM effect was first discovered by Ullakko and his co-workers [39] in 1996. They observed that a Ni_2MnGa sample experienced a 0.2-% strain in a 0.6-T magnetic field at 265 K — well below the martensitic transformation temperature.

To explain the FSM behavior, one has to take into account also the magnetic dipole moments of the twin variants. In the absence of magnetic field, the dipoles point in the directions of the easy axes of magnetization of the different twin variants. In a weak applied field, the dipole moments start to rotate to align the dipoles with the field but at stronger fields the twins are reorganized such that the proportion of the variant favorably oriented with respect to the field starts to increase (see Figs. 2.10 and 2.11). This latter mechanism is responsible for the observed macroscopic strain, the maximum value of which depends on the material and the crystal structure of the martensitic phase. Magnetic-field-induced strains (MFIS) of almost 10 % have been reported in martensitic $\text{Ni}_{48.8}\text{Mn}_{29.7}\text{Ga}_{21.5}$ [40].

The large MFIS observed in FSM alloys is theoretically modelled by several research groups in Refs. [34, 42–44], the last one being also a thorough review of the known ferromagnetic shape-memory materials. According to Likhachev and

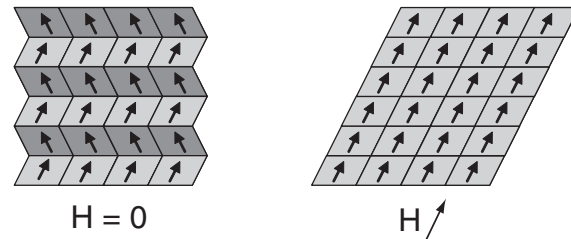


Figure 2.10: Redistribution of the twin variants in an applied magnetic field. In Ni–Mn–Ga the variant size in the multivariant state ($H = 0$) is approximately $100 - 200 \mu\text{m}$ whereas the size of the magnetic domains is $10 - 20 \mu\text{m}$ [41].

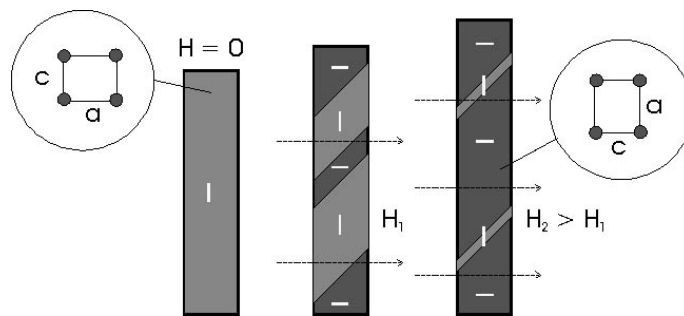


Figure 2.11: Left: An FSM sample consisting of a single martensitic variant at zero field. Center: When a magnetic field orthogonal to the orientation of the variant is applied, a new martensitic variant oriented parallel to the field is nucleated in the alloy. Right: As the field strength is increased, the proportion of this new variant increases and, simultaneously, the sample is elongated.

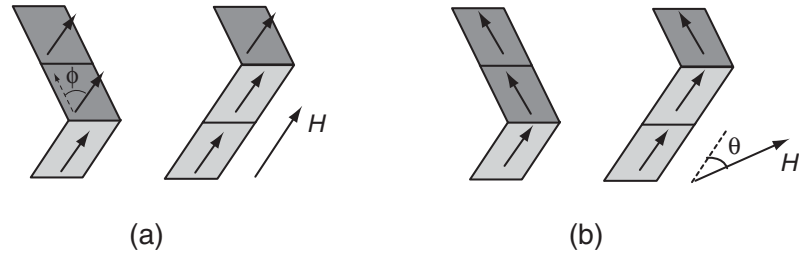


Figure 2.12: Mechanism for the twin-boundary motion driven by a magnetic field in the case of (a) weak and (b) strong martensitic anisotropy relative to the Zeeman energy.

Ullakko [43], the twin-boundary motion is possible if the magnetic-field-induced stress, $\sigma_M = K_u/e_0$, is larger than the critical stress at zero field, σ_{tw} , needed to transform the sample to a single-variant state. Here, K_u is the anisotropy constant of the martensitic phase and $e_0 = (1 - c/a)$, where c and a are the lattice constants of the (tetragonal) martensitic phase. All these parameters are functions of temperature, which means that the MFIS depends on temperature. This model has also been applied to explain how the stress σ_M depends on the magnetic field and what kind of field- and stress-dependence the actual strain, $e = \Delta l/l < e_0$, has.

In O’Handley’s [34] approach, the twin-boundary motion is connected to the magnetic anisotropy and saturation magnetization of the material by a dimensionless field parameter $h_A = M_S H / (2K_u)$. In the case of weak anisotropy, $h_A \gg 1$, and the magnetization vector of those variants unfavorably oriented with the field simply rotates and the saturation is readily reached. The driving force for the twin-boundary motion is now the magnetic anisotropy energy difference $\Delta E_{anis} = K_u \sin^2 \phi$, where ϕ is the angle between the easy axes of magnetization of the neighboring twins as illustrated in Fig. 2.12a. At the other extreme, the magnetic anisotropy is high and $h_A \ll 1$. In this case, the directions of the magnetization vectors are practically unaffected by the applied magnetic field and the twin boundaries start to move because of a large difference in the Zeeman energy $\Delta \mathbf{M} \cdot \mathbf{H}$ across the twin boundary as Fig. 2.12b shows; the magnetic anisotropy energy does not change during the process. O’Handley has also shown that in order to drive the sample most efficiently from one variant state to another, the magnetic field should be applied parallel to a twin boundary — not in the direction of the easy axis of magnetization of one of the adjoining variants. In O’Handley’s theory, the maximum output strain is obtained from a simple relation: $e/e_0 \approx M_S H / (2C e_0^2)$, where C is the stiffness constant of the material.

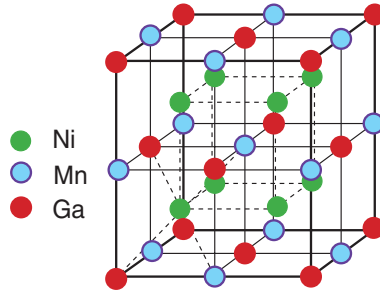


Figure 2.13: Crystal structure of the stoichiometric Ni_2MnGa in the austenitic phase.

2.4 Properties of ferromagnetic shape-memory alloys

2.4.1 Ni–Mn–Ga alloys

The FSM effect has been observed in many intermetallic or iron-based alloys. Examples include binary Fe–Pd, Fe–Pt, and Co–Ni as well as ternary Co–Ni–Ga and Co–Ni–Al and quaternary Fe–Ni–Co–Ti, but so far the most promising candidates are $\text{Ni}_{2+x+y}\text{Mn}_{1-x}\text{Ga}_{1-y}$ alloys which in this work are abbreviated to Ni–Mn–Ga [44]. Typically, the MFIS are of the order of 0.1 – 1 % in a cyclic magnetic field with a maximum value of approximately 1 T, but for Ni–Mn–Ga the strains can be much higher: from 1.8 to 9.5 % [40, 44]. This thesis concentrates on the properties of Ni–Mn–Ga alloys.

The stoichiometric Ni_2MnGa has been studied for decades together with other so-called *Heusler alloys* X_2YZ [45]. In the 1980's, Webster *et al.* [46] discovered that Ni_2MnGa undergoes martensitic transformation at low temperatures, which made it a potential shape-memory material. Finally, in 1996, Ullakko *et al.* [39] reported a 0.2 % MFIS in this alloy.

The parent austenitic phase of Ni–Mn–Ga has a cubic crystal structure. The Ni atoms can be thought to form a simple-cubic (sc) lattice while Mn and Ga atoms form a NaCl-like structure (face-centered cubic, fcc lattice). The two lattices interpenetrate such that each simple-cubic Ni unit cell encloses one Mn or Ga at its body-center cite according to Fig. 2.13. The lattice constant of Ni_2MnGa is $a_A = 0.5825$ nm at room temperature [44], whereas, e.g., for $\text{Ni}_{51.1}\text{Mn}_{28.4}\text{Ga}_{20.5}$, the corresponding value is $a_A = 0.5837$ nm at 373 K [47] and for $\text{Ni}_{49.7}\text{Mn}_{29.1}\text{Ga}_{21.2}$, the value of $a_A = 0.5840$ nm at 323 K has been determined [48].

The transformation to the martensitic phase can occur in several different ways. The

type of the martensite, its crystal structure, and the transformation temperature depend on the Ni/Mn/Ga ratio. The stoichiometric Ni_2MnGa has a tetragonal martensitic structure below $T_M = 202$ K with lattice parameters $a = b = 0.5920$ nm and $c = 0.5566$ nm [44]. Thus, the lattice is contracted such that $c/a = 0.94$. Other Ni–Mn–Ga structures show a variety of martensitic structures such as non-modulated tetragonal (T) martensite with $c/a > 1$, five-layer-modulated (5M) tetragonal and seven-layer-modulated (7M) orthorhombic structures with $c/a < 1$; the modulation means periodic deformation of the crystal lattice with periods of 5 or 7 atomic layers. The transformation temperature can be well above 300 K for these off-stoichiometric alloys. For example, the 7M $\text{Ni}_{50.5}\text{Mn}_{29.4}\text{Ga}_{20.1}$ has a T_M of 352 K and lattice constants of $a = 0.618$ nm, $b = 0.580$ nm, and $c = 0.552$ nm [49]. Both the martensitic transformation temperature as well as the Curie temperature for a wide range of Ni–Mn–Ga alloys can be found in Ref. [50].

The FSM alloys may exhibit intermartensitic transformations when cooled to temperatures well below T_M or when subjected to external stress. A typical transformation sequence is $P \rightarrow 5M \rightarrow 7M \rightarrow T$ or $P \rightarrow 7M \rightarrow T$, where P stands for the parent phase. For the $\text{Ni}_{50.5}\text{Mn}_{29.4}\text{Ga}_{20.1}$, the latter transformation takes place at 263 K [51]. One should note that the T phase is the most stable martensitic phase and, therefore, it exists at low temperatures. For many alloys, it is the only martensitic phase even above the Curie temperature T_C .

The martensitic state is systematically characterized by the average number of valence electrons per atom, n_v . It has been shown that the c/a ratio changes from > 1 to < 1 when $n_v \leq 7.7$ and that the T_M is below the Curie point when $n_v < 7.6$ [50]. In addition, the T_M is observed to increase and the T_C to decrease with growing n_v . Chernenko *et al.* [52] have studied a number of alloys and concluded that by keeping their Mn content constant, the T_M decreases as Ga is added in the alloy. In addition, with a fixed Ni content, the addition of Mn raises the T_M , and as the Ga content remains intact, the substitution of Ni with Mn lowers the T_M . The transformation temperature can thus be increased by carefully tailoring the Ni/Mn/Ga ratio of the alloy. The simultaneous decrease in T_C is explained by the fact that the magnetic dipole moment of the alloy is mainly due to Mn atoms: as the Mn concentration increases, these atoms couple antiferromagnetically such that only the Ni atoms determine the magnetic moment and the Curie temperature [53].

The maximum obtainable strain, e_0 , is of the order of 5 – 10 % for the 5M and 7M structures [54, 55] and up to 20 % for the T structure [54, 56]. In practice, the magnetically induced strains are lower than these theoretical values: 5.8 % for the 5M $\text{Ni}_{49.2}\text{Mn}_{29.6}\text{Ga}_{21.2}$ ($e_0 = 5.89$ %), 9.4 % for the 7M $\text{Ni}_{48.8}\text{Mn}_{29.7}\text{Ga}_{21.5}$ ($e_0 = 10.66$ %) but less than 0.02 % for the tetragonal $\text{Ni}_{52.1}\text{Mn}_{27.3}\text{Ga}_{20.6}$ ($e_0 = 20.5$ %) [54]. The reason for the very small strain response of the last alloy is that the estimated magnetic-field-induced stress, σ_M , is much smaller than the measured

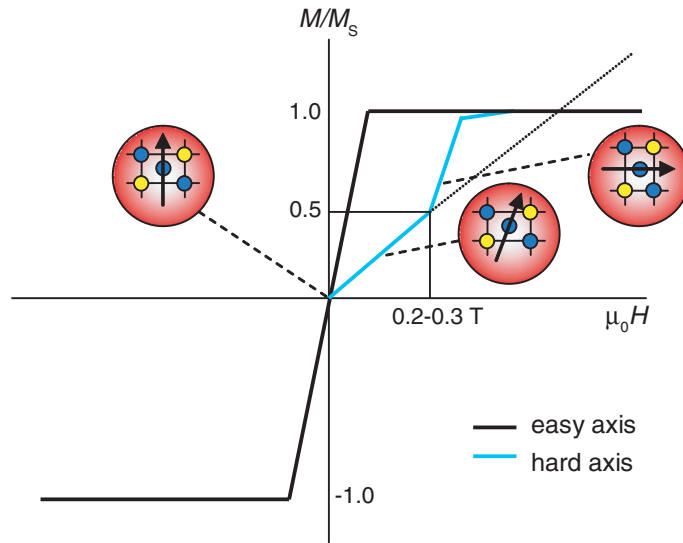


Figure 2.14: Schematic illustration of the magnetization of an FSM sample when applying the field along the easy and the hard axis. Before the process, the sample is assumed to be in a single-variant state.

twinning stress [54]. In order to induce the largest strains, the sample has first to be biased into a single-variant state in a static magnetic field or by subjecting it to a uniaxial stress. The onset of the FSM effect is observed as a jump of the magnetization in the first quadrant of the $M - H$ -curve. This behavior is illustrated in Fig. 2.14 [57, 58]. Typically, the threshold field is of the order of 0.2 – 0.3 T. In the reverse direction, the magnetization follows the path determined by the easy axis of the sample.

The magnetocrystalline anisotropy is one of the most important parameters that determines the occurrence of the FSM effect. The anisotropy constants can be obtained by measuring the magnetization curves for different orientations of the field with respect to the crystallographic axes of the material [49]. In tetragonal Ni–Mn–Ga, the easy axis of magnetization points either in the (1 0 0) or the (0 0 1) direction. For example, in the 5M structure with $a = b = 0.595$ nm and $c = 0.559$ nm, the magnetization saturates at approximately 0.5 T for $\mathbf{H} \perp c$ where c now stands for the easy direction. The zero-temperature value for the first anisotropy constant of this alloy is evaluated to be $K_{u,1} = 2.8 \times 10^5$ J/m³ [59]. The 7M alloy with $a = 0.618$ nm, $b = 0.580$ nm, and $c = 0.552$ nm has the easy (1 0 0), the mid-hard (0 1 0), and the hard (0 0 1) directions. In the hard direction, the saturation is reached at approximately 1 T, and from the measured curves one can determine for the values of the anisotropy constants at room temperature $K_1 = 1.7 \times 10^5$ J/m³ and $K_2 = 0.9 \times 10^5$ J/m³ [49]. Similar values have been obtained for other Ni–Mn–Ga

alloys.

Typically, the specific saturation magnetization of bulk Ni–Mn–Ga is 60–80 emu/g (in SI units, 60–80 Am²/kg) [49, 54–59], but this value depends largely on the composition and the temperature. An interesting result is that the saturation magnetization of the martensitic phase is higher than that of the austenitic phase. This difference in magnetizations gives rise to a large change in entropy during the transformation process and results in the so-called *giant magnetocaloric effect*: heating of the sample by adiabatic magnetization and cooling by adiabatic demagnetization — or vice versa [60].

2.4.2 Ni–Mn–Ga–Fe alloys

Practical applications of FSM materials would benefit from a high martensitic transformation temperature but, simultaneously, the Curie point should be as high as possible and the material should have a large saturation magnetization at the working temperatures. Several ternary and quaternary shape-memory alloys have been studied to meet the above-mentioned demands. Examples of these include Fe–Ni–Ga with the T_M of 150 – 300 K [47, 61] and Ni–Mn–Ga doped (or modified) with Bi, Pb, Si, Sn, or Zn [61], with lanthanoids Nd, Sm, or Tb [62], or, above all, with Fe [61, 63–67].

Kikuchi *et al.* [61] have observed that by replacing a small amount of Mn with Fe, the lattice constant as well as the T_M decrease linearly with the iron content. This is due to the fact that iron stabilizes the parent austenitic phase and makes transition to the martensitic state more unlikely. In addition, the thermal hysteresis of the transformation process increases as the relative proportion of the Fe atoms in the crystal structure grows. This is caused by an enhanced mobility of the twin boundaries. Simultaneously, the T_C increases since doping with iron leads to a stronger exchange interaction between the electron spins — albeit the magnetic dipole moment of the alloy decreases [61]. On the other hand, increasing the Ni content of the alloy raises its T_M up to 600 K but, as stated above, replacing atoms with Fe tends to decrease the transformation temperature. Therefore, the Ni/Mn/Ga/Fe composition has to be optimized to obtain large saturation magnetization at possibly high operating temperatures. For example, Koho *et al.* [66] have systematically studied the physical properties of several Ni–Mn–Ga–Fe alloys by varying the iron content between 0.7 and 11 % and concluded that with increasing Fe content, a high T_C was obtained when the Ni/Mn ratio was larger than 1.7.

In addition, for Fe-doped alloys the temperature dependence of the MFIS is enhanced. For instance, as the Fe content in Ni₅₂Mn_{24–x}Fe_xGa₂₄ increases from 0 to 8 %, the range of the MFIS within the temperature interval 160 – 300 K changes from 0.3 . . . 1.2 % to 0.7 . . . 1.1 % [67].

2.5 Applications of FSM alloys

All shape-memory (SM) alloys are good candidates for different actuator applications due to the large strains they can produce and due to their mechanical durability; Krulevitch *et al.* [37] have reported that Ni–Ti and Ni–Ti–Cu SM alloys can generate 2-% strains even after millions of cooling–heating cycles. The operating frequency of many conventional SM materials is, however, limited to approximately 100 Hz due to the thermal nature of the phase-transformation process, whereas FSM alloys have already been used in applications in the kHz regime [68]. In addition, actuators based on FSM alloys have a fast response — less than 0.2 ms — to the driving force and are able to generate large thrusts (for instance, 40 mm/s and 1 N for a linear motor) [69, 70]. Also pumps and valves constructed of FSM materials have been demonstrated, and potential future applications of FSM and other SM materials could include microgrippers, deformable mirrors, catheters in medical use, damping components, and velocity and acceleration sensors [38, 71]. The last of these applications are based on the reverse FSM effect where mechanical strains induce large voltages, up to 100 V [72].

The clear advantages of FSM alloys are their ability to generate very large strains and their high energy density at magnetic fields of ≈ 1 T. In addition, the maximum work output at weaker fields is of the same order of magnitude as that of standard giant magnetostrictive alloys (e.g., 0.01 J/cm^3 for Tb–Dy–Fe at 50 mT) [71]. One should, however, note that the work output for the best Ni–Ti alloys is almost 10 J/cm^3 . Furthermore, although the MFIS of, e.g., Ni–Mn–Ga is very high, up to 10 %, magnetostrictive materials are still competitive alternatives to FSM materials because of the large force they are able to produce; this force can be converted to large deflections with the help of bimetallic cantilevers [71]. But due to the good positioning accuracy (smaller than $1 \mu\text{m}$), the low power consumption, the narrow thermal hysteresis of Ni–Mn–Ga, and the possibility to replace complex mechanical systems with a piece of material, i.e., the material itself can act as a machine, FSM alloys are considered promising "smart" materials for several applications.

One interesting future application area are ferromagnetic semiconductors which make use of both the charge and the spin of electrons. Components made of such materials can be used in devices designed for quantum-information processing or quantum computing, and they enable the realization of, e.g., non-volatile memories that can be integrated into semiconductor devices and circuits [73, 74]. It has been suggested that ferromagnetic Heusler alloys are good candidates for efficient electrical spin injection into semiconductors [75].

2.6 Thin films of Ni–Mn–Ga

This section gives a brief introduction to the preparation of Ni–Mn–Ga thin films by different techniques and introduces the necessary requirements for the substrate material such that the film would crystallize in the desired phase. The topic will be covered in detail in the case of pulsed laser deposition in section 3.5.

Most of the research on Ni–Mn–Ga has so far dealt with bulk material whereas only a few groups have studied the preparation and physical properties of thin Ni–Mn–Ga films. However, thin films are an interesting research area since they would make it possible to realize micromechanical structures and even microscopic machines in a small volume. Other advantages of thin films are a low driving force [37] and large work output which scales linearly with the film thickness [76]. Thin FSM films are thus potential building blocks for robotics as well as for novel actuators and sensors.

Molecular beam epitaxy (MBE) has proven to be a successful technique to deposit high-quality Ni–Mn–Ga films on semiconductor substrates, in particular on GaAs [76–80]; gallium arsenide and other semiconductors are widely used substrate materials since small structures can be patterned into the films by using standard lithographic techniques. In some of the films deposited by MBE, the shape-memory effect during a repeated temperature cycling across the austenitic–martensitic boundary has taken place, and even signs of the FSM effect have been observed [76]. Other promising techniques to prepare FSM films include magnetron and ion-beam sputtering [81–85], flash evaporation [86], and pulsed laser deposition (PLD) [87–92]. The films studied in this work were deposited by the PLD technique.

The physical properties of the prepared films have generally been comparable to those of bulk samples. For example, the saturation magnetization has ranged from 20 to 40 emu/g, and by carefully optimizing the various deposition parameters, it can be increased up to 70 % of the typical bulk value. Such high values have been obtained for the samples studied in Papers I–III.

Takeuchi *et al.* [85] have prepared Ni–Mn–Ga films with different compositions by magnetron sputtering and mapped the phase diagram of Ni–Mn–Ga. The films were deposited on tiny silicon cantilevers fabricated in a single wafer. Their method provides a convenient way to find a proper Ni/Mn/Ga ratio for applications requiring a high T_M and/or a high T_C . Both sputtering and PLD are efficient techniques if one is interested in rapidly producing a large number of films with different compositions during a single deposition process.

In the context of this thesis, "thin" means that the film thickness is of the order of 50–500 nm. The physical properties of such films are generally rather homogeneous across the whole sample area and, furthermore, the overall film quality is sufficient

for patterning microscopic components on their surface. Note that the thicker the film, the more likely it is that stacking errors of atomic layers and the number of lattice defects or cracks and droplets on the surface start to accumulate. On the other hand, in the case of Ni-Mn-Ga, the film should be at least a few tens of nanometers thick such that unwanted phases formed, e.g., as a result of chemical reactions at the film-substrate interface are excluded from the Ni-Mn-Ga matrix. In addition, thicker films provide mechanical durability for many applications.

The substrate has to fulfill some general requirements such that Ni-Mn-Ga would crystallize in the desired phase:

- no or hardly any chemical reactions should take place between the film and the substrate,
- the substrate should preferably be smooth and single-crystalline to promote crystalline growth,
- the substrate should also have a proper lattice structure with a good match with the lattice constant of Ni-Mn-Ga in some crystallographic direction, and
- the thermal expansion coefficients of the substrate and the film should not deviate too much from each other.

The last condition is of great importance since the films are typically prepared at temperatures of approximately 500 °C but the operating temperatures rarely exceed 100 °C.

Standard semiconductors such as silicon, germanium, and GaAs meet relatively well the above-mentioned criteria and are thus proper substrate materials for the preparation of austenitic Ni-Mn-Ga films. However, at high temperatures silicon and GaAs tend to react with Ni-Mn-Ga, and, in particular, the mobility of Si atoms is enhanced such that they start to diffuse into the film matrix and form silicide compounds. For these reasons, chemically inert and structurally and thermodynamically compatible buffer layers with a thickness of only a few atomic monolayers have been used between the substrate and the film when depositing Ni-Mn-Ga on GaAs by the MBE technique. In addition, these interlayers act as templates in controlling the film growth and its orientation. Typical buffer-layer materials are Sc_{0.3}Er_{0.7}As [76, 77, 80], Ni-Ga [78], and ErAs [79].

Semiconductor substrates are not flexible, and to induce the martensitic transformation and to observe the FSM effect, the film has to be totally or partially released from its substrate (or an extremely thin substrate has to be used). In this work, this

last issue was addressed by depositing films also on other single-crystalline substrates such as on NaCl. Kim *et al.* [86] have already deposited Ni₂MnGa on glass and NaCl so that these substrates are known to be compatible with Ni–Mn–Ga.

Chapter 3

Pulsed laser deposition of Ni–Mn–Ga films

Pulsed laser deposition is a technique to prepare thin films of almost any material. In particular, it is suitable for multi-component ceramic compounds that are difficult to process into thin-film form by other methods such as thermal evaporation or co-deposition from multiple sources in MBE. In PLD, short and intense laser pulses (duration 100 fs–50 ns, pulse energy up to 1 J) interact with a target resulting in a massive ejection of particles, i.e., ablation from its surface provided that the pulse-energy density, fluence (J/cm^2), is sufficiently high. The emitted species form a high-pressure particle cloud which transforms to a plasma plume after having absorbed a significant amount of energy from the laser beam. The plume expands through the deposition chamber and, finally, the ablated particles condense on the surface of a substrate, which is typically placed opposite to the target. A schematic illustration of the PLD process is shown in Fig. 3.1.

The PLD process takes place in a vacuum chamber where the different deposition parameters — the fluence, the dimensions of the laser spot on the target, the temperature of the substrate, the distance between the target and the substrate, and the pressure of a possible background gas to mention the most important ones — can be adjusted in a controlled way; the optimal values of these parameters depend on the material to be ablated. The background gas can be reactive (such as O_2 in the case of oxide films), reducing (such as Ar/H_2 when depositing superconducting MgB_2 films), or passive (such as Ar). The Ni–Mn–Ga films studied in this work were generally deposited in vacuum; a couple of samples were prepared by using moderate Ar pressures (see Paper I).

In the following three sections, the three principal phases of a PLD process are reviewed: interaction of laser pulses with the target material, plume formation and expansion, and film condensation. The main emphasis is put on metals and metallic

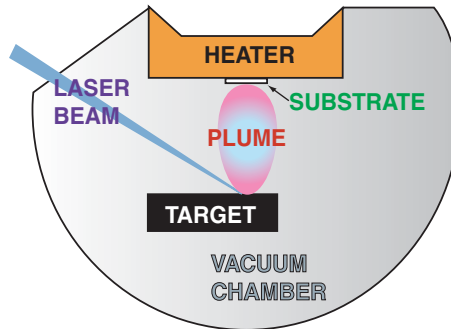


Figure 3.1: Principle of laser ablation. Energetic laser pulses hit the target and evaporate material from its surface. The emitted particles condense on the substrate surface.

alloys. Section 3.4 deals with laser-beam shaping, and in section 3.5, the deposition of Ni–Mn–Ga thin films is discussed and the experimental results are summarized. General references to these topics include [14–16, 93].

3.1 Interaction of laser pulses with matter

The interaction of laser pulses with matter can be divided into three different regimes by their timescales. In the femtosecond regime, the absorbed electromagnetic energy of a laser pulse is immediately converted to different excitations of the electron distribution such as plasmons, excitons, electron–hole pairs (in semiconductors), and unbound electrons (in metals). These *electronic processes* are considered the most important interaction mechanisms for the shortest, sub-picosecond laser pulses [94–98]. Due to the very short timescale, the ablation of particles in the femtosecond PLD can be considered a direct solid–vapor or solid–plasma transition. The power density can be high enough to cause even dielectric breakdown and multiphoton or avalanche electronic ionization in the material. Ultrafast laser pulses have generally a good ablation efficiency, and the threshold fluence can be many times lower than in the case of, e.g., nanosecond pulses. In addition, since the pulses are too short to couple the electronic energy to the crystal lattice, heat conduction is insignificant and ablation occurs practically without damaging the target [15, 93, 99].

In the case of picosecond and nanosecond laser pulses, the emission of particles is controlled by the conduction and diffusion of the absorbed energy in the lattice. Now the pulses are sufficiently long that the energy of the electronic excitations is transferred to the ions in the crystal lattice via electron–phonon coupling within a few picoseconds. As a result, either the lattice is heated or the interaction leads to

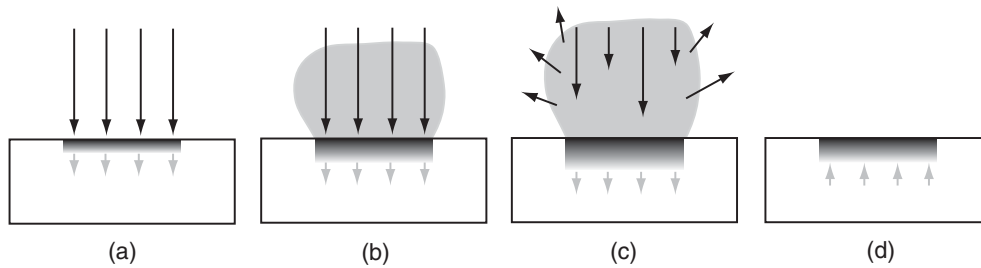


Figure 3.2: Schematic illustration of the ablation process in the case of nanosecond PLD. (a) Initial absorption of laser radiation (black arrows) and melting of the target material (grey arrows indicate the motion of the solid–liquid interface). (b) The melt front propagates into the solid and the evaporation of particles begins. (c) The plume absorbs the rest of the laser radiation and a fully ionized plasma is formed. (d) The melt front starts to recede after the laser pulse and the target is re-solidified.

the evolution of defects and gradual decomposition of the target surface [99–102]. If the absorption depth of the material, $1/\alpha$, where α is the absorption coefficient, is larger than the thermal diffusion length, the target surface will be heated to the thickness of $1/\alpha$ independent of the pulse duration. This is the case for many ceramics ablated with picosecond pulses, and it generally results in a significant removal of matter at low fluences. The situation is reversed for metals, for which it typically holds that the absorption depth is much smaller (≈ 10 nm) than the thermal diffusion length: all of the laser-pulse energy is deposited in a thin surface layer and then transported to a volume whose depth is of the order of one diffusion length. This depth is proportional to the square root of the laser-pulse duration. As a result, melting and vaporization take place inside the target and material starts to boil off into the vacuum [15, 16, 93, 99].

In nanosecond PLD, which is the case when using excimer or Q -switched Nd lasers, the situation presented above is complicated by the ionization of the evaporated particle layer. Again, the transfer of energy to the lattice occurs within the picosecond timescale but now there is enough time such that a large part of the target material heats up to temperatures above its melting and boiling points. In the case of metals, the long pulse duration creates a large layer of molten material, from which the evaporation of particles takes place. The target surface starts to vaporize after approximately 100 ps, and the material under the evaporated cloud is effectively screened from the rest of the laser pulse. Thus, the particle cloud absorbs a significant part of the incoming laser pulse. The process is schematically illustrated in Fig. 3.2 [15, 16, 93, 99].

The laser-pulse energy is finally converted to the kinetic energy of the emitted particles. The term ”sputtering” is used here to distinguish the different emission — or

ablation — mechanisms from each other. In *collisional sputtering*, the conservation laws for energy and momentum directly give the maximum transfer of energy from the projectile beam to the target. In the case of photons, however, only indirect collisional effects are of importance: the ions in a plasma plume can interact with the laser beam and, as a result, can be scattered towards the target [103]. In *thermal sputtering*, the particles are evaporated from a heated, partly molten target surface. As mentioned in the previous paragraph, this mechanism is the dominant one when depositing films of metal targets with nanosecond pulses. For short laser pulses, the primary mechanism responsible for the observed non-thermodynamical yield of particles is *electronic sputtering*. Different electronic processes were presented at the beginning of this section, and all of them have the common feature of inducing some form of ionizations or excitations. Electronic processes are also considered the main reason for the ejection of particles when ablating semiconductors or insulators with nanosecond pulses [102, 104]. Other ablation mechanisms are discussed, e.g., in Ref. [103].

The laser fluence has to be higher than a certain threshold value such that stoichiometric ablation takes place. The fluence can be increased either by increasing the pulse energy or by shrinking the dimensions of the laser spot on the target. However, too tight a focusing of the beam can result in a low removal rate of matter, the ejection of droplets or large particulates from the target, or the formation of cone-like structures in the surface, possibly enriched with respect to some element. Thus, the surface modification of the ablated targets as a function of the fluence and the pulse duration has attracted much research interest [99, 105].

The threshold value for the fluence has been determined for several different materials, and its dependence on the wavelength, the pulse duration, and the beam radius have been widely studied [93, 97, 102, 106, 107]. For noble and transition metals, the threshold value is of the order of $1 - 2 \text{ J/cm}^2$, for refractory metals such as Mo, Re, and W it is higher than 10 J/cm^2 , and for ceramics such as YBCO approximately 1 J/cm^2 . Generally, the larger the fluence, the fewer droplets or off-stoichiometric particulates are emitted but too high a fluence may lead to the sputtering of unwanted debris from the target. In addition, the shorter the pulse, the higher its spatial and temporal uniformity should be to ensure homogeneous ablation. This aspect will be discussed in section 3.4.

In PLD, lasers operating at UV wavelengths are commonly used since at short wavelengths the reflectivity of most materials, in particular that of metals, is much lower than in the IR regime. This promotes the absorption of the laser light and increases the ablation efficiency. Since also the absorption coefficient is large in the UV region, the beam energy is absorbed in a thin surface layer, which further intensifies the ablation process.

3.2 Plume formation and propagation

The material evaporated or otherwise ejected from the target is hot and partially ionized. In the nanosecond regime, this particle cloud absorbs further energy from the laser pulse that has initiated it, becomes more and more ionized, and finally a fully ionized plasma develops. The particles in the high-pressure plasma collide with each other until the bubble reaches thermal equilibrium at a distance of $\approx 50 \mu\text{m}$ from the target, in the so-called Knudsen layer [15, 16]. After this point, the particles can be described by the Maxwell–Boltzmann statistics, and the plasma *plume* starts to expand like a pulsed jet from a nozzle at supersonic velocities in the direction of the target normal. Typically, the spreading of the forward-peaked plume is modelled by a $\cos^n \theta$ law where n (not necessarily an integer) ranges from 1 to 10 depending on the material and the ablation parameters and θ is the scattering angle [108]. Also other, more complicated models for the formation and evolution of the plume have been presented [109–112].

The plume consists of ions, electrons, neutral atoms, particle clusters, and macroscopic particulates originating from the target or resulting from condensation and nucleation of particles in the supersaturated vapor. The emitted light and the color of the plume are caused by fluorescence and recombination processes in the plasma. Although atomic transitions typically have lifetimes of the order of a few nanoseconds, collisions can re-excite atoms such that the characteristic emission lines are observed even microseconds after the laser pulse [113].

As the plume expands, it rapidly evolves both in space and in time: the different species in the plume have different kinetic energies and their energy distributions will change as a result of interactions with other particles in the plasma. For example, the strong Coulomb force between electrons and ions prevents the electrons from escaping from the dense plume. Thus, they are decelerated with respect to neutral particles although they are light and have a high mobility [16]. The ions, on the contrary, are accelerated to higher velocities than the neutral species in the plasma. The electron temperature varies more slowly as a function of θ than the ion temperature, which, moreover, is peaked along the target normal. Typical values for the temperatures in an expanding plasma are 0.1 – 0.5 eV for electrons, 1 – 100 eV for ions, and a few eV for neutral particles [16, 108, 114, 115].

In an ambient gas, the plume behaves in a different way than in vacuum. In vacuum, the plume can be considered to expand adiabatically albeit, due to the high density of the plasma, the expansion is not completely unidirectional but backward velocity components appear as well. The molecules of the background gas, on the other hand, scatter, attenuate, and finally thermalize the plume. In addition, reactive scattering, e.g., with O_2 can produce clusters and molecules which are essential for the proper stoichiometry of the growing film. As the pressure of the background

gas increases, at first the fluorescence becomes more prominent. Then, the plume boundary sharpens and the plume itself becomes slower and better confined. At high pressures, a shock front is formed as the plume compresses the background gas. This results in an audible shock wave with a clicking sound (at atmospheric pressures) and, finally, the plume diffuses into the ambient gas [108, 113, 116].

The fluence has a significant effect on the shape, size, and visibility of the plume. As the fluence increases, the visible part of the plume becomes longer due to the increasing energy of the ablated species but the angular distribution is not considerably altered. At high fluences, the plume can tilt away from the target normal, probably due to the formation of cones, cracks, craters, or columnar structures on the target surface. A similar tilting effect is observed when the laser beam has a non-uniform intensity distribution or the laser spot size on the target is reduced too much. Decreasing the spot size but keeping the fluence constant results in an inefficient removal of matter and widening and shortening of the plume. In addition, the angular distribution of the plume in the substrate plane may change when the target-substrate distance is increased, in particular, when depositing the films in the presence of some background gas [108].

3.3 Film condensation

3.3.1 Different growth modes

The nucleation of a film is basically determined by the equilibrium between the vapor and solid phases of the material ejected from the target. Every compound has a tabulated, temperature-dependent equilibrium vapor pressure, and if the real vapor pressure of the arriving particle jet is larger than this equilibrium value, it is energetically favorable for the vapor to condense onto the substrate. The actual film growth can be further divided into four different modes depending on how the atoms arrange themselves on the substrate: three-dimensional growth of particle islands, two-dimensional formation of full monolayers, growth of islands on top of monolayers, and the so-called step-flow growth where the film follows the step-terrace structures of the substrate [117–119].

In the three-dimensional growth mode, the particles incident on the substrate surface form clusters which start to grow in size such that the resulting film finally consists of large but separate islands of atoms. The atomic processes connected to the nucleation and disintegration of clusters are presented in Fig. 3.3. Thermodynamically, all these processes change the total free energy of the film-substrate-vapor system. The cluster will grow if the derivative of the free energy with respect to the number of atoms in it is negative [117]. This condition is met beyond a certain critical radius

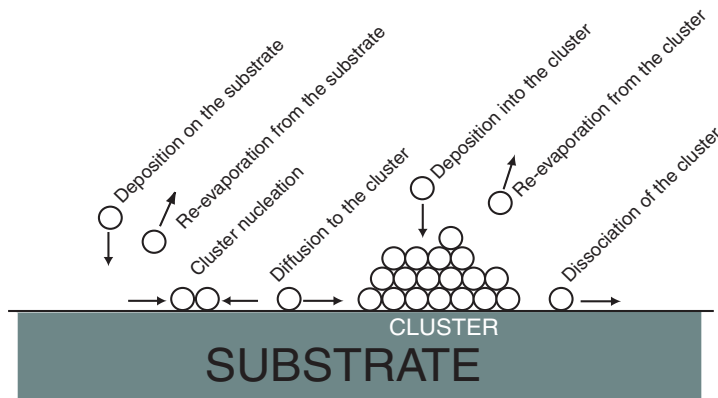


Figure 3.3: Different atomic processes in the nucleation of three-dimensional clusters on the substrate.

which is a function of temperature and supersaturation¹ of the incoming vapor. The formation of a stable cluster can also be described in terms of surface energies. If the sum of the surface energies in the cluster–vapor and substrate–cluster interfaces is larger than the corresponding surface energy for the substrate–vapor interface, the film will grow three-dimensionally since the area-to-volume ratio of a cluster is now smaller than that of planar structures [117]. The island growth can be promoted by decreasing the temperature and increasing the supersaturation, i.e., the deposition rate. On the other hand, if the supersaturation is very high during a single burst of particles followed by a longer period without a particle flux, the clusters will have time to evolve into full monolayers due to the high mobility of the atoms [120,121].

If the above-mentioned inequality for the surface energies is not satisfied, the film grows as full monolayers. This growth mode can also be considered to involve the formation of clusters but their radius is small and they are only one-monolayer thick. Two-dimensional growth takes place typically at high temperatures and at reasonably low supersaturations (deposition rates are not too high), and generally this layer-by-layer-type film growth results in epitaxial films with an atomically smooth surface. However, large periods between successive laser pulses can somewhat complicate the situation: the size of a critical cluster can grow and the sub-critical clusters may adhere into larger clusters promoting three-dimensional film growth [117, 122–125].

The third common growth mode is that after a few monolayers islands start to form and increase in size. This effect, mainly resulting from increased stress with increasing layer thickness, is due to a non-perfect lattice match between the film and the

¹Supersaturation means the ratio of the actual deposition rate and the thermodynamical equilibrium growth rate.

substrate. Island formation on top of monolayers has been observed, in particular, when depositing films of elemental metals [117].

The fourth way how the film can grow is the step-flow growth or, more generally, heterogeneous nucleation. For instance, atomic steps, point defects, and dislocations in the substrate provide additional nucleation sites for the incoming particles. Again, the onset of this growth mode depends on the various process parameters and on the film thickness: the temperature has to be high such that the island growth is suppressed and the deposition rate should be high such that the particles would not condense on a single monolayer but follow the seeds in the substrate. However, the thicker the film, the more probable it is that transition to the three-dimensional growth mode occurs [118, 119].

To obtain high-quality films in terms of their crystallinity and surface smoothness, the film should grow two-dimensionally, as full monolayers. A high substrate temperature, a reasonably large supersaturation of the particle plume and a properly lattice-matched and chemically inert substrate material are necessary pre-requirements for this type of film growth. In addition, the sticking coefficient of the film to the substrate should be large and the thermal expansion coefficients of the film and the substrate should not differ too much from each other. The background gas has a large effect on re-sputtering from the growing film but it can also prevent chemical reactions with, e.g., the residual oxygen in the deposition chamber. To meet many of the criteria mentioned above, Blank *et al.* [120, 121] have developed an interval deposition technique: one monolayer is quickly deposited using a high supersaturation followed by a break long enough such that the film has time to reorganize and grow in a layer-by-layer fashion. This guarantees a high nucleation probability during the short deposition interval but also decreases the size of three-dimensional islands and the probability for the particles to nucleate into them during the pauses.

3.3.2 Particulates on the film surface

The number of particulates on the surface is another issue that affects the overall film quality. The particulates can be categorized into small droplets (whose diameters range from a few nanometers to one micrometer) and large, possibly irregularly-shaped outgrowths (diameters up to tens of micrometers). The number density of the particulates depends on the fluence, the number of laser pulses on the target, and on the deposition parameters such as the substrate temperature and the background-gas pressure. The largest particulates are believed to originate directly from the target: breaking of protruding surface features, mechanical disintegration of, e.g., cones, craters, or microcracks, ejection of large droplets due to thermal

shocks, splashing of a molten surface layer, or violent expansion of gas bubbles under a solid layer are typical explanations for their emergence. Droplets, on the other hand, are either re-solidified objects ejected from the target or other species condensed from the supersaturated vapor on the substrate. By adjusting the deposition parameters properly, the particulate density can be minimized but, simultaneously, the number of so-called precipitates can increase. The precipitates are particulates with a stoichiometry totally different from that of the film matrix and they are a sign of good crystallinity: off-stoichiometric areas are excluded from the otherwise perfect film into a separate phase. The enrichment of the particulates or precipitates with respect to some element is typical for films deposited from metal-alloy targets since elements with a low melting point and a high vapor pressure are evaporated first thus making the target deficient in these components [126].

The particulate density is the highest off the deposition axis but the on-axis particulate density can also be high if the target–substrate distance is too small or the velocity of the species in the plume is too high. A high enough substrate temperature and a moderate background-gas pressure reduce the number of droplets and outgrowths on the film surface; reactive scattering at high pressures may lead to the nucleation and growth of additional particle clusters. The fluence has a complicated influence on the distribution and size of the particulates: the larger the fluence, the larger the particulates are but the smaller their number is on the deposition axis. Furthermore, the pulse repetition rate should be low enough such that the condensed species would have time to form a smooth layer with the correct stoichiometry but too low a rate should be avoided such that chemical reactions would not take place [126]. For example, repetition rates of the order of 1 – 10 Hz promote the growth of YBCO in the desired orthorhombic high-temperature phase [127] and result in a smooth film surface, whereas in the case of yttrium-iron-garnet films, the repetition rate should be above 20 – 30 Hz to prevent the loss of oxygen from the film matrix [128]. At the moment, there are only a limited number of studies on the effect of the laser-pulse duration on the film quality. Klini *et al.* have deposited ZnO films using nanosecond and femtosecond pulses at 248 nm and concluded that femtosecond PLD produces rougher surfaces with a higher number of small crystallites on the surface than nanosecond PLD [129].

3.4 Laser-beam shaping for the PLD process

In many application areas of laser ablation, uniform illumination, i.e., a so-called flat-top intensity profile, is required over a relatively large area compared to the dimensions of a focused spot. Examples include accurate lithographical patterning of small structures and components — especially in the UV region where the resolu-

tion is the highest — precise drilling and welding, laser surgery, and pulsed laser deposition [19, 20, 130–132]. In the case of PLD with Gaussian beams, only the central part of the beam leads to stoichiometric ablation whereas the beam edges may only heat the target or might not ablate all the elements stoichiometrically.

Many of the challenges presented in the previous sections have been addressed to make PLD an effective and reliable technique for the production of different materials in thin-film form:

- The particulates can be almost eliminated from the film surface by scanning the laser beam across the target or installing velocity filters in the plume path [126].
- Several techniques have been developed to remove non-uniformities of the thickness and composition profiles, in particular, of large-area films [133, 134].
- The problems related to the by-default Gaussian intensity distribution of the laser pulses can be solved by transforming the output beam into a flat-top-type distribution on the target surface [19, 20].
- The reproducibility of the PLD process can be improved by using a beam-homogenizing system to control the distribution of the energy density [19, 20].

The last two issues are of great importance since the profile of, e.g., a typical excimer-laser pulse is sensitive to alignment of the laser resonator, the discharge voltage of the laser, and the aging of the gas fill, and considerable fluctuations may occur from pulse to pulse [18–20].

The existing beam-shaping and -homogenizing approaches can be divided into three classes: beam aperturing, field mappers, and beam integrators (see Fig. 3.4) [130]. The first one is also the simplest: a suitable part of the possibly expanded laser beam is selected by an aperture, after which it is imaged onto the target. The uniformity of the resulting profile is rather good, and the steepness of the profile is determined by the sharpness of the aperture edges. However, the technique requires that the original beam profile has a homogeneous part that does not change from pulse to pulse or with the aging of the gas fill.

In the case of field mappers, the incident field is transformed to the desired distribution in the output plane by using a single refractive or diffractive phase element or a diffractive element together with a focusing lens. This approach makes it possible to realize flat-top and other non-Gaussian intensity distributions. Also so-called random phase plates belong to the class of field mappers [20]. It is worth noting

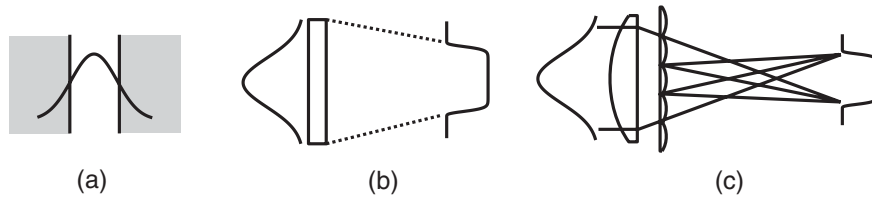


Figure 3.4: Three different ways to shape laser beams: (a) aperturing of a Gaussian beam, (b) transforming the Gaussian beam into a uniform distribution by a field-mapping element, (c) dividing the Gaussian beam into several beamlets and combining them in the focal plane of a positive lens.

that random phase plates and other field-mapping techniques were applied already in the 1980's to realize uniform illumination on laser-fusion targets [135, 136].

Beam integrators form the largest class of the suggested beam-shaping methods. Their operation principle is to divide the beam into beamlets and then combine them in a certain way in the focal plane of a lens. This typically requires incoherent or partially coherent light since, otherwise, the interference of the beamlets produces a rapidly fluctuating speckle pattern [137]. With the reported beam-integrator techniques, it has been possible to produce high-quality flat-top-like distributions and smoothen out a large part of the shot-to-shot intensity variations, e.g., of excimer-laser pulses [131]. Beam integrators can be arrays consisting of refractive or diffractive elements such as microlenses or a single diffractive element [21, 131]. Wagner *et al.* [19] have improved the basic technique by aperturing and imaging the resulting flat-top profile onto the target surface: the homogenized beams had a good quality, which was manifested by uniform erosion of the target and the homogeneous growth rate of the film. Diffractive beam shaping has been studied by Turunen *et al.* [21, 24] and this technique will be discussed in more detail in chapter 5.

In addition to these "standard" techniques, flat-top profiles can be produced by using a system consisting of prisms, mirrors, lenses, and beam splitters [138]. The beam-shaping problem has also been addressed in Refs. [139–142], and in addition to improvements on the above-mentioned ideas, an interesting concept of producing beams directly from laser resonators was presented. Matsuura *et al.* [143] presented another novel idea: excimer-laser beams were guided with hollow quartz fibers into rectangular hollow waveguides, which homogenized the approximately Gaussian profile coming out from the fiber. Bollanti's [144] idea was to improve the beam-integrator approach by adding a zoom and an asymmetric array divider into the system such that smaller microlenses could be used in the region where the beam profile is the most asymmetric.

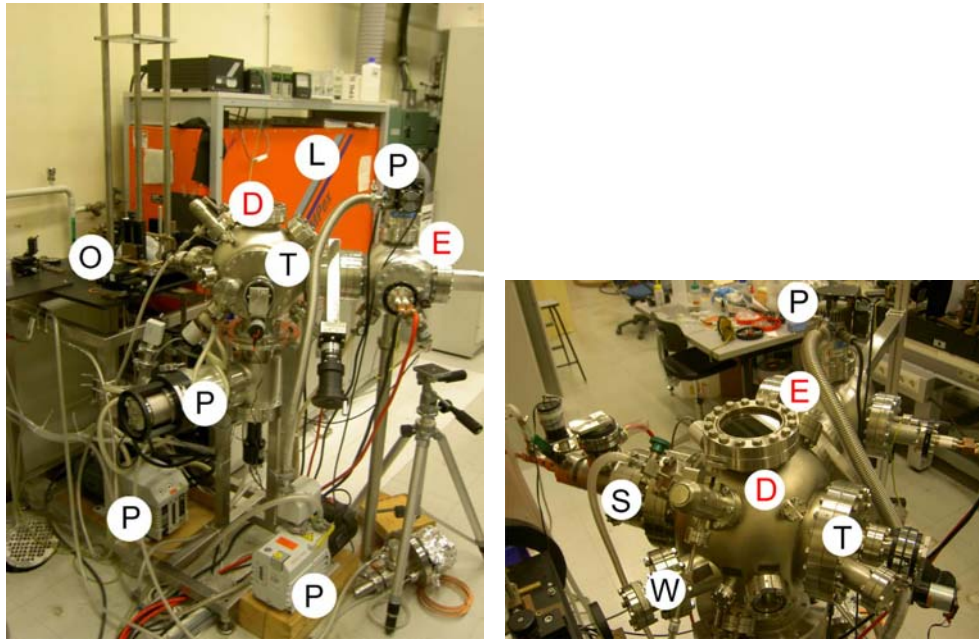


Figure 3.5: Photographs of the PLD system at Helsinki University of Technology. D: deposition chamber, E: load chamber, L: excimer laser, O: beam-guiding and -shaping optics, T: target holder, S: substrate heater, P: vacuum pumps, W: beam-entrance window.

3.5 Experimental

3.5.1 Equipment

The Ni–Mn–Ga films were prepared using the PLD system in the laser laboratory of Helsinki University of Technology. A detailed description of the setup is presented in Refs. [17, 145]. In the following, only a brief overview is given. A photograph of the system is shown in Fig. 3.5.

The laser pulses are produced by a Lambda Physik COMPex 205 KrF excimer laser. The wavelength is 248 nm and the pulse duration is approximately 20–30 ns. The maximum pulse energy obtained with a discharge voltage of 26 kV is 500–600 mJ. The dimensions of the nearly rectangular transverse output profile of the beam (FWHM, $x \times y$) are $10 \times 26 \text{ mm}^2$. The profile is approximately Gaussian albeit in the longer y direction it is not perfectly symmetric. In the present beam-shaping and -guiding system, the pulses pass through a $6 \times 12\text{-mm}^2$ aperture, after which they are imaged with a $f = 340\text{-mm}$ lens onto the target surface. The intensity distribution on the target is flat-top-like with steep edges and a rather good uniformity across the typical $3 - 4\text{-mm}^2$ spot area [146]. However, less than 20 %

of the original laser-pulse energy ends up in the target plane due to the large number of optical components — the aperture, four mirrors, the focusing lens, and two windows — in the setup and the long optical path (> 3 meters) between the aperture and the target. This is one of the reasons why we have studied other ways to realize the desired intensity profile in the output plane, e.g., by applying diffractive beam shaping. Typically, the pulse energy on the PLD target is 80–100 mJ and the corresponding fluence is 2–3 J/cm².

The depositions take place in a 12-inch-diameter vacuum chamber whose base pressure can be lowered down to 10^{-9} mbar. Special attention has been paid to the choice of materials for the different vacuum parts since originally the chamber was designed for the deposition of high-temperature superconducting YBCO films which require high temperatures (800 – 900 °C) and oxygen pressures (0.1 – 1000 mbar). The substrates are inserted to the deposition chamber from the load chamber (see Fig. 3.5) with a transfer rod. The chambers can be evacuated separately with their own turbo molecular pumps, which makes it possible to remove the film from the deposition chamber immediately after its preparation without breaking the vacuum. In the load chamber, it is also possible to thermally evaporate a protective or contact metal layer, e.g., a gold film onto the sample.

The target holder keeps the ablation targets fixed in the vertical orientation during the deposition process. In the Ni–Mn–Ga experiments, a simple one-target holder was used. The maximum diameter and thickness of the target disk in this configuration are 50 and 6 mm, respectively. It is also possible to deposit multilayer films, e.g., Ni–Mn–Ga with buffer layers by using a carousel-type holder designed for three targets, whose maximum diameter is 50 mm and thickness 3 mm [17]. In both cases, the targets are rotated during the deposition to ensure uniform wear of their surfaces.

The substrate heater consists of eight 400-W halogen lamps mounted on a water-cooled reflector. The reflector is surrounded by a rotating cylinder, on top of which the substrate and its supporting plate are attached. The substrate can be radiatively heated up to 900 °C by a HP 6684A DC power supply, but in these experiments typical substrate temperatures were much lower, 450 – 600 °C, which corresponded to DC currents of 45 – 55 A. The temperature was monitored by an S-type thermocouple, the end loop of which was wired between the lamps. The substrate temperature was somewhat lower than the reference value obtained by this method, and a pre-determined calibration curve was used to estimate the real sample temperature [134]. To ensure a proper thermal contact during the depositions, the substrate was attached to its supporting plate with silver paint.

3.5.2 Deposition process

Before the deposition, typically in the previous day, the substrates and the supporting plate were cleaned, the substrates were mounted on the plate, and the silver paint was left drying overnight. As substrates we used small ($0.5 - 1 \text{ cm}^2$) pieces cut from larger wafers, whose upper side was polished to enable epitaxial film growth. The studied substrate materials were semiconductors Si, GaAs, and Ge and NaCl as well as bulk Ni-Mn-Ga.

The number of films possible to prepare during a single deposition was restricted to 4 – 8 due to the small homogeneous central part (diameter $\sim 20 \text{ mm}$) of the plume in the target plane. The deposited area and, simultaneously, the production rate of the films could be increased by increasing the distance between the target and the substrate but, on the other hand, the larger the distance, the lower the growth rate is and the larger is the probability that detrimental reactions take place in the substrate plane. In most of the experiments, the target-substrate distance was fixed to approximately 50 mm; this value was slightly varied within the practical limits of the present deposition system, i.e., from 45 to 60 mm but no noticeable differences in the measured properties of the films were observed.

The targets were 30-mm-diameter and 3-mm-thick slices cut from Ni-Mn-Ga ingots. The ingots were provided by AdaptaMat Ltd. and the Laboratory of Physical Metallurgy and Materials Science of Helsinki University of Technology. The targets were mounted to the rotating holder with the help of a stainless-steel adapter. When depositing Fe-doped Ni-Mn-Ga films, the standard target geometry was slightly modified as illustrated in Fig. 3.6. In one of the approaches, the Ni-Mn-Ga disk was surrounded by an iron ring, and by moving the imaging lens, the laser spot was continuously transferred from Ni-Mn-Ga to iron and back; for example, first ablating the disk for 30 s and then the iron ring for 2 s and repeating this procedure some 100 times. Since the inner edge of the Fe ring had a small inclination angle with respect to the Ni-Mn-Ga target, the iron plume did not point directly towards the target. However, this deviation was so small that it was overrun by the much larger tilting effect of the plume towards the laser beam. In the second iron-doping approach, a small notch was cut in the target and an iron wedge was tightly pressed into it. The iron content of the film could now be selected between 0 and 4 % since, according to Fig. 3.6, the amount of iron ablated during the deposition depends on the radial position of the laser spot on the rotating target. The third way to prepare films with the desired iron content is to use a target with a fixed Ni/Mn/Ga/Fe composition. The advantage of this method is that iron will be evenly distributed in the film matrix — and its concentration is uniform also in the target — but separate targets are needed for each doping level.

In the experiments, the laser fluence ranged from 2.5 to 3 J/cm², the substrate

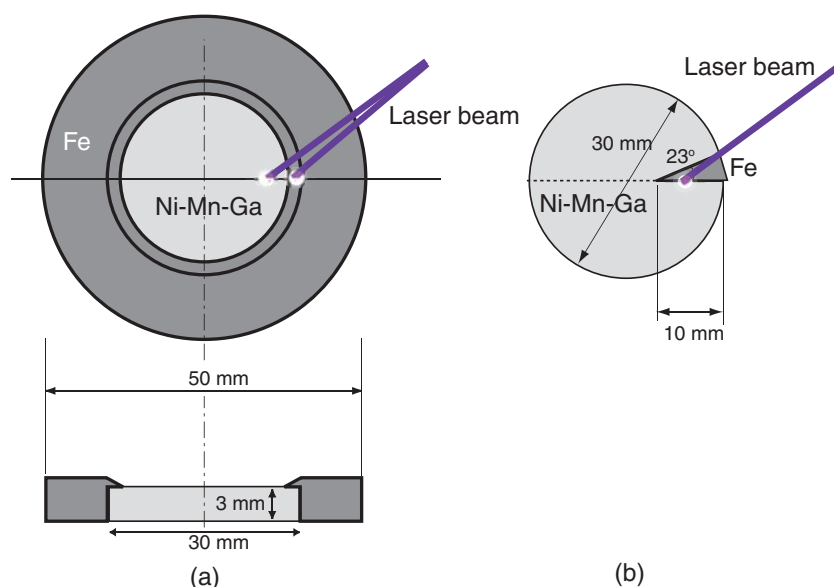


Figure 3.6: Two different approaches for the deposition of iron-doped Ni–Mn–Ga films. (a) Ni–Mn–Ga disk surrounded by an iron ring. The laser beam is continuously transferred from Ni–Mn–Ga to iron and back. (b) Iron wedge tightly pressed in a notch in the target. The iron content can be continuously varied between 0 and 4 %.

temperatures were varied between 450 and 600 °C, the laser-pulse repetition rate was 10 – 15 Hz, and the depositions took place in vacuum (base pressure 10^{-7} – 10^{-5} mbar). With these parameters and with 40,000 pulses the film thickness was typically 200 – 300 nm. The growth rate depended, however, strongly on how many depositions had been made after the target had been polished and the beam-entrance window cleaned: after just two depositions, the target surface was so eroded that the plume was significantly tilted away from the target normal and the window was coated with the ablated debris so that the real fluence on the target surface could be less than half of the estimated value. To get rid of these problems, the target surface was regularly polished and the chamber window was either cleaned or polished after two or three depositions.

When preparing Ni–Mn–Ga films on single-crystalline Ni–Mn–Ga substrates, a slightly different deposition recipe was applied. The substrate temperature was kept below the Curie temperature (≈ 100 °C) but above the martensitic transformation temperature of the substrate alloy (≈ 40 °C). Unfortunately, our deposition system is not optimized for such "low" temperatures and, therefore, the experiments had to be made by continuously switching the heater lamps on and off.

A couple of the deposited samples were annealed at high temperatures after their magnetic properties were measured. The samples were sealed in evacuated quartz

ampoules, which were then put in a furnace. The furnace was kept at a constant temperature of 800 – 1000 °C. In some of the ampoules, we also put a piece of Mn or Ni–Mn–Ga to compensate for the possible evaporation of Mn during the heat treatment. The annealing times ranged from 15 to 30 mins.

3.5.3 Film characterization

The magnetization curves of the deposited films were measured with a self-built vibrating sample magnetometer (VSM). The studied sample was attached on top of a quartz rod which vibrated at a small amplitude and at 20-Hz frequency in a homogeneous magnetic field. The flux density of the field was varied between –1.5 and 1.5 T. The vibrating sample induces a voltage to four pick-up coils symmetrically installed on both sides of the sample. The signal was detected by a lock-in amplifier (Stanford Research Systems, SR830DSP). The conversion factor between the induced voltage and the magnetization was determined from earlier measurements made with a Ni disk with a known saturation magnetization; the voltage is directly proportional to the magnetization. The signal from the 200 – 300-nm-thick films is weak (of the order of 100 – 500 nV) but discernible although external noise and small changes in the measurement conditions have a significant contribution to the results. Thus, each point in the magnetization curve is an average over 500 or 1000 successive measurement results for the signal voltage at a certain magnetic field. In addition, the VSM system was calibrated by determining the response of a bare substrate and the sample holder, and this reference data was subtracted from the obtained $M(H)$ curve.

To measure magnetizations at different temperatures, a furnace-type heater has been designed such that the sample vibrates inside two concentric tubes. The inner one, made of copper, is the actual heating element, whereas the outer stainless-steel tube acts as a thermal shield but also as a flow cryostat when decreasing the sample temperature, e.g., with the flow of cold nitrogen gas [147].

The surface morphology of the films was studied with a LEO-1450 scanning electron microscope (SEM), and their chemical composition was simultaneously determined by using energy dispersive spectroscopy (EDS). The crystal structure was analyzed by a Phillips X'pert X-ray diffractometer with Co K_α radiation. The samples were also visually inspected by optical microscopes.

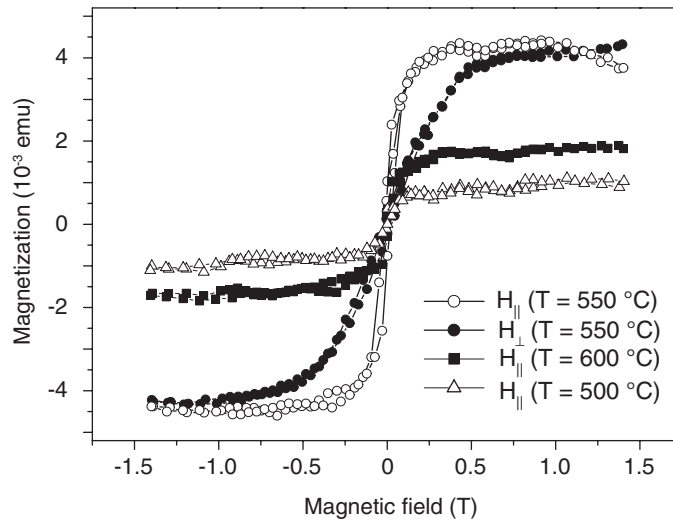


Figure 3.7: Magnetization curves of Ni–Mn–Ga films deposited at 500 °C (open triangles), 550 °C (open and solid circles), and 600 °C (solid squares). The curves labelled with H_{\parallel} are measured by applying the magnetic field parallel to the film plane, whereas the curve with a sign H_{\perp} has been obtained by applying the field perpendicular to this plane.

3.5.4 Results

Magnetic properties

The magnetization curves of Ni–Mn–Ga films deposited at different temperatures on silicon are shown in Fig. 3.7. The magnetizations have been measured by applying the external field parallel to the film plane and, in the case of the sample with the highest magnetization, also in the direction perpendicular to this plane. The in-plane curves saturate quickly and show a narrow hysteresis indicating that the films dominantly consist of a single magnetically soft phase. Most probably this is the austenitic phase. In the perpendicular direction, the curve is tilted only due to the effect of the demagnetizing field (see Eq. (2.1)). These observations show that the phase that has been formed has a low anisotropy.

By using the estimated values for the film thickness (200 – 300 nm) and its surface area (0.5 – 1 cm²) and assuming that the density is close to that of bulk Ni–Mn–Ga (8 g/cm³), specific saturation magnetizations of the order of 20 – 40 emu/g were obtained; the largest determined values are 60 – 70 % of the typical bulk value (60 emu/g) and comparable to the reported values for Ni–Mn–Ga films prepared by other groups [77, 78]. A more detailed analysis of these results can be found in Papers I and II.

The results show that PLD is a suitable technique to deposit ferromagnetic

Ni-Mn-Ga films once the deposition parameters have been properly adjusted. The most important observation was that the substrate temperature should be 500 – 550 °C: at lower temperatures Ni-Mn-Ga does not crystallize in the austenitic phase and at higher temperatures chemical reactions such as the diffusion of Si atoms into the Ni-Mn-Ga start to degrade the film quality finally leading to the formation of a non-ferromagnetic phase.

In the case of single-crystalline Ni-Mn-Ga substrates (see Paper II), the deposition temperature was kept below 100 °C as explained in subsection 3.5.2. These combined film-substrate structures of Ni-Mn-Ga exhibited the same 6-% strain as the bulk after the deposition but their magnetic properties could not be determined: it was not possible to distinguish the contribution of the sole film from the total magnetization of the whole sample. It was also difficult to determine how thick the film actually was since it had fused with the substrate into a single structure. The film layer could nevertheless be observed by taking transmission-electron-microscope (TEM) images of a thinned sample but at the time of these experiments, we did not have access to a TEM.

Only with one sample one could be sure that a new layer had been formed onto the bulk surface: after the sample was taken out from the deposition chamber and then bent, it cracked. The most probable reason for this cracking is stress between the film and the substrate. The substrate temperature might not have been high or stable enough during the deposition such that the film could not crystallize in the correct phase or that the target and the substrate alloys might have had too different transformation temperatures such that the atoms in the film matrix could not follow the template provided by the Ni-Mn-Ga substrate. Nevertheless, the results we obtained were promising and gave evidence on the importance of optimal deposition conditions but also of the substrate material on the preparation of martensitic Ni-Mn-Ga films.

The substrate has a significant effect also on the magnetization of the deposited films. Although all the selected materials had a relatively good lattice match² with Ni-Mn-Ga, only films on Si and NaCl were measured to be ferromagnetic; films on GaAs and Ge were paramagnetic independent of the deposition conditions. As discussed in Paper II in the case of GaAs, the most probable explanation for the lack of ferromagnetism is that the film and the substrate react chemically at their interface. It may be possible to eliminate this problem by depositing a properly lattice-matched and chemically inert buffer layer between the materials (see, e.g., Refs. [77, 78]) but these "extra" layers complicate the fabrication of micromechanical structures. Therefore, we decided that the preparation of multi-layer films does

²The lattice constants are: Silicon, $a = 0.543$ nm, diamond structure; Germanium, $a = 0.566$ nm, diamond structure; GaAs: $a = 0.565$ nm, zincblende structure; NaCl: $a = 0.565$ nm, fcc lattice

not belong to the main research questions of this thesis.

In Papers I and II, the role of other deposition parameters than the substrate temperature on the ferromagnetism of the samples has also been briefly discussed. Some of the films on silicon and on GaAs were prepared at different background argon pressures ranging from 3×10^{-4} to 5×10^{-3} mbar. Argon was selected as the background gas to prevent reactions with residual oxygen and to shape the kinetic-energy distribution of the plasma plume. However, the highest magnetizations were obtained for films prepared in vacuum and the higher the argon pressure, the smaller was the saturation magnetization until finally the films turned out to be paramagnetic. This is most probably due to the fact that argon promotes reactive scattering in the plume and change either the stoichiometry or the crystal structure of the growing film. Thus, the preparation of strongly ferromagnetic films requires at least a high vacuum ($p < 10^{-5}$ mbar).

Only films deposited at fluences above or of the order of 3 J/cm^2 were ferromagnetic. This implies that the threshold fluence for stoichiometric transfer of the target alloy to the substrate is somewhat higher than that for the elemental Ni, Mn, and Ga. One should, however, keep in mind that the actual fluence on the target was sensitive to the dirtiness of the beam-entrance window. To make sure that the threshold value would be exceeded in all circumstances, the window was cleaned after two or three depositions and the laser gases were changed as soon as the laser-pulse energy in front of the imaging lens dropped below 100 mJ.

In addition to the deposition parameters, the post-annealing conditions have to be optimized carefully. Ohtsuka *et al.* [83, 84] have demonstrated the importance of heat treatment at $800 - 1000 \text{ }^\circ\text{C}$ on the crystallinity, and, consequently, on the magnetic properties of the as-deposited films. So far, our experiments presented in Paper I have not been successful — annealing resulted in the disappearance of ferromagnetism — although the annealing time was kept short and the possible loss of Mn was compensated by pieces of Mn or Ni–Mn–Ga. Since the annealed samples were prepared on silicon, we conclude that the tendency of silicon atoms to react with Ni–Mn–Ga at high temperatures and to form silicide compounds is so large that the heat treatment should be made only after the film has been released from its substrate — as reported in Refs. [83, 84].

In Paper III, the studied films were deposited on NaCl. The magnetization curves at different temperatures for one of these samples are shown in Fig. 3.8. The saturation magnetization remains at the determined high level, approximately 40 emu/g, also after the substrate has been removed. In addition, the continuous decrease of magnetization of another, partially released sample as a function of temperature indicates a gradual phase transformation to the martensitic phase (see Fig. 3.9). In the case of silicon, no signs of such a transformation were observed although the samples were cooled down to 10 K as stated in Paper I. This suggests that the elastic

constraint set by the substrate restricts free movements of the film and prevents the martensitic transformation from taking place.

However, the magnetization loops in Fig. 3.8 and also those determined for the sample in Fig. 3.9 did not show any noticeable differences from the room-temperature behavior: the saturation magnetization increases slightly and the hysteresis loop becomes wider but the transformation to the martensitic phase would have changed the curves more or less to resemble those in Fig. 2.14. It might well be that the samples have transformed only partly to the martensitic phase, which explains why the decreasing tendency of $M(T)$ is difficult to observe from the measured $M(H)$ curves: the austenitic response is still the dominant one. Another possibility is that the martensitic state is not fully stable. This hypothesis is supported by sudden jumps in the magnetization at around -80 °C (see Fig. 3.9). But one should keep in mind that we did not know exactly how the components of the measurement system or the substrate behaved at low temperatures. Nevertheless, these results support the claim that shape-memory effects are possible when the effect of the substrate has been eliminated.

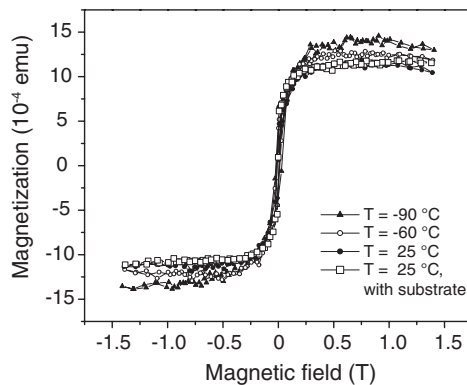


Figure 3.8: Magnetization curves at $+25$ °C, -60 °C, and -90 °C for a Ni–Mn–Ga film deposited on NaCl. The room-temperature curve has been measured both with and without the NaCl substrate.

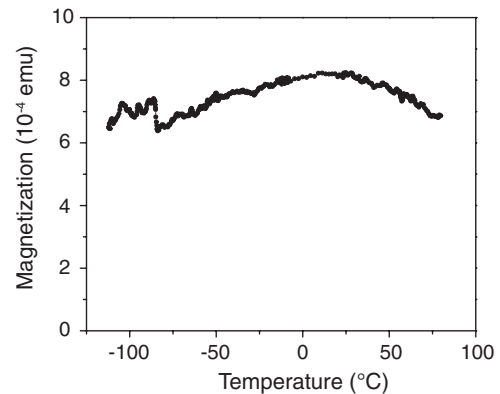


Figure 3.9: Magnetization of a partially released Ni–Mn–Ga film as a function of temperature from -110 °C to $+80$ °C. The flux density had a constant value of 0.5 T.

The results presented in Papers I-III form the basis for studying the effect of iron doping on, e.g., the magnetic properties of Ni–Mn–Ga films. Figure 3.10 presents in-plane magnetization curves of Ni–Mn–Ga films with different iron content. These samples were prepared by using the combi-target consisting of a Ni–Mn–Ga disk and a surrounding iron ring (see Fig. 3.6). One notices that the saturation magnetization slightly increases and the hysteresis loop somewhat widens as the iron concentration increases but the changes are yet marginal when comparing the curves with

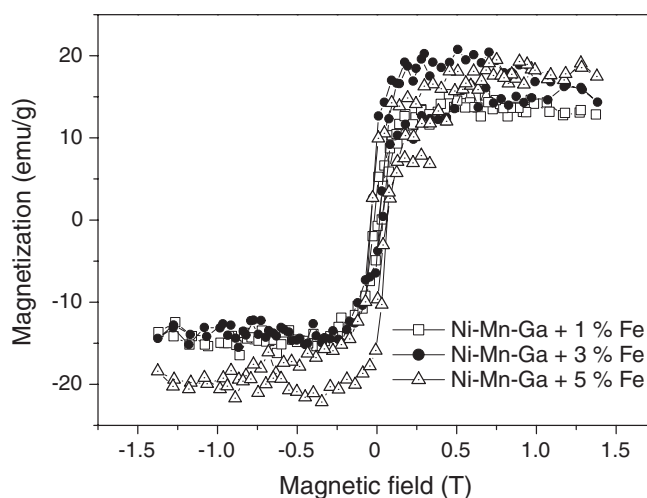


Figure 3.10: Magnetization curves of Ni–Mn–Ga films with different iron content: 1 % (open squares), 3 % (solid circles), and 5 % (open triangles).

those measured for undoped samples. As a conclusion, although the dopants are known to change the thermodynamical transition temperatures, these results show that the doping level should be well above 5 % until iron has any noticeable effect on the magnetization of Ni–Mn–Ga films.

Crystal structure

Typical X-ray diffractograms for films deposited on Si, GaAs, and NaCl are shown in Figs. 3.11 and 3.12. Some of the curves have been published in Papers I–III. In the case of NaCl, the measurements were made after the sample was released from its substrate since the as-deposited film had too uneven a surface to obtain any reasonable X-ray data. In Fig. 3.11, the highest peaks are due to the substrate whereas in Fig. 3.12 the peaks labelled with NaCl are caused by tiny residual crystals of NaCl on top of the film.

In the case of films on silicon, the peaks labelled with "austenite" (Fig. 3.11a) match with a cubic structure, whose lattice constant is 0.580 nm — close to the value determined for bulk Ni–Mn–Ga in the parent austenitic state [47, 48]. Iron doping did not have any effect on the crystalline structure of the films. The additional peaks in the diffractograms suggest the presence of another cubic phase with a lattice constant of 0.539 nm, i.e., very close to that of silicon. This phase is assumed to be an intermediate layer between the austenite and silicon.

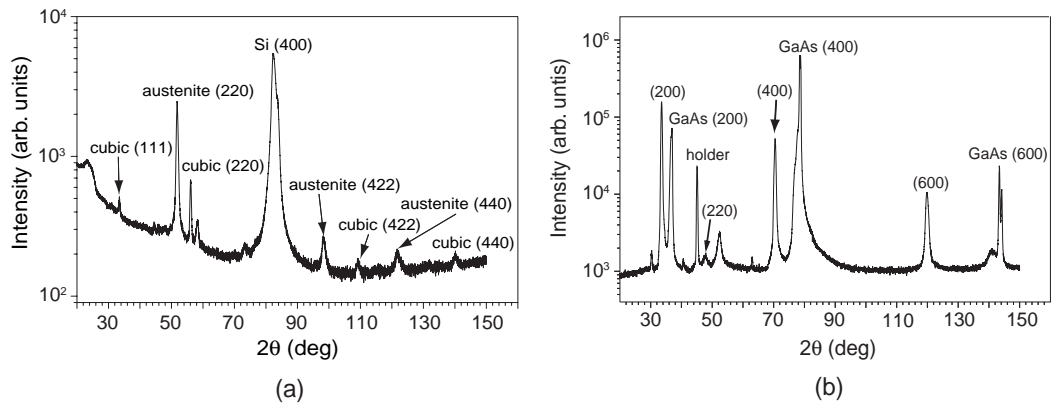


Figure 3.11: X-ray diffractograms of Ni–Mn–Ga films deposited on (a) silicon and (b) GaAs.

No traces of the austenite were observed in films deposited on Ge or on GaAs. According to Fig. 3.11b, the films on GaAs had crystallized in a cubic phase with a strange lattice constant of 0.62 nm but a very strong texture in the (1 0 0) direction perpendicular to the sample surface. These results indicate that despite a relatively good lattice match, GaAs (and Ge) are not chemically compatible with Ni–Mn–Ga. No data was obtained for Ni–Mn–Ga on Ni–Mn–Ga crystals since the contribution of the film could not be distinguished from that of the substrate and, besides, the granularity of the crystal surface made the X-ray measurements rather difficult a task.

NaCl seems to be best substrate material when considering the crystallinity of the films: the austenitic phase can again be identified from the diffractograms (see Fig. 3.12) and a pole figure of one of the analyzed samples in Fig. 3.13 shows a strong texture in the (1 0 0) direction perpendicular to the surface after the sample was tilted by 45°. This gives evidence that the film is polycrystalline, not amorphous with occasional austenitic crystals distributed in the film matrix.

All the results show that by using proper substrate materials, the films will crystallize in the desired high-temperature austenitic phase with the correct lattice constant and a good crystallinity. Buffer layers might help in matching the lattice constants of the substrate and the film with each other and in eliminating the unwanted phases from the film–substrate interface.

Surface quality

Typical SEM images of the surface of the deposited Ni–Mn–Ga films on Si, GaAs, and NaCl are shown in Figs. 3.14, 3.15, and 3.16, respectively. The films on silicon

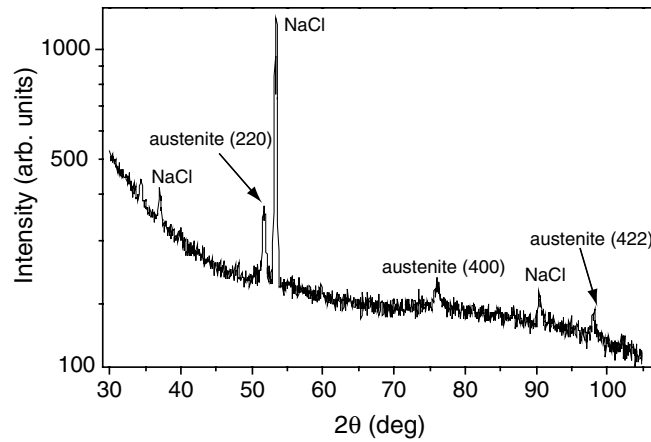


Figure 3.12: X-ray diffractogram of a Ni–Mn–Ga film deposited on NaCl. The data were taken after the film had been released from the substrate.

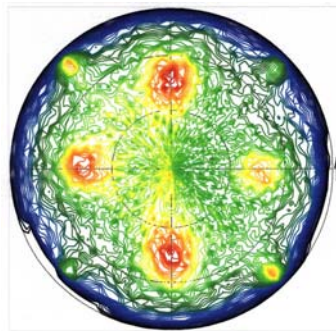


Figure 3.13: Pole figure of the same Ni–Mn–Ga film as in Fig. 3.12 indicating a strong texture in the (1 0 0) direction perpendicular to the film surface.

generally have a smooth, mirror-like surface in the macroscopic level with only a few μm -sized droplets. The droplet density, as calculated in Paper I, is relatively low, only $\approx 0.01 \mu\text{m}^{-2}$. Such values were determined for all the studied samples prepared by using substrate temperatures within the optimal window of 500–550 °C and fluences of the order of 3 J/cm². These results confirm that the parameters used in the deposition experiments were properly selected: only minor optimization is needed to further improve the magnetic properties of the films and promote the film growth in the austenitic phase.

Again, the results obtained from films on GaAs emphasized the importance of chemical compatibility of the film and the substrate materials: the granular surface one can observe in Fig. 3.15 is most probably caused by Ni–Mn–Ga reacting

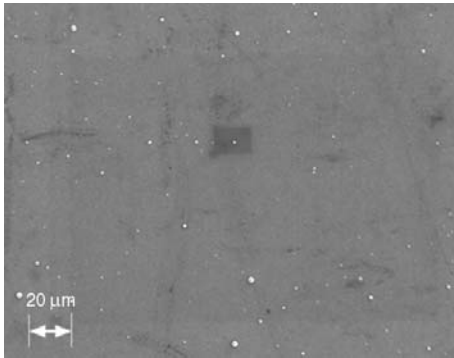


Figure 3.14: Scanning electron microscope image of the surface of a Ni-Mn-Ga film deposited on silicon.

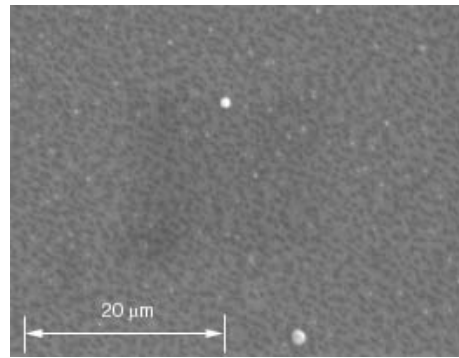


Figure 3.15: Scanning electron microscope image of the surface of a Ni-Mn-Ga film deposited on GaAs.

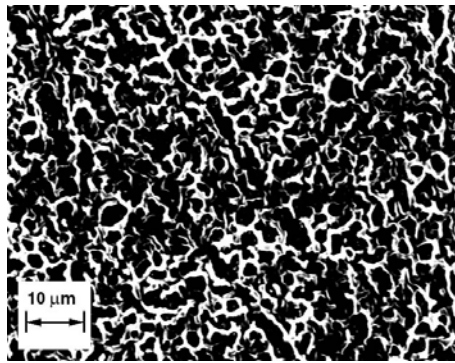


Figure 3.16: Scanning electron microscope image of the surface of a Ni-Mn-Ga film deposited on NaCl.

with As atoms of the GaAs substrate, and this is the most probable reason why none of these films was ferromagnetic.

The films on NaCl showed an uneven surface which visually resembled wrinkled aluminum foil. In fact, some of the samples had a mirror-like surface when they were taken out of the ablation chamber but when they were accidentally subjected to small mechanical shocks (such as dropping them upside down on a laboratory table), the same corrugated-iron-like surface emerged. This is most probably due to the large mismatch in thermal expansion coefficients of NaCl and Ni-Mn-Ga: as the deposited film cools down to room temperature, the substrate shrinks more than the film resulting in compressive stress and popping up of the film from the NaCl surface.

The compositions of some of the films deposited on Si were determined by the EDS

technique. Examples are presented in Papers I and II, and the obtained Ni/Mn/Ga ratio was close to that of the target; the small deviations from the target composition can be explained by the strong signal originating from the substrate, which made it difficult to determine the exact proportions of Ni, Mn, and Ga in the studied film. The EDS method was also applied to determine the real iron content of Fe-doped samples, and these results were then compared with the goal values. For example, the measured Ni/Mn/Ga/Fe compositions of films prepared by scanning the laser beam between the Fe and Ni–Mn–Ga targets according to a pre-determined program were approximately 56/37/5/2, 50/35/9/5, and 53/35/5/6 for samples with the goal Fe concentrations of 1 %, 3 %, and 5 %, respectively. However, these values were taken from visually smooth locations of the film; droplets on the surface contained hardly any iron but were Ga-enriched and Mn-depleted. It seems reasonable to assume that gallium tends to be excluded from the film matrix, and this might be one of the reasons why no clear transitions to the martensitic state have been observed: the film stoichiometry is not correct in the microscopic level. This issue will be at the focus of further studies.

Realization of free-standing structures

As discussed in Paper III, NaCl is a good substrate material to realize free-standing structures and totally released films due to its high solubility to water. In the previous subsections it became evident that such structures enable one to study magnetic and structural properties of the films without the restricting effects of the substrate. Furthermore, the air bridges we have fabricated are the first steps towards the fabrication of FSM components and microscopic machines.

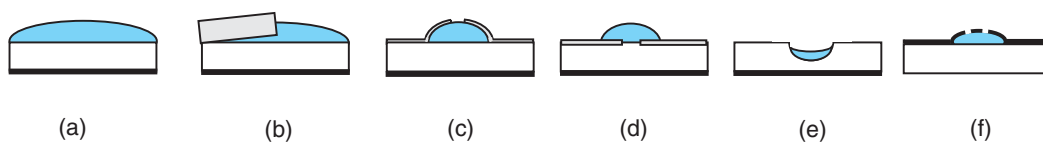


Figure 3.17: Different approaches for the realization of free-standing films and film structures. White boxes represent the substrate, black lines the film, and grey areas the masks. Blue regions stand for water. (a) Removing the whole substrate with water. (b), (c), and (d) Isotropic etching with water using masks made of plastic, Scotch tape, and silver paint, respectively. (e) Deepening of the grooves realized in (d) with small drops of water. (f) Isotropic etching through template grooves created by diffractively-shaped excimer-laser pulses.

Four different approaches to realize the free-standing films and small structures were tested in this thesis (see Fig. 3.17). In the simplest of them (Fig. 3.17a), the

film was placed upside down on a piece of flexible plastic and NaCl was dissolved away with a few drops of water; the film was then left on the plastic to wait for further analyses. The most straightforward technique to fabricate partially released structures was to put a plastic mask on the back face of the substrate and drop water on the uncovered regions of the substrate with an injection needle (Fig. 3.17b). However, even the tiniest droplets tended to wet large areas of the substrate and penetrate under the mask such that only mm²-sized structures — holes at the center or cantilevers close to the substrate edges — could be realized. A slight improvement was to replace the plastic mask with Scotch tape or silver paint at the back face of the substrate (Figs. 3.17c and d). A surgical knife was used to make thin cuts into the tape or the paint, and shallow grooves were created in the exposed areas of the NaCl substrate with water. After that, the protective layer was removed and the dissolution procedure was continued by dropping water into the grooves (Fig. 3.17e). Unfortunately, the feature size could not be significantly reduced below 1 mm, which seems to be the general limit for the resolution of the realized structures in all the mask-based approaches.

The best method to fabricate small structures seems to be combining UV lithography with isotropic etching; an added advantage of this technique is that the same laser can be applied both to deposit and to pattern the films. In our approach, template grooves were created on the film side of the sample with excimer-laser pulses (Fig. 3.17f). The pulses were first diffractively shaped to have a flat-top intensity distribution on the sample surface, and then they passed through a small slit. With this technique, approximately $100 \times 1000 \mu\text{-m}^2$ film-free areas at 500- μm steps could be easily realized. Isotropic etching with water was then applied to create air bridges as demonstrated in Fig. 3.18 and discussed in Paper III. This technique still suffers from water spreading under the film, which makes it difficult to fabricate sub-100- μm components. Large feature size leads also to other problems: the bridges can easily break into two cantilevers. The dimensions of the air bridges and cantilevers can be significantly reduced, e.g., by using diffractive beam-shaping elements to produce a number of evenly spaced, equal-intensity diffraction orders next to each other (see chapter 5) such that the fluence of every order is above the ablation threshold. The results of this approach are shown in Figs. 3.19 and 3.20. The different diffraction orders had a spacing of approximately 100 μm in the film plane, and by properly adjusting the laser fluence, 50 – 70 μm wide film-free areas stripes separated by some 20- μm wide Ni-Mn-Ga stripes could be realized. These results indicate that both of the studied substrate materials are good candidates for the fabrication of tiny FSM components based on air bridges, but with silicon the obtained feature size is much smaller and the etch quality is much better. As mentioned in earlier paragraphs, the films deposited on NaCl had an uneven surface and the film tended to come off from its substrate, which were the two most important reasons why the studied approach worked badly in the case of NaCl. Even with low

fluences, the laser pulses tore off large parts of the film material as can be observed in Fig. 3.19.

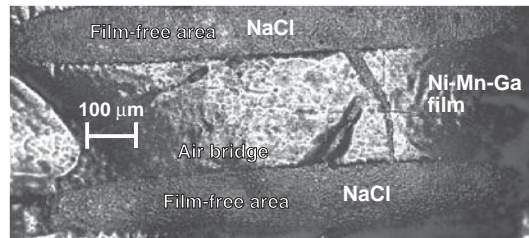


Figure 3.18: Microscope image of an air-bridge structure patterned in a Ni–Mn–Ga film.

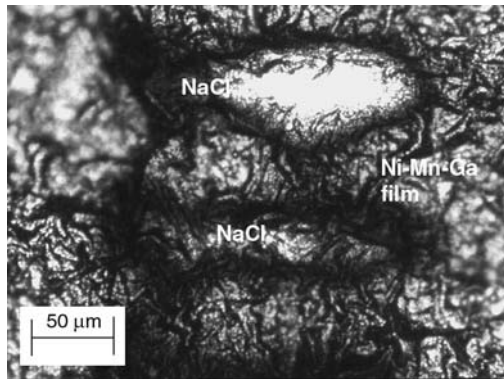


Figure 3.19: Film-free areas on the surface of a Ni–Mn–Ga sample deposited on NaCl. A binary diffractive element that produces 8 equal-intensity diffraction orders was used in these experiments.

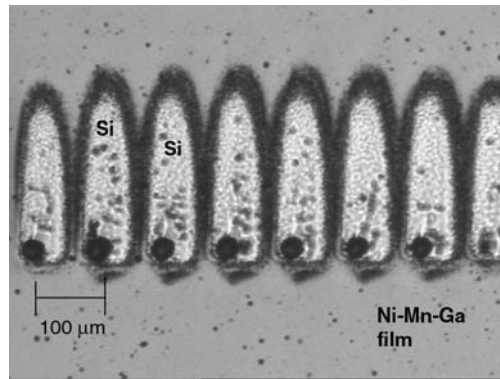


Figure 3.20: Film-free areas on the surface of a Ni–Mn–Ga sample deposited on Si. A binary diffractive element that produces 8 equal-intensity diffraction orders was used also in these experiments.

Chapter 4

Laser-beam shaping

In the latter part of this work, the shaping of coherent and partially coherent laser beams is studied and related experimental results are presented. Beam shaping has already been briefly discussed in Section 3.4 in context of pulsed laser deposition. The goal was to convert the intensity distribution of an excimer-laser beam into a uniform profile with steep edges in the target plane. In addition to PLD, these flat-top beams could be used in other application areas of laser ablation, e.g., in lithographical patterning of small structures, laser machining, and medical surgery [130].

Beam shaping is not only restricted to materials processing but several other fields of physics, chemistry, biology, and medicine would benefit from laser beams whose intensity distribution is different from the standard Gaussian profile. Flat-top or, more generally, super-Gaussian beams are good examples of such "unconventional" distributions, but also beams whose transverse intensity distribution remains unchanged upon propagation have attracted much research interest [22, 23, 25, 148–150]. A particularly interesting goal is the realization of beams with a long and narrow focal line [151]. These Bessel or Bessel-like beams would be advantageous in such applications as pointing and tracking of small objects (surface profilometry) and high-resolution three-dimensional imaging [152], guiding and trapping neutral atoms or nanometer-scaled objects [28, 153–155], precise alignment of optical components and metrological applications [27, 156], real-time medical imaging [157], and addressing atoms in optical lattices without cross-talk [158]. Applications related to laser ablation such as direct-write laser lithography [159], precise laser drilling [29], corneal surgery [160], production of laser plasmas [161], and electron accelerators [162] would also find propagation-invariant fields an attractive alternative, in particular, if one could realize diffraction-free flat-top beams discussed, e.g., in Ref. [163]. Fundamental Bessel and Bessel-Gauss (Bessel beams apodized by a Gaussian envelope function) are particularly suitable for many of the purposes

presented above since they have a bright central maximum and the propagation-invariant range as well as the beam width can be tailored to practically any value. Recently, Bessel beams have been applied in manipulating the motion and locations of tiny particles in optical tweezers [28] and in rotating small objects in optical spanners [151, 164, 165]; the last application is based on the fact that higher-order Bessel beams carry orbital angular momentum and exhibit a phase dislocation at the center of the beam. Optical tweezers and spanners represent the first practical demonstrations of the powerful capabilities of non-diffracting beams.

In this work, the main emphasis is put on diffractive beam shaping. Diffractive optical elements have been designed in close collaboration with University of Joensuu both to create flat-top profiles and to directly produce exact Bessel-Gauss beams in laser resonators. In addition, Bessel-type beams are created by another method: the self-focusing of Gaussian laser beams in a highly nonlinear nematic liquid crystal generates almost diffraction-free beams with a central-peak width of only $5\ \mu\text{m}$ over a distance of more than one millimeter. These three examples are all based on novel but at the same time straightforward and relatively easy techniques to realize the desired intensity profiles. They will be discussed in more detail in chapters 5 and 6.

The flat-top and Bessel-type beams generated during this research work have the following connections to PLD:

- Diffractive optics provides a novel way to transform the intensity distribution of an excimer-laser beam into a flat-top profile on the surface of the ablation target.
- Using diffractive optical elements instead of laser-beam aperturing to generate the desired flat-top will decrease the power losses of our PLD system.
- Flat-top beams as well as Bessel beams can be used to pattern small structures, e.g., in Ni–Mn–Ga thin films. A few hundred μm wide air bridges have already been realized by using flat-top beams as discussed in section 3.5. Furthermore, templates for $< 50\text{-}\mu\text{m}$ wide structures have been created.
- After amplifying and imaging Bessel beams on the target surface, these beams could be used in depositing the films, as well. In principle, the Q -switched Bessel–Gauss pulses studied in section 6.3 are suitable for this purpose but PLD with Bessel–Gauss pulses is beyond the scope of this thesis. Besides, the energy of these ns-long pulses is a few μJ , which is not enough for PLD when the spot size is of the order of a few mm^2 .

Chapter 5

Diffractive shaping of excimer-laser beams

5.1 Theoretical basis

In this section, we derive a formula for the intensity distribution behind a diffractive transmittance grating, in particular, in the focal plane of a positive lens, starting from the Maxwell's equations. This formula is used in simulations to determine the optimal values for the period of the diffractive element and for the distance of the element from the focal plane of the lens such that a flat-top distribution results. It is sufficient to neglect the vector nature of the electric and magnetic fields and use *scalar theory* to describe the behavior of the fields upon propagation. Let us first assume that every field component E can be written in the form

$$E(x, y, z, t) = U(x, y, z)e^{-i\omega t}.$$

In other words, the field is assumed to have a harmonic time dependence in terms of the (angular) frequency ω . The spatial part of the field, $U(x, y, z)$, fulfills the wave equation which in scalar theory reduces to the *Helmholtz equation*:

$$\nabla^2 U(x, y, z) + k^2 U(x, y, z) = 0, \quad (5.1)$$

where $k = \omega/c = 2\pi/\lambda$ is the wave vector and λ is the wavelength. Let us now take $z = 0$ as the reference plane and assume that the field distribution there, $U(x, y, 0)$, is known. The field at distance z can then be calculated from the Fresnel diffraction formula [166]:

$$U(x, y, z) = -\frac{ik}{2\pi z} e^{ikz} \int_{-\infty}^{\infty} \int_{-\infty}^{\infty} U(x', y', 0) e^{ik[(x-x')^2 + (y-y')^2]/(2z)} dx' dy', \quad (5.2)$$

where the primed coordinates refer to the plane $z = 0$. Let us next place a transmittance element, such as a diffractive transmission grating with thickness H , in the incident plane and assume that it has a thin profile. After the element, the field is $U(x, y, H) = t(x, y)U(x, y, 0)$, where the transmittance function of the element, $t(x, y)$, is expressed in terms of its complex refractive index $n(x, y, z)$ [24]:

$$t(x, y) = e^{ik \int_0^H n(x, y, z) dz}. \quad (5.3)$$

Here we assume that the absorption coefficient is negligible (a fully transparent element) such that the imaginary part of $n(x, y, z)$ vanishes. Usually, the element has a certain surface-relief pattern $h(x, y)$ such that

$$n(x, y, z) = \begin{cases} n_1 & , z < h(x, y), \\ n_2 & , \text{otherwise.} \end{cases} \quad (5.4)$$

For elements in this work, n_1 is that of fused silica and $n_2 \approx 1$ (corresponding to air). The phase function of the element, $\phi(x, y) = k \int_0^H n(x, y, z) dz$, can be wrapped between 0 and 2π , and the corresponding surface-relief pattern is [24]

$$h(x, y) = \frac{\phi_{2\pi}(x, y)}{2\pi(n_1 - n_2)} \lambda. \quad (5.5)$$

The phase function is determined by the desired far-field profile and then converted to $h(x, y)$ with this formula. One notices that the relief thickness is typically of the order of λ in all standard optical materials.

Periodic gratings are widely used diffractive optical components for the realization of various field distributions in the target plane. In the case of a thin element, the grating can be described by its transmittance function $t(x, y)$ and be written as a Fourier expansion, which in one dimension is

$$t(x) = \sum_{m=-\infty}^{\infty} T_m e^{i2\pi mx/d}, \quad (5.6)$$

where the Fourier coefficients are

$$T_m = \frac{1}{d} \int_0^d t(x) e^{-i2\pi mx/d} dx \quad (5.7)$$

and d is the element period. The quantity $\eta_m = |T_m|^2$ is the diffraction efficiency of the m^{th} order.

If the incident field at $z = 0$ is a fundamental Gaussian laser beam (TEM₀₀ mode), the Fresnel propagation formula in cylindrical coordinates gives for the field in the output plane (without any diffractive elements) [1, 24]:

$$U(r, z) = U_0 \frac{w_0}{w(z)} e^{ikz} e^{-i\Phi(z)} \exp \left\{ r^2 \left[i \frac{\pi}{R(z)} - \frac{1}{w^2(z)} \right] \right\}, \quad (5.8)$$

where w_0 is the $1/e^2$ beam radius at $z = 0$, i.e., the beam waist,

$$w^2(z) = w_0^2 \left[1 + \left(\frac{\lambda z}{\pi w_0^2} \right)^2 \right] \quad (5.9)$$

is the beam radius at distance z from the waist,

$$R(z) = z \left[1 + \left(\frac{\pi w_0^2}{\lambda z} \right)^2 \right] \quad (5.10)$$

is the radius of the wavefront curvature, and

$$\Phi(z) = \arctan \frac{\lambda z}{\pi w_0^2} \quad (5.11)$$

is the axial phase.

However, excimer-laser beams — which are of interest here — are only partially coherent, which implies that an additional coherence term has to be incorporated into the equations. In the Gaussian-Schell model (GSM), this is done by characterizing the beam by its *cross-spectral density function* $W(x_1, x_2, y_1, y_2, z)$ [24, 167–169]. The generation of directional beams from partially coherent light sources has originally been studied by Collett, Wolf, and Gori, and the GSM is based on their theory presented, e.g., in Refs. [170–172]. The underlying assumption of the GSM is that the intensity and the spatial-coherence distributions of the incident field are of Gaussian form; note that if the spatial coherence is a function of $|\mathbf{r}_1 - \mathbf{r}_2|$ only, the beam is referred to as a Schell-model beam irrespective of the functional shapes of the intensity and coherence distributions.

If the GSM can be applied, the cross-spectral density at $z = 0$ is (in one dimension) [167, 168, 170–172]

$$W(x_1, x_2, 0) = W_0 \exp \left\{ -\frac{x_1^2 + x_2^2}{w_0^2} \right\} \exp \left\{ -\frac{(x_1 - x_2)^2}{2\sigma_0^2} \right\}, \quad (5.12)$$

where σ_0 is the coherence width at the waist. At distance z , the cross-spectral density has been shown to be [167, 169]

$$\begin{aligned} W(x_1, x_2, z) = & W_0 \frac{w_0^2}{w^2(z)} \exp \left\{ -\frac{x_1^2 + x_2^2}{w^2(z)} \right\} \exp \left\{ -\frac{(x_1 - x_2)^2}{2\sigma^2(z)} \right\} \\ & \times \exp \left\{ -\frac{ik(x_1^2 - x_2^2)}{2R(z)} \right\}, \end{aligned} \quad (5.13)$$

where

$$w^2(z) = w_0^2 \left[1 + \left(\frac{\lambda z}{\pi w_0 w_c} \right)^2 \right], \quad (5.14)$$

$$\sigma^2(z) = \sigma_0^2 \left[1 + \left(\frac{\lambda z}{\pi w_0 w_c} \right)^2 \right], \quad (5.15)$$

$$R(z) = z \left[1 + \left(\frac{\pi w_0 w_c}{\lambda z} \right)^2 \right], \quad (5.16)$$

$$\frac{1}{w_c^2} = \frac{1}{w_0^2} + \frac{1}{\sigma_0^2}, \quad (5.17)$$

and

$$\frac{\sigma_0}{w_0} = \frac{\sigma(z)}{w(z)} \equiv \alpha \quad (5.18)$$

When a thin grating is inserted into the beam path in the plane $z = 0$, the cross-spectral density is $W(x_1, x_2, H) = W(x_1, x_2, 0)t^*(x_1)t(x_2)$ and can be written in the form [24]

$$W(x_1, x_2, H) = W(x_1, x_2, 0) \sum_{m=-\infty}^{\infty} \sum_{n=-\infty}^{\infty} T_m^* T_n e^{-i2\pi(mx_1 - nx_2)/d}. \quad (5.19)$$

In many practical beam-shaping systems, the GSM beam is focused with a Fourier-transforming lens. If the lens is placed immediately before or after the element, the cross-spectral density in the back focal plane is [21, 24]

$$\begin{aligned} W(u_1, u_2, f) &= \frac{1}{\lambda f} \int_{-\infty}^{\infty} \int_{-\infty}^{\infty} W(x_1, x_2, H) e^{i2\pi(u_1 x_1 - u_2 x_2)/(\lambda f)} dx_1 dx_2 \\ &= W_0 \frac{w_0}{w_F} \sum_{m=-\infty}^{\infty} \sum_{n=-\infty}^{\infty} T_m^* T_n \exp \left\{ -\frac{(u_1 + mu_0)^2 + (u_2 + nu_0)^2}{w_F^2} \right\} \\ &\times \exp \left\{ -\frac{(u_1 - u_2)^2 + (m - n)^2 u_0^2}{2\sigma_F^2} \right\}, \end{aligned} \quad (5.20)$$

where

$$w_F = \frac{\lambda f}{\pi w_0 \beta} \quad (5.21)$$

is the radius of a single diffraction order in the Fourier plane,

$$\sigma_F = \frac{\sigma_0 w_F}{w_0} \quad (5.22)$$

is the coherence width in the same plane,

$$\beta = \frac{1}{\sqrt{1 + \alpha^{-2}}} \quad (5.23)$$

and

$$u_0 = \frac{\lambda f}{d}. \quad (5.24)$$

The last parameter, u_0 , is the separation between adjacent diffraction orders. If the element is located at distance Δz from the focal plane ($\Delta z < f$), one should replace f by Δz in the definition of u_0 . The intensity distribution takes finally the form

$$I(u) = W(u, u) = I_0 \frac{w_0}{w_F} \sum_{m=-\infty}^{\infty} \sum_{n=-\infty}^{\infty} T_m^* T_n \exp \left\{ -\frac{(u + mu_0)^2 + (u + nu_0)^2}{w_F^2} \right\} \\ \times \exp \left\{ -\frac{(m - n)^2 u_0^2}{2\sigma_F^2} \right\}. \quad (5.25)$$

It is interesting to note that it is straightforward to determine w_0 and w_F experimentally, after which the only parameters whose values have to be optimized are the element period, d , and the working distance, Δz .

5.2 Periodic beam-shaping elements

Diffraction optics provides a powerful way to shape all kinds of laser beams — both coherent and partially coherent — and to realize practically any spatial field distribution in the output plane. In particular, if the desired output consists of a set of discrete spots, periodic elements, i.e., gratings can be used to transform the incident laser beam into such a distribution. Clear advantages of periodic elements are that they are not particularly sensitive to alignment, fluctuations or variations in the beam profile, or the coherence or shape of the incident laser beam [137].

In practical applications, continuous distributions such as flat-top or other non-Gaussian profiles are often preferred to separate laser spots. Periodic elements are a proper solution also to this beam-shaping problem, but in the case of coherent laser beams, their use has certain drawbacks. The most severe of them is that the beamlets the elements produce interfere in the output plane resulting in a fluctuating speckle pattern. Field-mapping techniques discussed, e.g., in Ref. [24] can be applied to get rid of the interference effects but a major disadvantage is that the output distribution is now extremely sensitive to alignment of the diffractive element and changes in the incident beam profile and size.

Excimer-laser beams, on the other hand, are partially coherent, which makes beam shaping with periodic elements very attractive. Now the problems associated with coherent beams become easier to handle: as the coherence width of the beam decreases, i.e., the beam becomes more and more incoherent, the different diffraction orders overlap in the output plane such that finally no disturbing interference results [21].

In our approach, the goal is to convert the excimer-laser beam into a flat-top distribution in the focal plane of a positive lens. A schematic illustration of the technique is shown in Fig. 5.1. A periodic element is placed at a distance Δz from the back focal plane of the lens. The grating produces $2M + 1$ equal-intensity diffraction orders that partially overlap in this plane. The width of the resulting flat-top profile, $2Mu_0$, is determined by the number and spacing of the different diffraction orders, and its steepness is given by the steepness of a single order, i.e., the focused spot. Theoretically, 9 orders maximize the diffraction efficiency to larger than 99 % [173].

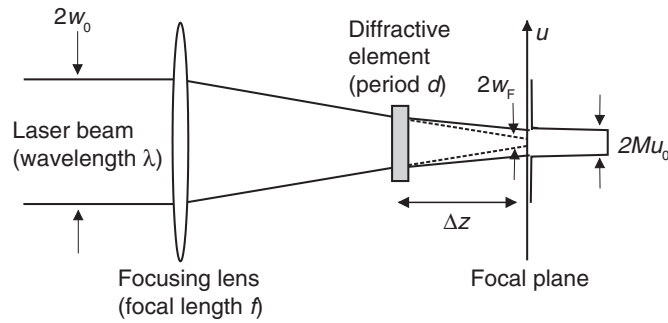


Figure 5.1: Schematic illustration of the technique used in this work to generate flat-top intensity distributions.

The important design parameters of the elements are the $1/e^2$ beam radii of the incident and the focused beams in both transversal directions ($w_{0,x}$, $w_{0,y}$, $w_{F,x}$, and $w_{F,y}$) and the working distance Δz . The beam widths can be determined by fitting Gaussian functions into the measured profiles. Additional restrictions might be set by the actual experiment where the flat-top generator is to be integrated and by the fabrication process of the element.

Together with the necessary input parameters f and λ , the focal length of the lens and the laser wavelength, respectively, the element periods, d_x and d_y , can then be determined with the help of simulations based on Eq. (5.25). The desired depth profile of the element is calculated from the exact diffraction theory, and local deviations from the goal depth should be smaller than 2 % (approximately 10 nm) within an area of $\sim \text{cm}^2$: otherwise the beam energy is not uniformly distributed

between all the diffraction orders. Compared to other beam-shaping approaches, our technique has several advantages:

- it is particularly suitable for partially coherent laser beams such as those of excimer lasers, some diode lasers, or LEDs
- the aspect ratio of the resulting flat-top distribution can be flexibly scaled by using separate diffractive elements for the different transverse directions,
- the whole beam is utilized to generate the flat top,
- the diffraction efficiency is large, and
- the losses come mainly from the surfaces and they can be practically eliminated by properly coating the element surfaces.

5.3 Experimental results

The functionality of the proposed beam-shaping technique was demonstrated by converting the $10 \times 26\text{-mm}^2$ (FWHM, $x \times y$) output beam from the Lambda Physik COMPex 205 KrF excimer laser ($\lambda = 248\text{ nm}$) into a $1 \times 4\text{-mm}^2$ flat-top profile in the focal plane of an $f = 480\text{-mm}$ lens. Note that due to the requirement of a high fluence on the PLD target, the demagnification of the optical system should be large — of the order of 10 in both transverse directions. The $1/e^2$ radii of the original beam are $w_{0,x} = 7.8\text{ mm}$ and $w_{0,y} = 13.9\text{ mm}$ and the corresponding focal radii are $w_{F,x} = 150\text{ }\mu\text{m}$ and $w_{F,y} = 600\text{ }\mu\text{m}$. The coherence widths were determined with the help of Eqs. (5.18), (5.21), and (5.23) to $\sigma_{0,x} = 0.3\text{ mm}$ and $\sigma_{0,y} = 0.07\text{ mm}$.

In the experiments, reported in detail in Paper IV, the x and y directions of the beam were shaped by separate elements with periods of $d_x = 200\text{ }\mu\text{m}$ and $d_y = 50\text{ }\mu\text{m}$ and sizes of $5 \times 8\text{ mm}^2$ and $7 \times 10\text{ mm}^2$, respectively. The elements were fabricated in fused silica using electron-beam lithography and proportional reactive ion etching as illustrated in Fig. 5.2 [174]. The average depth error of the best elements was approximately 2–3 % from the goal values, 510 nm and 506 nm, of the optimized "Mexican-hat" profiles illustrated in Fig. 5.3¹. This is a sufficiently good value for the realization of flat-top beams.

The working distance was set to $\Delta z \approx 100\text{ mm}$ such that the element size would be reasonable for the fabrication process. Fortunately, such a distance does not

¹The optimized goal depth is somewhat larger than the value calculated from Eq. (5.5) with $n_1 = 1.5084$, $n_2 = 1$, $\lambda = 248\text{ nm}$, and $\phi = 2\pi$. This results in a smoother flat-top and makes the fabrication of the grating easier.

cause insurmountable problems. Although in our PLD system the gratings should be placed outside the deposition chamber ($\Delta z \approx 300$ mm), the present elements could be used as well: the resulting distribution is just imaged with another lens on the target surface. However, this approach slightly increases the optical losses of the beam-shaping system. It is interesting to note that, letting fabrication problems aside, the working distance can be easily scaled to, e.g., 300 mm by changing the element period only: multiplying the working distance by three corresponds to two times larger periods for the gratings, i.e., $d_x = 600$ μm and $d_y = 150$ μm .

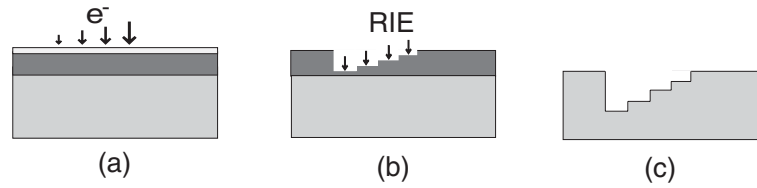


Figure 5.2: Schematic illustration of the fabrication process of multilevel diffractive elements. (a) Spinning a negative resist layer on a fused-silica substrate, coating with a thin aluminum layer, resist exposure by electron-beam lithography, removal of the aluminum layer, resist baking and development. (b) Proportional reactive ion etching (RIE) in a CHF_3 atmosphere. (c) The resulting multi-level profile in fused silica.

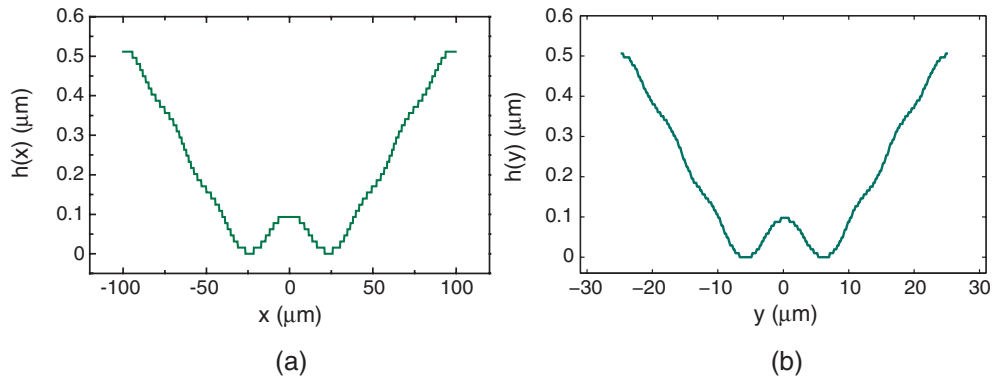


Figure 5.3: Optimized groove profiles ("Mexican hats") of (a) the 200- μm and (b) the 50- μm element.

Figure 5.4 shows the resulting one-dimensional profiles in the shorter x direction with different working distances. The larger the distance, the more clearly the diffraction orders are separated. One notices that their intensities are roughly equal and no extra orders are produced. The optimum value for the working distance, $\Delta z_x = 100$ mm, agrees well with the simulations. When further shortening the distance, the flat-top becomes narrower and narrower finally approaching the profile

of the focused spot as the theory predicts. In addition, practically all of the original intensity is coupled to the flat top: there are no side lobes or tails outside the region limited by the beam edges.

In the y direction, the measured one-dimensional profiles also match well with the simulated curves: the edges are as steep as they should be theoretically and, on the average, the plateau region has the pre-determined width of ~ 4 mm (see Fig. 5.5). Due to small fabrication errors in the element profile, the odd diffraction orders have slightly lower intensities than the even ones and too much power has been coupled to the zeroth diffraction order. This provides an explanation for the observed modulation of the flat-top.

The optimum working distance of the y element was somewhat shorter than that of the x element, $d_y = 95$ mm. This made it possible to obtain a good-quality, two-dimensional flat-top distribution for the PLD experiments by optimizing Δz_x and Δz_y separately. For example, in Paper IV, a 1.4×4.4 -mm² flat-top distribution was obtained by placing the two diffractive elements at $\Delta z_x = 125$ mm and $\Delta z_y = 95$ mm. The resulting one- and two-dimensional profiles are shown in Fig. 5.5. All these results show that the proposed method is a competitive alternative to conventional beam-integrator and field-mapper techniques in creating flat-top beams.

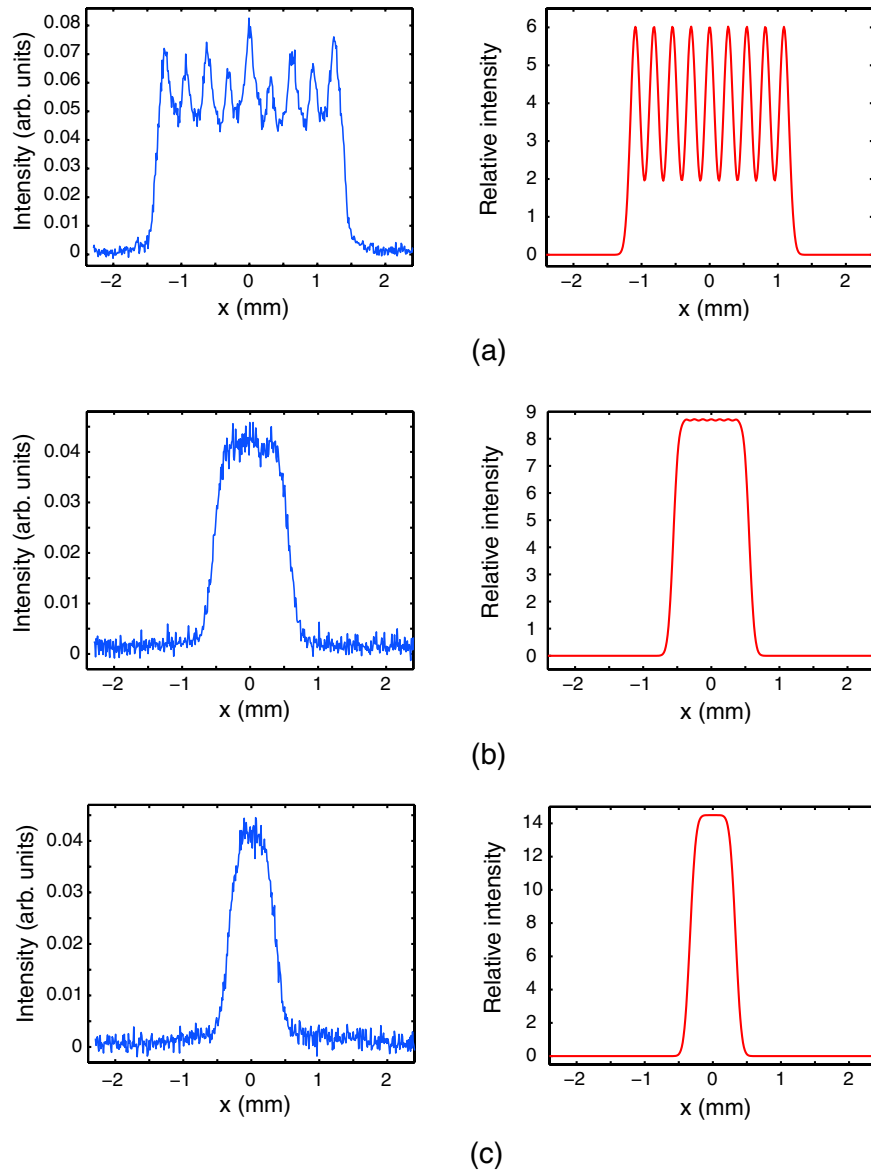


Figure 5.4: Measured (left) and simulated (right) one-dimensional profiles in the narrower x direction. The working distance is (a) $\Delta z_x = 220$ mm, (b) $\Delta z_x = 100$ mm, and (c) $\Delta z_x = 60$ mm.

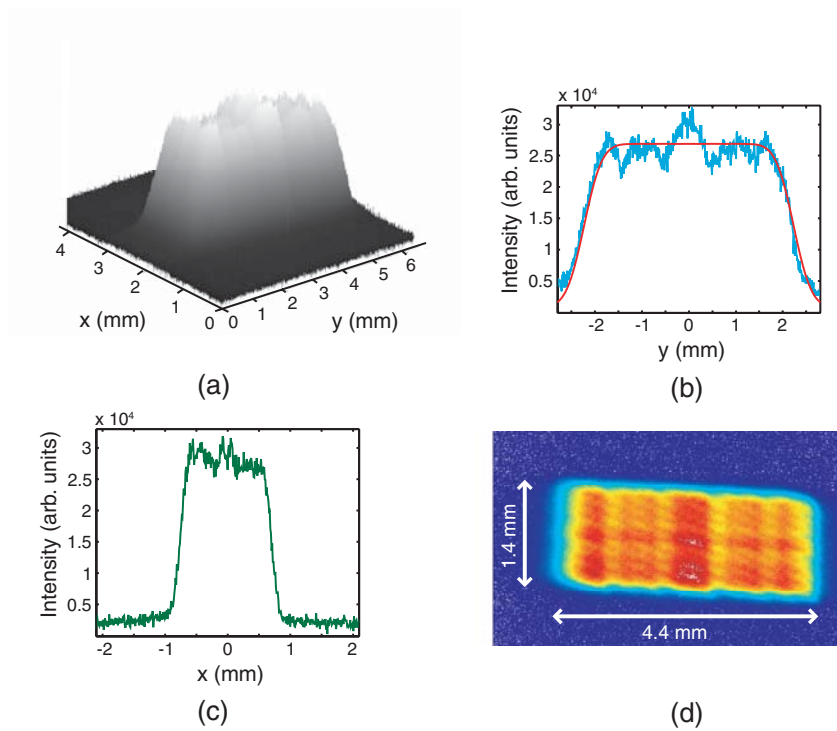


Figure 5.5: (a) Two-dimensional view of the $1.4 \times 4.4\text{-mm}^2$ flat-top distribution. (b) Measured (blue) and calculated (red) cross sections of the distribution in the y direction. (c) Measured cross section of the flat top in the x direction. (d) Another two-dimensional view of the flat top.

Chapter 6

Creation of propagation-invariant laser beams

6.1 Propagation-invariant beams

Propagation-invariant fields are an interesting solution to the Helmholtz equation: contrary to the conventional Gaussian laser beams, these fields retain their shape but also width upon propagation. Mathematically, propagation-invariant fields can be defined as $U(x, y, z) = F(x, y)e^{i\beta z}$; in cylindrical coordinates this expression becomes

$$U(r, \psi, z) = 2\pi e^{i\beta z} \sum_{m=-\infty}^{\infty} i^m \gamma_m e^{im\psi} J_m(\alpha r), \quad (6.1)$$

where β is the propagation constant, γ_m is the m^{th} Fourier component of the angular spectrum, J_m is the Bessel function of the first kind and order m , $\alpha^2 + \beta^2 = k^2$, and k is the wave vector [22,24,175,176]. Due to the fact that the field can be expressed in terms of Bessel functions, propagation-invariant fields are called *Bessel beams*.

Durnin *et al.* [22,175,176] were the first ones who introduced a strictly propagation-invariant field with a J_0^2 intensity distribution and studied the propagation characteristics of such beams. One should, however, note that Bessel beams are special cases of more general self-imaging fields introduced by Montgomery [177] in the 1960's.

The most actively studied of these propagation-invariant modes is perhaps the zeroth-order Bessel beam due to its bright central maximum, which does not spread during propagation. In addition, there are a whole lot of higher-order modes which are considered interesting alternatives to existing laser fields in various fields of optics and

physics. The higher-order modes have a dark central region surrounded by bright intensity rings, owing to which they are sometimes referred to as hollow beams.

Bessel beams belong to the class of conical beams. They can be considered a collection of plane waves, whose wave vectors lie on the surface of a cone with a vertex angle θ . This angle is connected to the beam parameters by the relation $\alpha = k \sin \theta$. Since the beam is composed of plane waves, Bessel fields are infinite and, thus, non-physical. The transverse intensity pattern of the beam consists of concentric rings and because the envelope function of the term $J_m^2(r)$ in this intensity profile is approximately proportional to $1/r$, every ring contains the same amount of energy. The energy content of a Bessel beam is therefore infinite [22, 175, 176].

A physically realizable and mathematically convenient approximation of Bessel fields are Bessel–Gauss beams first described by Gori [148]. Bessel–Gauss fields can be interpreted as Bessel fields apodized by a Gaussian envelope function e^{-r^2/w_0^2} , and due to this apodization, the field remains propagation-invariant only within a finite range z_m . This distance can nonetheless be significantly longer than the Rayleigh range, z_R , of the corresponding Gaussian beam. At the waist, an m^{th} order Bessel–Gauss beam can be written in the form [25]

$$U(r, \psi) = AJ_m(\alpha r)e^{-r^2/w_0^2}e^{im\psi}. \quad (6.2)$$

When $w_0 \rightarrow \infty$, a pure Bessel field is obtained whereas in the case $\alpha = m = 0$, a Gaussian beam results. In analogy with Bessel fields, Bessel–Gauss beams can be regarded as a collection of Gaussian beamlets whose wave vectors also lie on the surface of a cone according to the above-mentioned relation $\alpha = k \sin \theta$.

As the Bessel–Gauss beam propagates, two competing effects determine the behavior of its transverse intensity profile: the conical propagation of the different beamlets (characterized by the vertex angle θ) and their spreading due to diffraction (the divergence angle is approximately $\theta_G = \lambda/(\pi w_0)$) [148]. When $\theta \ll \theta_G$, the beam behaves like a Gaussian beam whereas in the opposite case, a Bessel-like beam with a propagation-invariant distance $z_m = w_0/\theta$ is obtained. According to geometrical optics, at this distance from the waist the Gaussian beamlets have moved a distance w_0 from the central axis such that an annular beam starts to form. In the far field, the intensity distribution of, e.g., a zeroth-order Bessel–Gauss beam has therefore transformed to a ring. The field within and outside the propagation-invariant range can be calculated from the Fresnel propagation formula, which yields

$$U(r, \psi, z) = A \frac{w_0}{w(z)} e^{i\Phi(z)} e^{im\psi} J_m \left(\frac{\alpha r}{1 + iz/z_R} \right) e^{-\left(\frac{1}{w^2(z)} - \frac{ik}{2R(z)}\right)(r^2 + \theta^2 z^2)}, \quad (6.3)$$

where

$$\Phi(z) = \beta z - \arctan \frac{z}{z_R} \quad (6.4)$$

is the on-axis phase, and $w(z)$ and $R(z)$ are the same as for Gaussian beams [25, 148, 178]. The function $\Phi(z)$ differs from that presented in Eq. (5.11) only by an additional term describing the geometric phase of the wave.

The properties of Bessel–Gauss and other approximate Bessel beams, which remain propagation-invariant within a finite range, have been studied by several research groups both theoretically and experimentally [22, 179–183]. In addition, Santarsiero [184] has shown that when *generalized Bessel–Gauss* beams¹ pass through an optical system characterized by its ABCD matrix their mathematical expression remains the same but the propagation-invariant range and the width of the central region can change. For example, by imaging an ordinary zeroth-order Bessel–Gauss beam with two lenses from the front focal plane of the first one to the back focal plane of the second one, the propagation-invariant range z_0 scales to $z'_0 = (f_2/f_1)^2 z_0$, where f_2 and f_1 are the focal lengths of the two lenses. Simultaneously, the radius of the Gaussian envelope is increased to $w'_0 = (f_2/f_1)w_0$. Some reports have also been published on extending the theory of propagation-invariant fields to partially coherent laser beams. For instance, Palma *et al.* [185] have considered Schell-model beams whose complex degree of spatial coherence is propagation-invariant.

6.2 Methods to realize propagation-invariant beams

Due to their interesting properties and possible applications, several approaches to create approximations of the Bessel beams have been suggested and realized. The original idea by Durnin *et al.* [22, 175, 176] was to use an annular aperture with radius R followed by a focusing lens at a distance f (where f is the focal length of the lens) from it to generate an approximate J_0 Bessel beam within the range z_m . A much more widely-used approach to create such beams, however, is to use *axicons*, either refractive or diffractive [151]. Refractive axicons were introduced as early as in 1954 by McLeod [186, 187] to generate long and narrow focal lines. Originally, axicons were simply glass cones which imaged a point source to a series of points along the cone axis, i.e., they produced a line focus behind the component. Diffractive axicons, on the other hand, are circular gratings or, more generally, computer-generated holograms, which produce the desired line segment much more flexibly than the bulky pieces of glass in the McLeod’s idea [23, 153, 155, 156, 188].

The length of the focal-line segment the axicons produce is proportional to the aperture R of the element and the vertex angle θ , and the conversion efficiency depends on the transmittance function of the element. Although axicons are an effective tool

¹Generalized Bessel–Gauss beams are characterized by the distribution $U(r, \psi) = AJ_m((\alpha - 2ia/w_0^2)r) \exp(-(r^2 + a^2/w_0^2))$, where a is a positive parameter.

in generating approximate Bessel or Bessel–Gauss beams, their use has some drawbacks. Since one is often interested in obtaining a narrow and uniform diffraction-free beam within a reasonably long range, an annular aperture or an apodizing mask has to be inserted in front of the axicon [189]. This leads to poor conversion efficiency and induces losses to the beam-shaping system. In addition, the generated Bessel-type field typically suffers from axial non-uniformity, the axicons are sensitive to alignment, and the production of high-quality diffractive gratings requires careful optimization of the fabrication process [179–181, 190–193]. One should also keep in mind that for the successful generation of Bessel beams, the aperture of the axicon should be much larger than the $1/e^2$ radius of the original Gaussian laser beam.

Other techniques to realize Bessel-type laser beams include using toroidal lenses and diffractive phase filters instead of ring-shaped apertures [194]. Two-component diffractive systems or axicons to realize Bessel beams and to suppress oscillations in the axial intensity have also been proposed [192, 193].

Bessel fields and their linear combinations are eigenmodes of an infinite Fabry–Perot resonator [195]. This has inspired many groups to design laser resonators, whose output would be a Bessel-like beam [196–201]. However, only a few experimental demonstrations have been reported. Uehara and Kikuchi [149] have used a cavity with a focusing lens and an annular mirror to create approximations of the fundamental Bessel–Gauss beam. In the paper by Khilo *et al.* [150], a dye solution was pumped with a 532-nm laser beam in a linear cavity where an axicon was placed close to one of the cavity end mirrors. Pääkkönen and Turunen have studied aspheric-mirror resonators [202–204] to produce approximate Bessel fields [25]. These ideas were experimentally verified in Paper V by designing and building a laser resonator with the exact zeroth-order Bessel–Gauss beam as the output field.

In recent years, the possibility to create narrow (width only a few μm) focal lines with a length of several millimeters and hollow laser beams in highly nonlinear nematic liquid crystals has become an interesting research area [205, 206]. The approach is based on the self-phase modulation of a Gaussian laser beam in the liquid crystal. As the beam undergoes self-focusing, the focal region can have Bessel-like field characteristics. At the moment, it is not known for certain, whether the self-focused field can be mathematically expressed in terms of Bessel functions or does the generated beam have characteristics of another beam whose far-field ring pattern resembles that of a Bessel beam.

6.3 Bessel–Gauss beams from a laser resonator

6.3.1 Resonator design

Let us consider a simple resonator configuration schematically shown in Fig. 6.1. The mirror M1 is semitransparent through which the laser crystal is pumped and the mirror M2 is a fully reflecting aspheric mirror. In the simplest design, M1 is planar and M2 has an effective radius of curvature, R , although typically this other mirror is a diffractive phase element.

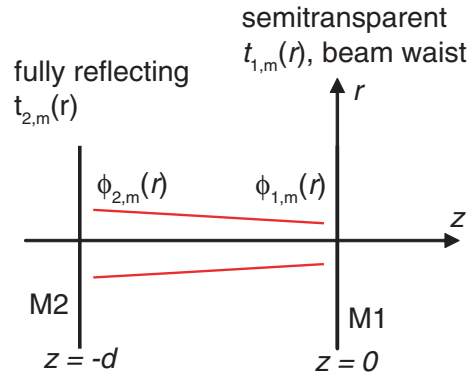


Figure 6.1: Schematic illustration of the resonator configuration used in generating a zeroth-order Bessel–Gauss output beam.

The field of the desired mode is assumed to be separable such that

$U_m(r, \psi, z) = u_m(r, z)e^{im\psi}$ [25]. The mirror M2 has a complex-amplitude transmittance — or reflectance — function

$$t_{2,m} = \frac{u_m^*(r, -d)}{u_m(r, -d)}. \quad (6.5)$$

In other words, the mirror conjugates the radial phase of the field. Similarly, at M1 the transmittance function is

$$t_{1,m} = \frac{u_m(r, 0)}{u_m^*(r, 0)}. \quad (6.6)$$

The waist of the Bessel–Gauss mode is located at M1, and if M1 is a planar mirror such that $t_{1,m} = 1$ for all m , then at M2 the Fresnel propagation formula² gives [25]

$$t_{2,m} = \exp \left\{ i \left[2\Phi(d) + \frac{k(r^2 + \theta^2 d^2)}{\lambda R(d)} \right] \right\} J_m \left(\frac{\alpha r}{1 + id/z_R} \right) J_m^{-1} \left(\frac{\alpha r}{1 - id/z_R} \right). \quad (6.7)$$

²The (paraxial) Fresnel diffraction formula can be applied since we implicitly assume that the central peak is much wider than the wavelength.

The notations here are the same as in section 6.1. By making use of the mathematical properties of Bessel functions, $t_{2,m}$ can be written in the form

$$t_{2,m} = e^{i\phi_{2,m}(r)}, \quad (6.8)$$

where the phase function is [25]

$$\phi_{2,m}(r) = 2\Phi(d) + \frac{k\theta^2 d^2}{R(d)} + \frac{kr^2}{R(d)} + 2 \arg \left[J_m \left(\frac{\alpha r}{1 + id/z_R} \right) \right]. \quad (6.9)$$

The first two terms are proportional to the resonator parameters whereas the last two ones represent the paraxial phase of a corresponding spherical mirror and the asphericity of M2, respectively. For instance, if $\alpha = 0$, then $\phi_{2,m} \rightarrow 2kd - 2 \arctan(d/z_R) + kr^2/R(d)$, i.e., the phase of a spherical mirror in a conventional resonator with a Gaussian output beam. If $w_0 \rightarrow \infty$ implying that $z_R \rightarrow \infty$, one obtains $\phi_{2,m} \rightarrow 2\beta d$, which corresponds to the phase of a planar mirror in a Fabry–Perot resonator. Note that when $d \rightarrow 0$, $R(d) \rightarrow \infty$ and $\phi_{2,m} \rightarrow \text{constant}$ whereas in the case $d \rightarrow \infty$, $\phi_{2,m} \rightarrow Ar + B$, which is the phase of an axicon [24]. This relation shows that axicons can be used instead of aspheric mirrors to produce approximations of the Bessel–Gauss fields provided that the field at the axicon is essentially the far field.

6.3.2 Experimental setup

A schematic illustration of the actual Bessel–Gauss laser is shown in Fig. 6.2. As the laser material, we used Nd-doped YAG, YVO₄, and YLF crystals; the dimensions, doping levels, and other physical properties including the pump and laser wavelengths of these three crystals are presented in Table 6.1. The crystals were end pumped by either a 2-W JDS Uniphase 2462 diode laser at 808 nm or a 4-W Unique-m.o.d.e. UM4000/100/20 diode operating at 798 nm or at 795 nm.

The resonator was a simple linear cavity as described in the previous subsection and in Paper V. One end of the laser crystal — the mirror M1 — was HR (high-reflectivity) coated for the laser wavelength and AR (anti-reflection) coated for the pump wavelength. The other end was AR coated for the laser wavelength. The mirror M2 was a diffractive element with an effective radius of curvature of $R \approx 10$ cm. This 2.7-mm-diameter mirror was patterned in fused silica at University of Joensuu using the standard electron-beam-lithography and proportional reactive-ion-etching techniques [174]; 32 phase levels were used when exposing the element to obtain a nearly continuous phase profile as shown in Fig. 6.3. The corresponding depth profile was calculated from Eq. (5.5) by inserting $n_1 = 1$ and $n_2 = -1$ (the case of a reflectance element). The goal depth of the element was

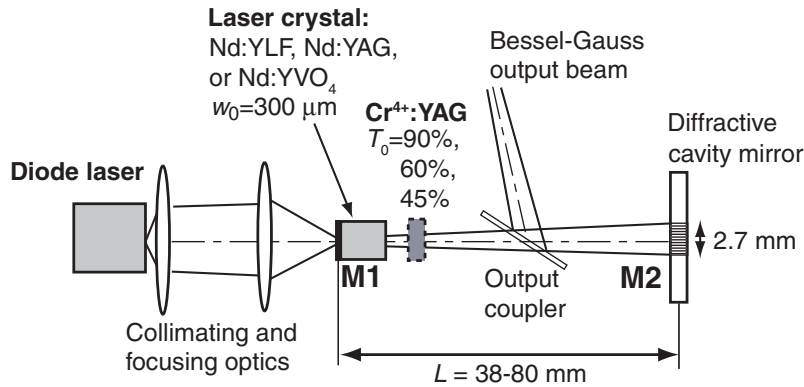


Figure 6.2: Schematic illustration of the laser cavity designed to be an active source for the fundamental Bessel–Gauss mode.

thus $\lambda/2$, and since Nd:YAG was used in the very first experiments, this value was chosen to 532 nm. However, since the lasing wavelengths of the different crystals do not differ significantly from each other, the same element was successfully used with all the laser crystals. Finally, the element was coated with a 130-nm-thick layer of gold such that the reflectivity at 1047 – 1064 nm would be of the order of 99 %.

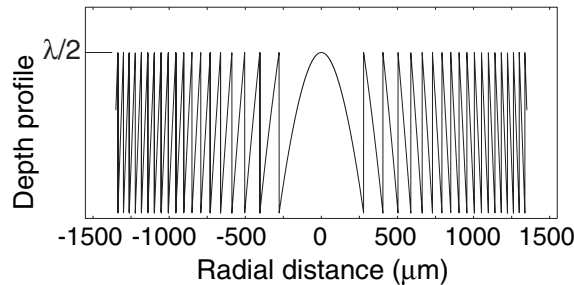


Figure 6.3: Depth profile of the diffractive cavity mirror.

In an 8-cm resonator, the waist radius of the Bessel–Gauss mode is $w_0 \approx 300\ \mu\text{m}$. Together with the design value for the cone angle, $\theta \approx 3.75\ \text{mrad}$, the propagation-invariant range becomes $z_0 \approx 80\ \text{mm}$. This value was selected on the basis of Fox–Li simulations such that a good modal discrimination could be obtained [24, 25]. Furthermore, by using such a “small” value for z_0 , it becomes easier to distinguish the resulting distribution from a Gaussian beam.

In practical applications, the range z_0 should be relatively long and, in addition, the propagation-invariant range should be larger than the Rayleigh range, $z_R = \pi w_0^2/\lambda$, of the corresponding Gaussian beam with the same waist radius. In our case,

$z_R \approx 266$ mm which is three times the propagation-invariant range of the generated Bessel–Gauss field. By using a telescope, the distance z_0 can be scaled to practically any value but, unfortunately, at the same time the width of the corresponding Gaussian beam and, thus, the Rayleigh range increase. If the beam is imaged, e.g., with two lenses such that $f_2 = 2f_1$, the propagation-invariant range can be extended to 320 mm but the beam radius increases to $w'_0 = 600 \mu\text{m}$. The selected propagation-invariant range should thus be considered only as an example. Longer ranges are obtained by reducing the cone angle of the beam.

The simulations showed — and this was also experimentally verified — that the mode was not sensitive to the resonator length, at least within the range 20–80 mm. In many of the performed experiments, the cavity length was much shorter than the selected $z_0 = 80$ mm, which makes our approach superior to the techniques based on intracavity axicons.

An optional, passively Q -switching Cr^{4+} :YAG crystal for the production of ns-long Bessel–Gauss pulses is also shown in Fig. 6.2; the initial transmissions of these crystals ranged from 45 % to 90 %. In Q switching, a shutter is introduced in the cavity to prevent the laser action such that the population inversion would be maximized during pumping. If the shutter is now opened suddenly, the laser gain greatly exceeds losses, and practically all of the stored energy is released in a short and intense light pulse. Q switching can be realized either actively by using, e.g., mechanical shutters or acousto-optical switches or passively with the help of saturable absorbers such as Cr^{4+} :YAG. Passive Q switching is based on the bleaching of the saturable absorber at low intensities. When the intensity in the cavity exceeds the saturation value of the absorber, I_S , the absorption coefficient drops, the material becomes more transparent, and the laser intensity starts to grow exponentially. When the cavity photon number has reached a sufficiently high value, the population inversion begins to be depleted, and when it has dropped below its threshold value, the laser will have losses in excess of gain and the pulse starts to decrease exponentially. Finally, the photon number goes to zero, the population inversion decreases to a final value, and the transmission coefficient of the absorber is restored to its initial value [1].

The production of short and energetic Q -switched pulses would be an interesting future application area of our Bessel–Gauss laser since this area has gained much research interest during the past few years (see Refs. [207–212]). Several reports have been published, e.g., on the modelling and operation of passively Q -switched Nd:YAG and Nd:YVO₄ microchip lasers. With these lasers, the pulse duration can be scaled down to a few tens of picoseconds and the pulse energy up to hundreds of microjoules but both of the goals cannot be reached simultaneously [207–209]. Such pulses can be used in PLD and other application areas of laser ablation.

6.3.3 Results

The CW operation of the Bessel–Gauss laser was demonstrated with all the laser crystals mentioned in the previous subsection. The results obtained with YAG and YVO₄ have been published in Paper V whereas those achieved with the YLF crystal can be found in Ref. [218].

In the case of YAG and YVO₄, the strongly diverging pump beam of the 2-W diode laser (divergences in the directions perpendicular and parallel to the diode junction were $\theta_{\perp} = 12^{\circ}$ and $\theta_{\parallel} = 32^{\circ}$, respectively) was collimated by a positive lens with a focal length of 8 mm and focused by another lens (focal length 5 mm) such that the beam radius at the crystal was $w_p \approx 100 \mu\text{m}$. Approximately 95 % of the pump power was absorbed in the crystal in this configuration, and since the diode drive current was limited to 2 A, the maximum value for the absorbed power was ≈ 1.2 W. In the case of YVO₄, the pump beam was σ polarized before the crystal since the absorption coefficient for this polarization is about two times higher than for π polarization (see Table 6.1).

The laser operation was obtained at an absorbed pump power of 265 mW with the YAG rod, and when using the YVO₄ plate, the threshold power was approximately half of this value. This is in accordance with the theory by Fan and Byer [219]: the threshold pump power is inversely proportional to $\sigma_e \tau \eta_p$ where σ_e is the stimulated-emission cross section, τ is the upper-state lifetime, and η_p is the pump quantum efficiency, i.e., the number of Nd ions in the upper laser level created by a single absorbed photon.

When using the YLF crystal, the pump beam from the 4-W diode laser was coupled to a single-mode fiber. After that, the beam was collimated and focused with aspheric lenses (with focal lengths of 8 and 11 mm or 4.6 and 11 mm). Accordingly, the beam radius in the crystal ranged from 50 to 100 μm . Since the output of the diode is unpolarized and the cross section of YLF depends on the polarization of the pump beam, only 70 % of the pump power was absorbed in the crystal. However, the maximum pump power of the diode was so high that the obtained laser power was comparable to that of the YAG- and YVO₄-based lasers. As one would expect on the basis of Table 6.1, the threshold pump power of the YLF laser was approximately the same as that of the YAG laser, i.e., 250 mW — the product of the stimulated-emission cross section and the upper-state lifetime is practically the same for both of the materials.

The laser beam was coupled out from the resonator by a wedge-shaped plate. The output coupling was not optimal and, therefore, the power could be measured only in the case of the YLF crystal at sufficiently high pumping levels. At an absorbed pump power of 1400 mW, the combined power of the two output beams — reflections from the back and front sides of the wedge plate — was 230 mW. This modest

Table 6.1: Physical properties, dimensions, and doping levels of the laser crystals used in the experiments [209, 213–217].

	Nd:YAG	Nd:YLF	Nd:YVO ₄
Nd doping (%)	1	1	2
Crystal dimensions (mm)	length 5, diam. 3	3 × 3 × 5	3 × 3 × 1.2
Laser wavelength (nm)	1064	1047 (π)	1064 (π)
Pump wavelength (nm)	808	797	810
Absorption coefficient, for [Nd]=1.0 % (cm ⁻¹)	4 – 7.2	5 (σ) 3.3 (π)	31.2 (σ) 9.2 (π)
Upper-state lifetime, for [Nd]=1.0 % (μ s)	230	480	90
Stimulated-emission cross section (cm ²)	2.6×10^{-19}	1.8×10^{-19} (π)	25×10^{-19} (π)
Refractive index (@ 1 μ m)	$n = 1.82$	$n_o = 1.448$ $n_e = 1.470$	$n_o = 1.9573$ $n_e = 2.1652$
dn/dT ($10^{-6} \times K^{-1}$)	7.3 – 9.9	-4.3	3
Thermal expansion coefficient ($10^{-6} \times K^{-1}$)	8.2	8.3	11.4
Thermal conductivity (WK ⁻¹ m ⁻¹)	13	6.3	5.2

value could be scaled up by changing the simple linear resonator configuration to an L- or V-shaped cavity and inserting an optimized output-coupling mirror, e.g., at the tip of the "V". Another possibility is to use a partially transmitting end mirror as M1 and install a suitably coated beam splitter between the collimating and focusing lenses to couple out the beam from the laser.

Figure 6.4 gives examples of one- and two-dimensional intensity profiles of the output-coupled beam at different distances from the beam waist in the case of the YLF crystal. In addition, the corresponding theoretical profiles calculated from the Fresnel propagation integral are shown in the right column of the figure. The images show that close to the beam waist (1 cm, Fig. 6.4a), the first minimum is reached at approximately $r \approx 100 \mu\text{m}$ (theoretical value $108.6 \mu\text{m}$), and the ratio of the intensities of the first and secondary maxima behaves similarly to the theoretical predictions within the propagation-invariant range (see Fig. 6.4b which is taken at 6 cm from the waist). In the far field ($z_{\text{ff}} = 38 \text{ cm}$), the profile has transformed to a ring with a peak-to-peak diameter of $2r_{\text{ff}} = 2.5 - 2.6 \text{ mm}$ (see Fig. 6.4c). The cone angle of the beam is approximately $\theta \approx r_{\text{ff}}/z_{\text{ff}} \approx 3.3 - 3.4 \text{ mrad}$ — in accordance with the estimate, $\theta_{\text{th}} = 3.6 \text{ mrad}$ calculated from the corresponding theoretical distribution. The measured profiles are slightly asymmetric, which is most probably due to spherical aberrations induced by small fabrication errors in the depth profile of the diffractive mirror. These errors also explain why the secondary maxima and minima in the profiles measured at 6 cm from the waist are higher than they should be. A small average depth error ($\approx 2 \%$) from the goal value was also measured but it did not have a noticeable effect on the laser operation.

Numerical simulations showed that a constant error from the goal depth of the diffractive element increases the intracavity losses by several per cent; for instance, a 10-% error would lead to an additional optical loss of 20 %. On the other hand, an error smaller than 3 – 5 % seems not to have a significant effect on the threshold pump power or the obtained output power. This is evidenced by the fact that the Bessel–Gauss laser worked also with the YLF crystal although the optimal depth in this case would be 523.5 nm — a 1.6-% deviation from the design value of 532 nm — and the error from the real average depth (543 nm) is thus larger than 3.7 %. This suggests that the functionality of the laser is above all dependent on the proper realization of the groove profile of the diffractive element, not so much on the absolute value of the average depth.

The passively Q -switched operation of the Bessel–Gauss laser was also demonstrated with the YLF crystal by inserting saturable Cr^{4+} :YAG absorbers with different initial transmissions into the cavity (see Fig. 6.2). To protect the crystal from excessive thermal load which might be of problem due to the poor thermal conductivity of YLF ($6.3 \text{ Wm}^{-1}\text{K}^{-1}$ compared to $13 \text{ Wm}^{-1}\text{K}^{-1}$ for YAG), a quasi-CW pumping scheme was applied: the laser crystal was pumped with 1-ms pulses at a

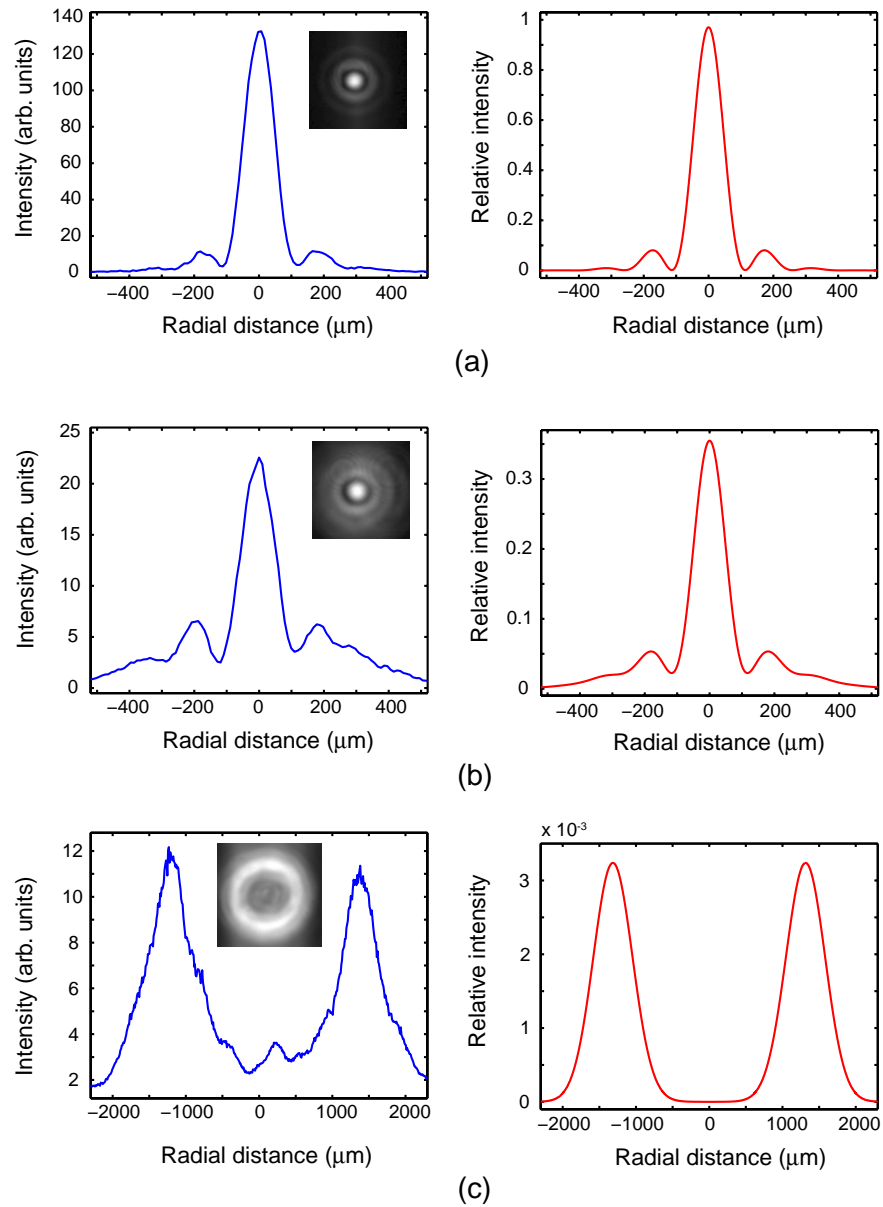


Figure 6.4: Measured radial intensity profiles together with two-dimensional CCD images (left) and theoretical profiles (right) of the Bessel–Gauss beam at (a) 1 cm, (b) 6 cm, and (c) 38 cm from the waist.

200-Hz repetition rate. The power level was adjusted such that a single Q -switched pulse was obtained during each pumping interval. The pulse widths as well as the repetition rates were determined with the help of a fast photodiode and a 1-GHz oscilloscope (Tektronix TDS 5104); the temporal resolution of this system was 2 ns. The pulse energies were evaluated from the measured average powers and repetition rates.

By using a Q -switching crystal with an initial transmission of $T_0 = 90\%$ and an 80-mm cavity, two beams of 30-ns-long pulses with energies of $3\ \mu\text{J}$ and the correct Bessel–Gauss-type profile within the whole propagation-invariant range were obtained. By shortening the cavity length down to 3.8 cm (which was the shortest possible length in our setup), the intensity profiles of the generated pulses matched still well with the corresponding CW curves. By using darker Cr^{4+} :YAG crystals with $T_0 = 60\%$ or $T_0 = 45\%$ in the short cavity, the pulse durations dropped to approximately 5.6 ns and 3 ns, respectively, while the pulse energy increased to $7.5\ \mu\text{J}$ with the darkest crystal. However, although the intensity profiles of such short pulses were very similar to the results obtained for longer pulses within the 8-cm propagation-invariant range (see Fig. 6.5d), the far-field profiles at 38 cm from the waist were significantly different: as Fig. 6.5 shows, an additional central peak starts to evolve as the initial transmission of the Q -switching crystal and, simultaneously, the pulse duration decrease. The most probable explanation to this behavior is that the number of round trips in the cavity is insufficient to form the desired Bessel–Gauss mode. Another possibility is that the radial transmission of the saturable absorber changes during the Q -switched pulse — an effect studied by Arvidsson [220] in a passively Q -switched Nd:YAG laser. These results, however, are the first demonstration of Bessel–Gauss pulses and as Fig. 6.5 shows, they have the desired intensity profile within the whole propagation-invariant range.

6.4 Generation of Bessel-like laser beams in liquid crystals

6.4.1 Theory

The generation of Bessel-like beams in liquid crystals results from the *self-focusing* of Gaussian laser beams. At high intensities, the refractive index of a medium, n_0 , is modified such that $n = n_0 + n_2 I$, where n_2 is a material-dependent positive coefficient (for instance, $n_2 \approx 4.5 \times 10^{-16}\ \text{cm}^2/\text{W}$ for fused silica). This dependence on intensity induces a nonlinear phase shift that in the case of a Gaussian profile is $\delta\phi = (2\pi n_2 l I_p / \lambda) e^{-2(r/w)^2} \approx (2\pi n_2 l I_p / \lambda) [1 - 2(r/w)^2]$, where l is the length of the medium and I_p is the peak intensity of the laser beam. This phase shift is

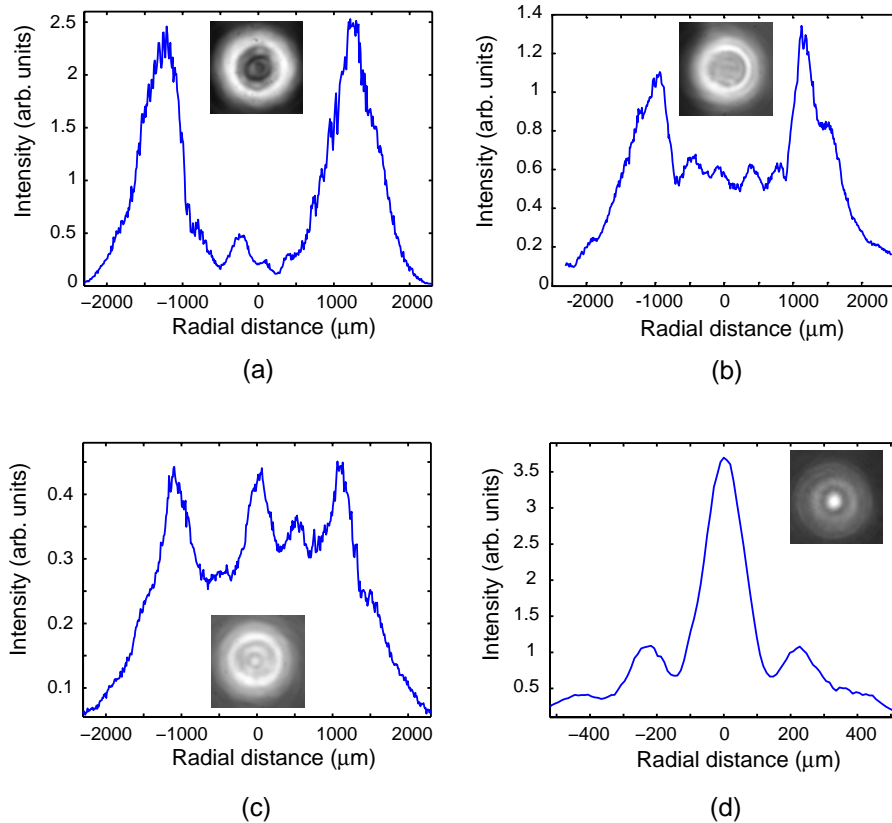


Figure 6.5: Measured radial intensity profiles together with two-dimensional CCD images (insets) of the generated Bessel–Gauss pulses. The far-field patterns were taken at 38 cm from the waist by using a Cr^{4+} :YAG crystal with an initial transmission of (a) 90 %, (b) 60 %, and (c) 45 %. (d) shows the intensity profile at 85 mm from the waist in the case of the darkest crystal.

equivalent to that introduced by a positive lens. The induced lens then leads to the beam focusing as the power exceeds a critical value. The phenomenon is known as self-focusing, and the modulation of the phase of the incident beam is referred to as *self-phase modulation* [1].

The theory for the behavior of self-focused Gaussian laser beams in a liquid crystal is based on two assumptions: the incoming beam is normally incident on the crystal, and the crystal is assumed to be thin such that the field behind the crystal is essentially the same as at the input face. The field distribution can again be calculated by using the Fresnel diffraction integral. Shevchenko *et al.* [205, 206] have presented a theoretical model for the propagation by noticing that a self-focused Gaussian beam behaves as if it was formed by a converging hollow beam in the region $z < 0$, i.e., before the liquid crystal. Since the field for this virtual hollow beam is similar to

that produced by an annular aperture, it is expected that at the focus the self-focused field would be Bessel-like, i.e., it would have a very low divergence. Based on this modelling, the complex amplitude of the field³ in the region $z > 0$ is written in cylindrical coordinates as

$$U(r, z) = \frac{2\pi}{\lambda z} \int_0^\infty U(0, \rho) e^{i\pi\rho^2/(\lambda z)} J_0\left(\frac{2\pi r \rho}{\lambda z}\right) d\rho \quad (6.10)$$

and

$$U(0, \rho) = \sqrt{I_p} e^{-\rho^2/w_{LC}^2 + i\phi(\rho)},$$

where I_p is the peak intensity of the original laser beam and w_{LC} is its $1/e^2$ radius in the crystal. The phase function $\phi(\rho)$ depends on I_p , w_{LC} , the crystal thickness L , the nonlinear refractive index n_2 , the location of the crystal with respect to the beam waist, and the radius of the wavefront curvature in this point (R_{LC}). A reasonably accurate model for the phase is [26]

$$\phi(\rho) = \frac{2\pi}{\lambda} L n_2 I_p e^{-2\rho^2/w_{LC}^2} + \frac{\pi\rho^2}{\lambda R_{LC}}.$$

The intensity profile calculated from Eq. (6.10) is shown in Fig. 1 of Paper VI. The profile is obtained by using the values of the actual experimental setup ($\lambda = 532$ nm, $w_{LC} = 220$ μ m, $R_{LC} = -39$ mm, $L = 100$ μ m, $n_2 = 3 \times 10^{-5}$ cm²/W, and $I_p = 1.7 \times 10^3$ W/cm²). The profile has a narrow peak ($w < 5$ μ m) with a high intensity ($I \approx 6 \times 10^5$ W/cm²) at $z \approx 2.8$ mm. Note that in the absence of the liquid crystal, a waist radius of 30 μ m would be obtained at a distance of 38 mm from it. This clearly shows how the nonlinear lens shapes the incoming beam. As the self-focused beam propagates an additional distance of 4.5 mm, the central-peak intensity drops by a factor of 10 whereas the width remains essentially unchanged. Compared to a Gaussian beam with the same waist radius of 5 μ m, this is a clear advantage: the radius of the Gaussian beam at 4.5 mm from the waist would be almost 150 μ m and the intensity only 0.1 % of that in the waist. In Paper VI, it has been concluded that the self-focused beam looks Bessel-like and spreads slowly due to the fact that the liquid crystal acts as a kind of collection of axicons with different cone angles and diffraction-free ranges.

6.4.2 Experimental

The diffraction-free properties of the self-focused Gaussian beam were studied by using the beam coming out from a frequency-doubled diode-pumped Nd:YVO₄ laser (Spectra Physics Millennia Xs) and focusing it to the liquid crystal with the

³The unessential phase factor $-i \exp[ik(z + r^2/2z)]$ has been left out in front of the integral.

setup shown in Fig. 6.6. The beam radius at the laser output is $w_0 = 1150 \mu\text{m}$, the focal length of the lens L_1 is 200 mm, and the crystal is placed at a distance of 162 mm from it. With this setup, the w_{LC} and R_{LC} had the same values as in the example of the previous subsection. The liquid crystal was pressed between two glass plates and its thickness was approximately $100 \mu\text{m}$. The crystal was homeotropically oriented in the nematic phase and its nonlinear refractive index was $n_2 = 10^{-5} \text{ cm}^2/\text{W}$. The resulting beam profiles were imaged with the lens L_2 onto a CCD camera; in these experiments, the imaging lens was a $20\times$ microscope objective, and according to Fig. 6.6, the total magnification of the imaging system was $M = 21.2$.

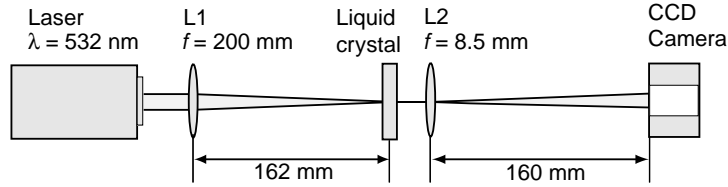


Figure 6.6: Schematic illustration of the experimental setup used for the generation of Bessel-like laser beams.

The peak intensity of $1.7 \times 10^3 \text{ W/cm}^2$ was obtained with a CW power of 1.3 W. This value is well above the self-focusing threshold of our liquid crystal [206]. The response time of the crystal is inversely proportional to L^2 , and in our case it was of the order of minutes. To accelerate the transition process, the laser power was first increased to 2 – 3 W and when the diffraction rings in the far field started to form, the power was rapidly decreased to the goal level. After the beam had stabilized, one- and two-dimensional images of its intensity distribution were taken by translating the imaging system consisting of the lens L_2 and the CCD camera at $500\text{-}\mu\text{m}$ steps along the optical axis. The results in Fig. 6.7 show that the self-focused beam behaves qualitatively similarly to an approximate Bessel beam upon propagation although it spreads more than Eq. (6.10) predicts. By taking into account the magnification of the imaging system, $M = 21.2$, the central-peak radii at 0, 1.5, and 4.5 mm from the major central peak were 4.8, 5.8, and $9.8 \mu\text{m}$, respectively, whereas the theory predicts that the radius should hardly change at all. This clearly shows that the presented model is an oversimplification of the true situation but, nevertheless, it gives reasonably accurate estimates for the shape of the intensity profile.

Like the Bessel–Gauss beam presented in section 6.3, the output beam from the liquid crystal is not perfectly symmetric, either, and it shows a double-ringed intensity pattern. This is in agreement with the results of Jaroszewicz *et al.* [156] who concluded that an asymmetric laser beam or a misaligned experimental setup induce

aberrations to the beam. In addition, back reflections from the imaging lens may disturb the self-phase-modulation process in the liquid crystal. Interesting observations were also that the larger the beam radius at the crystal, the longer the Bessel-like beam is produced and the higher the laser power, the narrower but shorter focal line results. In addition, by using π -polarized light, the threshold power for the onset of self-focusing depended on the tilting angle of the crystal, which is probably associated with the response of the liquid-crystal molecules to the incoming electric field. All these examples show that it is straightforward to adjust the dimensions of the generated beam and obtain a very narrow beam with a large depth of focus.

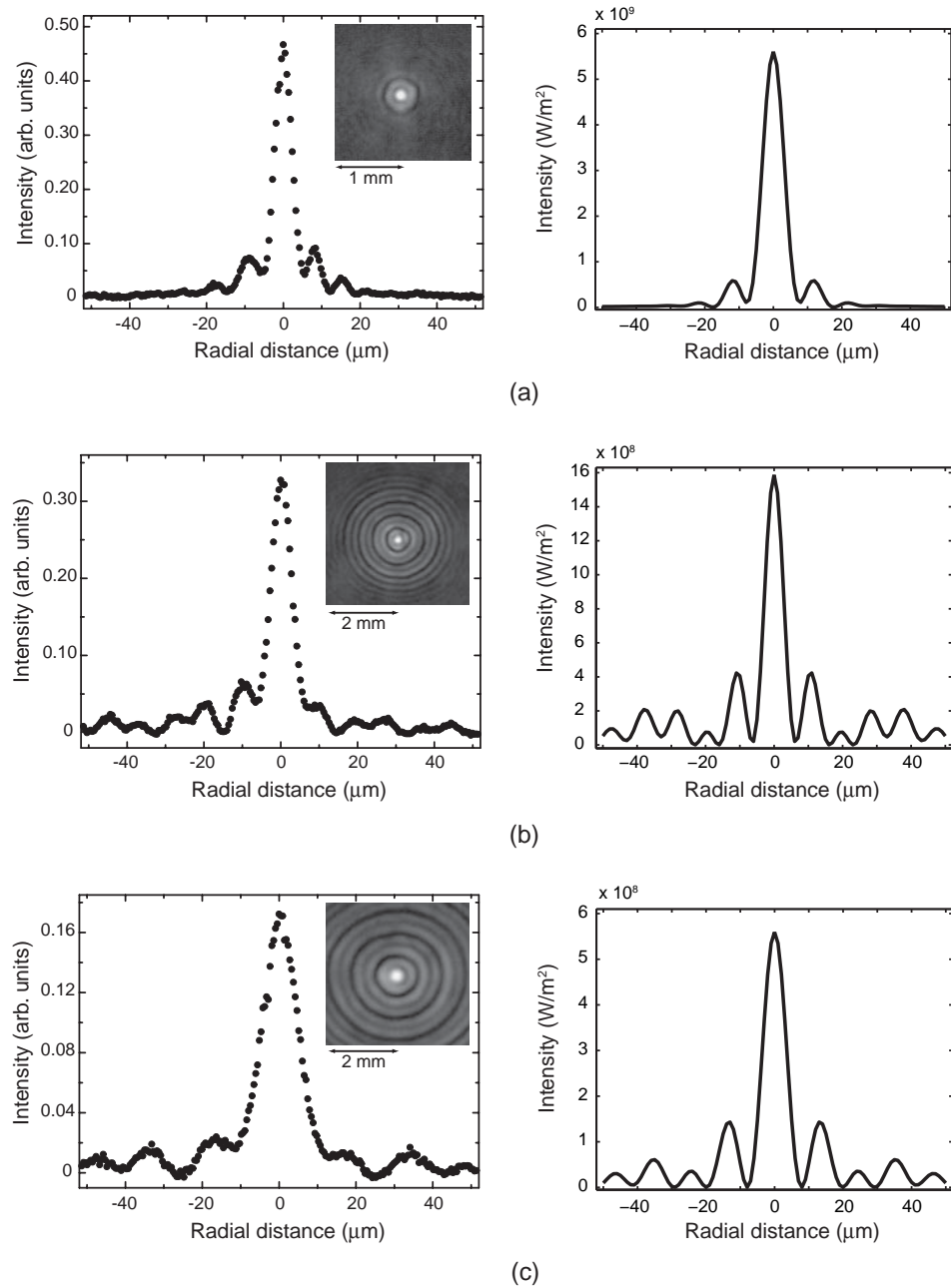


Figure 6.7: Measured intensity profiles together with the two-dimensional CCD images (left) and the corresponding theoretical profiles (right) of the self-focused laser beam at (a) 0 mm, (b) 1.5 mm, and (c) 4.5 mm from the waist.

Chapter 7

Conclusions

The first part of this thesis dealt with the preparation of thin films of ferromagnetic Ni–Mn–Ga shape-memory alloys using pulsed laser deposition. The goals were to demonstrate that PLD is an efficient and competitive technique to prepare Ni–Mn–Ga films and to find proper deposition parameters, in particular, the substrate temperature and the laser fluence such that the resulting films would be highly ferromagnetic and have the desired austenitic crystal structure at high temperatures and a smooth surface with a low droplet density. In addition, the samples should transform to the martensitic low-temperature phase when cooled below their critical temperature. These are necessary and — according to the studies made with bulk FSM alloys — usually sufficient conditions for the occurrence of the ferromagnetic shape-memory effect: the large deformations of a piece of material in an external magnetic field.

Pulsed laser deposition and other applications of laser ablation would greatly benefit from a laser beam which has a flat and uniform intensity distribution with steep edges across the laser-spot area on the ablation target. Standard Gaussian laser beams do not fulfill these requirements and, besides, the smaller is the waist radius of a Gaussian beam, the larger is its divergence. In the latter part of this work, diffractive optics was applied to convert the output of the excimer laser used in the deposition experiments into a flat-top-type profile in the desired plane. Diffractive optics provided a powerful way to tackle another beam-shaping problem: the generation of laser beams which diverge hardly at all upon propagation and whose focal line is long and possibly narrow. Such beams were created directly in a laser resonator equipped with a diffractive end mirror. In addition, another approach for the creation of approximately diffraction-free beams was studied. This technique was based on the self-focusing of a Gaussian beam in a highly nonlinear liquid crystal. The propagation-invariant beams studied in this thesis could be applied, e.g., in manipulating the motion of small particles and neutral atoms, aligning optical

systems, and in precise laser machining including laser ablation. The Q -switched Bessel–Gauss pulses discussed in section 6.3 could find use in PLD, too, after they have been amplified and imaged into the target plane.

The most important results of the thin-film research were that smooth, ferromagnetic films with a thickness of up to 300 nm could be deposited on single-crystalline silicon and NaCl substrates when the substrate temperature was 500 – 550 °C during the deposition and the laser fluence was 2.5 – 3 J/cm². With these parameters, the saturation magnetization of the films was almost 70 % of the typical value measured for bulk Ni–Mn–Ga samples, and the droplet density on the film surface was low ($< 0.01 \mu\text{m}^{-2}$). These are sufficiently good values such that the films could be used in the realization of microscopic FSM components — provided that they undergo the martensitic phase transformation at sufficiently low temperatures. In this respect, the prepared films were not perfect, yet: although the majority of the analyzed samples had crystallized in the proper austenitic phase, the X-ray diffraction data indicated the presence of other cubic phases between the substrate and austenitic Ni–Mn–Ga, and most of the studied films, in particular those deposited on silicon, seemed to remain in the parent phase even at liquid-helium temperatures. Obvious explanations are that the lattice constants of silicon and Ni–Mn–Ga differ too much from each other and that silicon eagerly forms silicide compounds at temperatures around or above 500 – 600 °C. Furthermore, silicon prevents free movements of the film and, simultaneously, stops any ongoing phase-transformation process. However, the large magnetizations and smooth surface of the films prove that the deposition parameters are close to their optimal values.

NaCl was observed to be a good choice for the substrate material: compared to silicon, the lattice match between NaCl and austenitic Ni–Mn–Ga is better, no chemical reactions seem to take place in the film–substrate interface, the saturation magnetization of the deposited films is of the same order of magnitude as that of samples on silicon, and, above all, the substrate can be removed partially or totally from the film with a few drops of water. This made it possible to study the properties of the sole films without the restricting effects of the substrate. During this work, several approaches were developed and studied to realize mm²- or even μm^2 -sized free-standing film structures such as cantilevers, air bridges, and areas under which the substrate had been "drilled" away. The best technique to fabricate small structures was noticed to be the combination of UV lithography and isotropic etching, e.g., with water. First, the film material was selectively removed from small areas with flat-top-shaped excimer-laser pulses, and then the substrate was etched away from under the region between two ablation spots.

Approximately 100- μm -wide and 1-mm-long air-bridge structures were successfully realized but due to their large mass and the tendency of water to spread between the film and the substrate, most of them collapsed or cracked into two pieces.

Smaller feature sizes were obtained by placing the diffractive elements at such a working distance that the different diffraction orders were separated in the output plane. When the fluence of all the orders exceeded the threshold value for ablation, 50 – 70- μm wide film-free areas separated by some 20- μm wide Ni–Mn–Ga stripes could be created on the surface of samples deposited both on silicon and on NaCl. Silicon proved to be a better candidate for the fabrication of μm -sized structures. Due to the good adhesion of Ni–Mn–Ga to silicon, the quality of the ablation spots was high, and although the substrate cannot be dissolved away as easily as in the case of NaCl, standard lithographic techniques nevertheless enable straightforward realization of tiny FSM components.

By measuring the magnetization at a fixed 0.3 – 0.5-T field as a function of temperature for several partially released films deposited on NaCl, signs of martensitic transformation at around $-100\text{ }^\circ\text{C}$ were observed. This gives a good reason to expect similar effects in all Ni–Mn–Ga films once the film and the substrate have been separated from each other. In addition, the Ni–Mn–Ga films deposited on Ni–Mn–Ga single crystals exhibited the same strain as the bulk, which proved that by using an optimal substrate material, highly crystalline Ni–Mn–Ga films that transform to the martensitic state upon cooling can be prepared by PLD.

Despite the many advantages of NaCl, it is not the ultimate solution: due to a large difference in thermal expansion coefficients of NaCl and Ni–Mn–Ga, the resulting film surface tends to be uneven and wrinkled. Standard semiconductors including silicon, germanium, and GaAs thus remain potential substrate materials since their lithographic patterning has been studied for decades, they can be insulated from the growing film by a lattice-matched and chemically inert buffer layer, and the crystal quality of the films could be improved by annealing the samples — particularly the released ones — at high temperatures; the heat treatment is known to improve the material properties of FSM alloys.

In the field of laser-beam shaping, diffractive optics proved to be an effective way to realize flat-top-type intensity distributions. Excimer-laser pulses were converted to $1.4 \times 4.4\text{-mm}^2$ flat-top profiles in the focal plane of a positive lens by inserting diffractive gratings at a certain working distance from the focus. Separate elements for the two transverse directions provided flexibility in the aspect ratio of the flat-top. The resulting profile of nine partially overlapping diffraction orders was rather smooth and homogeneous over the whole 4-mm^2 area, and measurements made using different working distances matched well with theoretical predictions. Only the fabrication errors of the element limited the profile uniformity. This is not an easy problem to solve: the average depth of the diffraction grating should not deviate more than 2 % (10 nm) from the goal value and the element groove profile should match the designed one to a high degree. However, the quality of the generated flat-top beams is already sufficient for patterning Ni–Mn–Ga films and for PLD.

The particular size of the flat-top, 4 mm^2 , was selected on the basis of earlier studies on the effect of the laser fluence and spot size on the quality of the deposited film: a proper range was observed to be $3 - 5 \text{ mm}^2$. Although with the present elements the optimal working distance is 10 cm, which means that the elements would be located inside the ablation chamber, this does not cause insuperable problems: the flat-top can be created outside the chamber and then imaged onto the target surface with a suitable lens.

Another important application area of laser-beam shaping was the creation of approximately diffraction-free, or more precisely, propagation-invariant beams, generally referred to as Bessel beams. Together with the flat-top profiles, Bessel beams provide advantages in laser ablation, and in this work, two novel ways to generate such beams were experimentally demonstrated: direct generation of Bessel–Gauss beams and Q -switched Bessel–Gauss pulses in laser resonators and creation of Bessel-like beams as a result of self-focusing of a Gaussian laser beam in a highly nonlinear nematic liquid crystal. The Bessel–Gauss beams had the correct intensity distribution within the whole propagation-invariant range in accordance with the theoretical predictions calculated from the Fresnel propagation formula. In the far field, the profile transformed to a ring, which gave additional proof that the beam was the exact fundamental Bessel–Gauss mode. Also the intensity profiles of the generated Q -switched pulses showed no observable differences from the expected behavior inside the 8-cm diffraction-free range. Only in the far field there were some deviations: the shorter the pulse (from 30 ns down to 3 ns), the more prominent was the additional peak in the middle of the ring. Nevertheless, the obtained results were the first demonstrations of Bessel–Gauss pulses. The Bessel-like beams created behind a liquid crystal showed that it is possible to generate narrow (diameter of the central bright spot smaller than $10 \mu\text{m}$) and long (5 – 10 mm) approximately propagation-invariant laser beams. These beams open up a whole new area of applications ranging from accurate optical tweezers to high-resolution laser machining.

As a conclusion, all the research areas discussed in this thesis and all the performed experiments had one common goal: to develop methods and techniques such that new materials could be efficiently produced in thin-film form. Simultaneously, novel types of laser beams with potential applications in several fields of physics, chemistry, biology, and engineering were generated. The results presented in this work fulfill this aim well and form a good basis for further studies such as the optimization of the physical properties of Ni–Mn–Ga films, decreasing the optical losses of the laser-ablation system with the help of diffractive optical elements, studying how the saturation magnetization and the martensitic transformation temperature depend on, e.g., the iron content of the alloy, and finally enable realizing small FSM devices.

Bibliography

- [1] O. Svelto, *Principles of Lasers* (Plenum Press, New York, 1998).
- [2] M. von Allmen and A. Blatter, *Laser-Beam Interactions with Materials* (Springer, Berlin, 1995).
- [3] C. N. Danson *et al.*, "Vulcan Petawatt — an ultra-high-intensity interaction facility," *Nucl. Fusion* **44**, S239–S246 (2004).
- [4] J. C. Miller (editor), *Laser Ablation – Principles and Applications* (Springer, Berlin, 1994).
- [5] C. B. Schaffer, *Interaction of Femtosecond Laser Pulses with Transparent Materials*, Ph.D. Thesis (Harvard University, 2001), Chapter 7.
- [6] C. B. Schaffer, A. Brodeur, J. F. García, and E. Mazur, "Micromachining bulk glass by use of femtosecond laser pulses with nanojoule energy," *Opt. Lett.* **26**, 93–95 (2001).
- [7] M. F. Yanik, H. Cinar, H. N. Cinar, A. Chisholm, Y. Jin, and A. Ben-Yakar, "Functional regeneration after laser axotomy," *Nature* **432**, 822 (2004).
- [8] A. Chimmalgi, C. P. Grigoropoulos, and K. Komvopoulos, "Surface nanostructuring by nano-/femtosecond laser-assisted scanning force microscopy," *J. Appl. Phys.* **97**, 104319-1–12 (2005).
- [9] F. Korte, J. Koch, J. Serbin, A. Ovsianikov, and B. N. Chichkov, "Three-dimensional nanostructuring with femtosecond laser pulses," *IEEE Trans. Nanotech.* **3**, 468–472 (2004).
- [10] J. Wang, H. Niino, and A. Yabe, "Micromachining of quartz crystal with excimer lasers by laser-induced backside wet etching," *Appl. Phys. A* **69**, S271–S273 (1999).

- [11] V. Tornari, V. Zafirooulos, A. Bonarou, N. A. Vainos, and C. Fotakis, "Modern technology in artwork conservation: a laser-based approach for process control and evaluation," *Optics and Lasers in Engineering* **34**, 309–326 (2000).
- [12] S. D. Allen, A. S. Miller, and S. J. Lee, "Laser assisted particle removal 'dry' cleaning of critical surfaces," *Mater. Sci. Eng. B* **49**, 85–88 (1997).
- [13] A. A. Puretzky, D. B. Geohegan, X. Fan, and S. J. Pennycook, "In situ imaging and spectroscopy of single-wall carbon nanotube synthesis by laser vaporization," *Appl. Phys. Lett.* **76**, 182–184 (2000).
- [14] D. B. Chrisey and G. K. Hubler (editors), *Pulsed Laser Deposition of Thin Films* (Wiley, New York, 1994).
- [15] P. R. Willmott and J. R. Huber, "Pulsed laser vaporization and deposition," *Rev. Mod. Phys.* **72**, 315–328 (2000).
- [16] M. N. R. Ashfold, F. Claeysens, G. M. Fuge, and S. J. Henley, "Pulsed laser ablation and deposition of thin films," *Chem. Soc. Rev.* **33**, 23–31 (2004).
- [17] A. Hakola, *Large-Area Deposition of High-Temperature Superconducting Thin Films Using Laser Ablation*, Master's Thesis (Helsinki University of Technology, 2001).
- [18] B. Dam, J. Rector, M. F. Chang, S. Kars, D. G. de Groot, and R. Griessen, "Laser ablation threshold of $\text{YBa}_2\text{Cu}_3\text{O}_{6+x}$," *Appl. Phys. Lett.* **65**, 1581–1583 (1994).
- [19] F. X. Wagner, M. Scaggs, A. Koch, H. Endert, H.-M. Christen, L. A. Knauss, K. S. Harshvardhan, and S. M. Green, "Epitaxial HTS thin films grown by PLD with a beam homogenizer," *Appl. Surf. Sci.* **127–129**, 477–480 (1998).
- [20] C. L. S. Lewis, I. Weaver, L. A. Doyle, G. W. Martin, T. Morrow, D. A. Pepler, C. N. Danson, and I. N. Ross, "Use of a random phase plate as a KrF laser beam homogenizer for thin film deposition applications," *Rev. Sci. Instrum.* **70**, 2116–2121 (1999).
- [21] J. Turunen, P. Pääkkönen, M. Kuittinen, P. Laakkonen, J. Simonen, T. Kajava, and M. Kaivola, "Diffractive shaping of excimer laser beams," *J. Mod. Opt.* **47**, 2467–2475 (2000).
- [22] J. Durnin, J. J. Miceli Jr., and J. H. Eberly, "Diffraction-free beams," *Phys. Rev. Lett.* **58**, 1499–1501 (1987).

- [23] J. Turunen, A. Vasara, and A. T. Friberg, "Holographic generation of diffraction-free beams," *Appl. Opt.* **27**, 3959–3962 (1988).
- [24] P. Pääkkönen, *Beam Formation And Shaping by Means of Diffractive Optics*, Doctoral Thesis (University of Joensuu, Joensuu, 2001).
- [25] P. Pääkkönen and J. Turunen, "Resonators with Bessel-Gauss modes," *Opt. Commun.* **156**, 359–366 (1998).
- [26] J. J. Wu, S.-H. Chen, J. Y. Fan, and G. S. Ong, "Propagation of a Gaussian-profile laser beam in nematic liquid crystals and the structure of its nonlinear diffraction rings," *J. Opt. Soc. Am. B* **7**, 1147–1157 (1990).
- [27] G. Bickel, G. Häusler, and M. Maul, "Triangulation with expanded range of depth," *Opt. Eng.* **24**, 975–977 (1985).
- [28] J. Arlt, V. Garces-Chavez, W. Sibbett, and K. Dholakia, "Optical micromanipulation using a Bessel light beam," *Opt. Commun.* **197**, 239–245 (2001).
- [29] M. Rioux, R. Tremblay, and P.-A. Belanger, "Linear, annular, and radial focusing with axicons and applications to laser machining," *Appl. Opt.* **17**, 1532–1536 (1978).
- [30] É. du Trémolet de Lacheisserie, D. Gignoux, and M. Schlenker (editors), *Magnetism, I — Fundamentals*, Grenoble Sciences (Kluwer, Norwell, 2002).
- [31] R. C. O'Handley, *Modern Magnetic Materials — Principles and Applications* (Wiley, New York, 2000).
- [32] N. W. Ashcroft and N. D. Mermin, *Solid State Physics* (Saunders College Publishing, Fort Worth, 1976).
- [33] K. Otsuka and C. M. Wayman, *Shape Memory Materials* (Cambridge University Press, Cambridge, 1998).
- [34] R. C. O'Handley, "Model for strain and magnetization in magnetic shape-memory alloys," *J. Appl. Phys.* **83**, 3263–3270 (1998).
- [35] W. J. Buehler, J. V. Gilfrich, and R. C. Wiley, "Effect of low-temperature phase changes on the mechanical properties of alloys near composition TiNi," *J. Appl. Phys.* **34**, 1475–1477 (1963).
- [36] K. Bhattacharya, *Microstructure of Martensite — why it forms and how it gives rise to the shape-memory effect* (Oxford University Press, Oxford, 2003).

- [37] P. Krulevitch, A. P. Lee, P. B. Ramsey, J. C. Trevino, J. Hamilton, and M. A. Northrup, "Thin film shape memory alloys microactuators," *J. Microelectromech. Syst.* **5**, 270–282 (1996).
- [38] K. Otsuka and X. Ren, "Recent developments in the research of shape memory alloys," *Intermetallics* **7**, 511–528 (1999).
- [39] K. Ullakko, J. K. Huang, C. Kantner, R. C. O'Handley, and V. V. Kokorin, "Large magnetic-field-induced strains in Ni₂MnGa single crystals," *Appl. Phys. Lett.* **69**, 1966–1968 (1996).
- [40] A. Sozinov, A. A. Likhachev, N. Lanska, and K. Ullakko, "Giant magnetic-field-induced strain in NiMnGa seven-layered martensitic phase," *Appl. Phys. Lett.* **80**, 1746–1748 (2002).
- [41] Y. Ge, O. Heczko, O. Söderberg, and V. K. Lindroos, "Various magnetic domain structures in a Ni–Mn–Ga martensite exhibiting magnetic shape memory effect," *J. Appl. Phys.* **96**, 2159–2163 (2004).
- [42] R. C. O'Handley, S. J. Murray, M. Marioni, H. Nembach, and S. M. Allen, "Phenomenology of giant magnetic-field-induced strain in ferromagnetic shape-memory materials," *J. Appl. Phys.* **87**, 4712–4717 (2000).
- [43] A. A. Likhachev and K. Ullakko, "Magnetic-field-controlled twin boundaries motion and giant magneto-mechanical effects in Ni–Mn–Ga shape memory alloy," *Phys. Lett. A* **275**, 142–151 (2000).
- [44] A. N. Vasil'ev, V. D. Buchel'nikov, T. Takagi, V. V. Khovailo, and É. I. Éstrin, "Shape memory ferromagnets," *Physics–Uspekhi* **46**, 559–588 (2003).
- [45] F. A. Hames, "Ferromagnetic-alloy phases near the compositions Ni₂MnIn, Ni₂MnGa, Co₂MnGa, Pd₂MnSb, and PdMnSb," *J. Appl. Phys.* **31**, S370–S371 (1960).
- [46] P. J. Webster, K. R. A. Ziebeck, S. L. Town, and M. S. Peak, "Magnetic order and phase transformation in Ni₂MnGa," *Phil. Mag. B* **49**, 295–310 (1984).
- [47] O. Söderberg, K. Koho, T. Sammi, X. W. Liu, A. Sozinov, N. Lanska, and V. K. Lindroos, "Effect of the selected alloying on Ni–Mn–Ga alloys," *Mater. Sci. Eng. A* **378**, 389–393 (2004).
- [48] O. Heczko and L. Straka, "Temperature dependence and temperature limits of magnetic shape memory effect," *J. Appl. Phys.* **94**, 7139–7143 (2003).

- [49] L. Straka and O. Heczko, "Magnetic anisotropy in Ni–Mn–Ga martensites," *J. Appl. Phys.* **93**, 8636–8638 (2003).
- [50] N. Lanska, O. Söderberg, A. Sozinov, Y. Ge, K. Ullakko, and V. K. Lindroos, "Composition and temperature dependence of the crystal structure of Ni–Mn–Ga alloys," *J. Appl. Phys.* **95**, 8074–8078 (2004).
- [51] L. Straka, O. Heczko, and K. Ullakko, "Investigation of magnetic anisotropy of Ni–Mn–Ga seven-layered orthorhombic martensite," *J. Magn. Magn. Mater.* **272–276**, 2049–2050 (2004).
- [52] V. A. Chernenko, E. Cesari, V. V. Kokorin, and I. N. Vitenko, "The development of new ferromagnetic shape memory alloys in Ni–Mn–Ga system," *Scr. Metall. Mater.* **33**, 1239–1244 (1995).
- [53] J. Enkovaara, A. Ayuela, A. T. Zayak, P. Entel, L. Nordström, M. Dube, J. Jalkanen, J. Impola, and R. M. Nieminen, "Magnetically driven shape memory alloys," *Mater. Sci. Eng. A* **378**, 52–60 (2004).
- [54] A. Sozinov, A. A. Likhachev, and K. Ullakko, "Crystal structure and magnetic anisotropy properties of Ni–Mn–Ga martensitic phases with giant magnetic-field-induced strain," *IEEE Trans. Magn.* **38**, 2814–2816 (2002).
- [55] S. J. Murray, M. Marioni, S. M. Allen, R. C. O'Handley, and T. A. Lograsso, "6% magnetic-field-induced strain by twin-boundary motion in ferromagnetic Ni–Mn–Ga," *Appl. Phys. Lett.* **77**, 886–888 (2000).
- [56] C. Jiang, T. Liang, H. Xu, M. Chang, and G. Wu, "Superhigh strains by variant reorientation in the nonmodulated ferromagnetic NiMnGa alloys," *Appl. Phys. Lett.* **81**, 2818–2820 (2002).
- [57] O. Heczko, "Magnetic shape memory effect and magnetization reversal," *J. Magn. Magn. Mater.* **290–291**, 787–794 (2005).
- [58] O. Heczko, A. Sozinov, and K. Ullakko, "Giant field-induced reversible strain in magnetic shape memory NiMnGa alloy," *IEEE Trans. Magn.* **36**, 3266–3268 (2000).
- [59] O. Heczko, L. Straka, N. Lanska, K. Ullakko, and J. Enkovaara, "Temperature dependence of magnetic anisotropy in Ni–Mn–Ga alloys exhibiting giant field-induced strain," *J. Appl. Phys.* **91**, 8228–8230 (2002).
- [60] J. Marcos, L. Manósa, A. Planes, F. Casanova, X. Batlle, and A. Labarta, "Multiscale origin of the magnetocaloric effect in Ni–Mn–Ga shape-memory alloys," *Phys. Rev. B* **68**, 094401-1–6 (2003).

- [61] D. Kikuchi, T. Kanomata, Y. Yamaguchi, H. Nishihara, K. Koyama, and K. Watanabe, "Magnetic properties of ferromagnetic shape memory alloys $\text{Ni}_2\text{Mn}_{1-x}\text{Fe}_x\text{Ga}$," *J. Alloys and Compounds* **383**, 184–188 (2004).
- [62] K. Tsuchiya, A. Tsutsumi, H. Ohtsuka, and M. Umemoto, "Modification of Ni–Mn–Ga ferromagnetic shape-memory alloy by addition of rare earth elements," *Mater. Sci. Eng. A* **378**, 370–376 (2004).
- [63] Z. H. Liu, M. Zhang, W. Q. Wang, W. H. Wang, J. L. Chen, G. H. Wu, F. B. Meng, H. Y. Liu, B. D. Liu, J. P. Qu, and Y. X. Li, "Magnetic properties and martensitic transformation in quaternary Heusler alloy of NiMnFeGa," *J. Appl. Phys.* **92**, 5006–5010 (2002).
- [64] A. A. Cherechukin, T. Takagi, H. Miki, M. Matsumoto, and M. Ohtsuka, "Influence of three-dimensional transition elements on magnetic and structural phase transitions of Ni–Mn–Ga alloys," *J. Appl. Phys.* **95**, 1740–1742 (2004).
- [65] A. A. Cherechukin, V. V. Khovailo, R. V. Kuposov, E. P. Krasnoperov, T. Takagi, and J. Tani, "Training of the Ni–Mn–Fe–Ga ferromagnetic shape-memory alloys due cycling in high magnetic field," *J. Magn. Magn. Mater.* **258–259**, 523–525 (2003).
- [66] K. Koho, O. Söderberg, N. Lanska, Y. Ge, X. Liu, L. Straka, J. Vimpari, O. Heczko, and V. K. Lindroos, "Effect of the chemical composition to martensitic transformation in Ni–Mn–Ga–Fe alloys," *Mater. Sci. Eng. A* **378**, 384–388 (2004).
- [67] G. H. Wu, W. H. Wang, J. L. Chen, L. Ao, Z. H. Liu, W. S. Zhan, T. Liang, and H. B. Xu, "Magnetic properties and shape memory of Fe-doped $\text{Ni}_{52}\text{Mn}_{24}\text{Ga}_{24}$ single crystals," *Appl. Phys. Lett.* **80**, 634–636 (2002).
- [68] I. Suorsa, *Performance and Modeling of Magnetic Shape Memory Actuators and Sensors*, Doctoral Dissertation (Helsinki University of Technology, 2005), Chapters 5 and 6.
- [69] I. Suorsa, J. Tellinen, E. Pagounis, I. Aaltio, and K. Ullakko, "Applications of magnetic shape memory actuators," *Proc. ACTUATOR 2002 Int. Conf.* (Bremen, Germany, 2002), p. 158.
- [70] J. Tellinen, I. Suorsa, A. Jääskeläinen, I. Aaltio, and K. Ullakko, "Basic properties of magnetic shape memory actuators," *Proc. ACTUATOR 2002 Int. Conf.* (Bremen, Germany, 2002), p. 527.

- [71] B. Winzek, S. Schmitz, H. Rumpf, T. Sterzl, R. Hassdorf, S. Thienhaus, J. Feydt, M. Moske, and E. Quandt, "Recent developments in shape memory thin film technology," *Mater. Sci. Eng. A* **378**, 40–46 (2004).
- [72] I. Suorsa, J. Tellinen, K. Ullakko, and E. Pagounis, "Voltage generation induced by mechanical straining in magnetic shape-memory materials," *J. Appl. Phys.* **95**, 8054–8058 (2004).
- [73] H. Ohno, "Making nonmagnetic semiconductors ferromagnetic," *Science* **281**, 951–955 (1998).
- [74] H. Ohno, F. Matsukura, and Y. Ohno, "Semiconductor spin electronics," *JSAP International* 5/2002, 4–13 (2002).
- [75] X. Y. Dong, C. Adelman, J. Q. Xie, C. J. Palmstrøm, X. Lou, J. Strand, P. A. Crowell, J.-P. Barnes, and A. K. Petford-Long, "Spin injection from the Heusler alloy Co_2MnGe into $\text{Al}_{0.1}\text{Ga}_{0.9}\text{As}/\text{GaAs}$ heterostructures," *Appl. Phys. Lett.* **86**, 102107-1–3 (2005).
- [76] J. W. Dong, J. Q. Xie, J. Lu, C. Adelman, C. J. Palmstrøm, J. Cui, Q. Pan, T. W. Shield, R. D. James, and S. McKernan, "Shape memory and ferromagnetic shape memory effects in single-crystal Ni_2MnGa thin films," *J. Appl. Phys.* **95**, 2593–2600 (2004).
- [77] J. W. Dong, L. C. Chen, C. J. Palmstrøm, R. D. James, and S. McKernan, "Molecular beam epitaxy growth of ferromagnetic single crystal (001) Ni_2MnGa on (001) GaAs," *Appl. Phys. Lett.* **75**, 1443–1445 (1999).
- [78] J. W. Dong, L. C. Chen, J. Q. Xie, T. A. R. Müller, D. M. Carr, C. J. Palmstrøm, S. McKernan, Q. Pan, and R. D. James, "Epitaxial growth of ferromagnetic Ni_2MnGa on GaAs(001) using NiGa interlayers," *J. Appl. Phys.* **88**, 7357–7359 (2000).
- [79] M. S. Lund, J. W. Dong, J. Lu, X. Y. Dong, C. J. Palmstrøm, and C. Leighton, "Anomalous magnetotransport properties of epitaxial full Heusler alloys," *Appl. Phys. Lett.* **80**, 4798–4800 (2002).
- [80] Q. Pan, J. W. Dong, C. J. Palmstrøm, J. Cui, and R. D. James, "Magnetic domain observations of freestanding single crystal patterned Ni_2MnGa films," *J. Appl. Phys.* **91**, 7812–7814 (2002).
- [81] J.-P. Ahn, N. Cheng, T. Lograsso, and K. M. Krishnan, "Magnetic properties of, structure and shape-memory transitions in Ni–Mn–Ga thin films grown by ion-beam sputtering," *IEEE Trans. Magn.* **37**, 2141–2143 (2001).

- [82] S. I. Patil, D. Tan, S. E. Lofland, S. M. Bhagat, I. Takeuchi, O. Famodu, J. C. Read, K.-S. Chang, C. Craciunescu, and M. Wuttig, "Ferromagnetic resonance in Ni–Mn–Ga films," *Appl. Phys. Lett.* **81**, 1279–1281 (2002).
- [83] M. Ohtsuka and K. Itagaki, "Effect of heat treatment on properties of Ni–Mn–Ga films prepared by a sputtering method," *Int. J. Appl. Electromagn. Mech.* **12**, 49–59 (2000).
- [84] M. Ohtsuka, M. Sanada, M. Matsumoto, and K. Itagaki, "Magnetic-field induced shape memory effect in Ni₂MnGa sputtered films," *Mater. Sci. Eng. A* **378**, 377–383 (2004).
- [85] I. Takeuchi, O. O. Famodu, J. C. Read, M. A. Aronova, K.-S. Chang, C. Craciunescu, S. E. Lofland, M. Wuttig, F. C. Wellstood, L. Knauss, and A. Orozco, "Identification of novel compositions of ferromagnetic shape-memory alloys using composition spreads," *Nature Materials* **2**, 180–184 (2003).
- [86] K. W. Kim, Y. V. Kudryavtsev, J. Y. Rhee, N. N. Lee, and Y. P. Lee, "A comparative study of Ni₂MnGa, Ni₂MnAl, and Ni₂MnIn Heusler alloy films," *IEEE Trans. Magn.* **40**, 2775–2777 (2004).
- [87] V. Podgurski and S. Galambos, "Ni₂MnGa thin films deposited by laser ablation," *Proc. DAAAM Int. Conf. (Tallinn, Estonia, 2000)*, p. 229.
- [88] P. G. Tello, F. J. Castaño, R. C. O'Handley, S. M. Allen, M. Esteve, F. Castaño, A. Labarta, and X. Batlle, "Ni–Mn–Ga thin films produced by pulsed laser deposition," *J. Appl. Phys.* **91**, 8234–8236 (2002).
- [89] F. J. Castaño, B. Nelson-Cheeseman, R. C. O'Handley, C. A. Ross, C. Redondo, and F. Castaño, "Structure and thermomagnetic properties of polycrystalline Ni–Mn–Ga thin films," *J. Appl. Phys.* **93**, 8492–8494 (2003).
- [90] C. Y. Chung, V. A. Chernenko, V. V. Khovailo, J. Pons, E. Cesari, and T. Takagi, "Thin films of ferromagnetic shape memory alloys processed by laser beam ablation," *Mater. Sci. Eng. A* **378**, 443–447 (2004).
- [91] V. A. Golub, A. Y. Vovk, L. Malkinski, C. J. O'Connor, Z. Wang, and J. Tang, "Anomalous magnetoresistance in NiMnGa thin films," *J. Appl. Phys.* **96**, 3865–3869 (2004).
- [92] T. J. Zhu, L. Lu, M. O. Lai, and J. Ding, "Growth and magnetic properties of NiMnGa thin films prepared by pulsed laser ablation," *Smart Mater. Struct.* **14**, S293–S296 (2005).

- [93] J. Shen, Z. Gai, and J. Kirschner, "Growth and magnetism of metallic thin films and multilayers by pulsed-laser deposition," *Surf. Sci. Rep.* **52**, 163–218 (2004).
- [94] D. von der Linde and K. Sokolowski-Tinten, "The physical mechanisms of short-pulse laser ablation," *Appl. Surf. Sci.* **154–155**, 1–10 (2000).
- [95] D. von der Linde, K. Sokolowski-Tinten, and J. Bialkowski, "Laser–solid interaction in the femtosecond regime," *Appl. Surf. Sci.* **109/110**, 1–10 (1997).
- [96] S. S. Mao, F. Quéré, S. Guizard, X. Mao, R. E. Russo, G. Petite, and P. Martin, "Dynamics of femtosecond laser interactions with dielectrics," *Appl. Phys. A* **79**, 1695–1709 (2004).
- [97] E. G. Gamaly, A. V. Rode, B. Luther-Davies, and V. T. Tikhonchuk, "Ablation of solids by femtosecond lasers: ablation mechanism and ablation thresholds for metals and dielectrics," *Phys. Plasmas* **9**, 949–957 (2002).
- [98] T. E. Itina, J. Hermann, Ph. Delaporte, and M. Sentis, "Modeling of metal ablation induced by ultrashort laser pulses," *Thin Solid Films* **453–454**, 513–517 (2004).
- [99] B. N. Chichkov, C. Momma, S. Nolte, F. von Alvensleben, and A. Tünnermann, "Femtosecond, picosecond and nanosecond laser ablation of solids," *Appl. Phys. A* **63**, 109–115 (1996).
- [100] J. N. Leboeuf, K. R. Chen, J. M. Donato, D. B. Geohegan, C. L. Liu, A. A. Puretzky, and R. F. Wood, "Modeling of dynamical processes in laser ablation," *Appl. Surf. Sci.* **96–98**, 14–23 (1996).
- [101] J. G. Lunney and R. Jordan, "Pulsed laser ablation of metals," *Appl. Surf. Sci.* **127–129**, 941–946 (1998).
- [102] R. F. Haglund Jr., "Microscopic and mesoscopic aspects of laser-induced desorption and ablation," *Appl. Surf. Sci.* **96–98**, 1–13 (1996).
- [103] R. Kelly and A. Miotello, "Mechanisms of pulsed laser sputtering" in *Pulsed Laser Deposition of Thin Films*, D. B. Chrisey and G. K. Hubler (editors), (Wiley, New York, 1994).
- [104] R. F. Haglund Jr. and N. Itoh, "Electronic processes in laser ablation of semiconductors and insulators" in *Laser Ablation – Principles and Applications*, J. C. Miller (editor), (Springer, Berlin, 1994).

- [105] S. R. Foltyn, "Surface modification of materials by cumulative laser irradiation" in *Pulsed Laser Deposition of Thin Films*, D. B. Chrisey and G. K. Hubler (editors), (Wiley, New York, 1994).
- [106] S. Martin, A. Hertwig, M. Lenzner, J. Krüger, and W. Kautek, "Spot-size dependence of the ablation threshold in dielectrics for femtosecond laser pulses," *Appl. Phys. A* **77**, 883–884 (2003).
- [107] L. M. Doeswijk, G. Rijnders, and D. H. A. Blank, "Pulsed laser deposition: metal versus oxide ablation," *Appl. Phys. A* **78**, 263–268 (2004).
- [108] K. L. Saenger, "Angular distribution of ablated material" in *Pulsed Laser Deposition of Thin Films*, D. B. Chrisey and G. K. Hubler (editors), (Wiley, New York, 1994).
- [109] S. Amoruso, B. Toftmann, and J. Schou, "Expansion of a laser-produced silver plume in light background gases," *Appl. Phys. A* **79**, 1311–1314 (2004).
- [110] T. E. Itina, J. Hermann, Ph. Delaporte, and M. Sentis, "Combined continuous-microscopic modeling of laser plume expansion," *Appl. Surf. Sci.* **208–209**, 27–32 (2003).
- [111] S. S. Mao, X. Mao, R. Greif, and R. E. Russo, "Initiation of early-stage plasma during picosecond laser ablation of solids," *Appl. Phys. Lett.* **77**, 2464–2466 (2000).
- [112] K. R. Chen, T. C. King, J. H. Hes, J. N. Leboeuf, D. B. Geohegan, R. F. Wood, A. A. Puretzky, and J. M. Donato, "Theory and numerical modeling of the accelerated expansion of laser-ablated materials near a solid surface," *Phys. Rev. B* **60**, 8373–8382 (1999).
- [113] D. B. Geohegan, "Diagnostics and characteristics of pulsed laser deposition laser plasmas" in *Pulsed Laser Deposition of Thin Films*, D. B. Chrisey and G. K. Hubler (editors), (Wiley, New York, 1994).
- [114] B. Toftmann, J. Schou, T. N. Hansen, and J. G. Lunney, "Evolution of the plasma parameters in the expanding laser ablation plume of silver," *Appl. Surf. Sci.* **186**, 293–297 (2002).
- [115] B. Toftmann, J. Schou, T. N. Hansen, and J. G. Lunney, "Angular distribution of electron temperature density in a laser-ablation plume," *Phys. Rev. Lett.* **84**, 3998–4001 (2000).

- [116] S. Amoruso, B. Toftmann, and J. Schou, "Thermalization of a UV laser ablation plume in a background gas: from a directed to a diffusionlike flow," *Phys. Rev. E* **69**, 056403-1–6 (2004).
- [117] J. S. Horwitz and J. A. Sprague, "Film nucleation and film growth in pulsed laser deposition of ceramics" in *Pulsed Laser Deposition of Thin Films*, D. B. Chrisey and G. K. Hubler (editors), (Wiley, New York, 1994).
- [118] J. H. Song and Y. H. Jeong, "SrTiO₃ homoepitaxy by the pulsed laser deposition method: island, layer-by-layer, and step-flow growth," *Solid State Commun.* **125**, 563–566 (2003).
- [119] W.-F. Hu, X.-J. Zhao, W. Peng, T.-S. Wang, W. Liu, L. Li, C. Lei, Y.-F. Chen, and L. Li, "Control of the growth mode of epitaxial *c*-axis YBa₂Cu₃O_{7- δ} thin films by vicinal (0 0 1) SrTiO₃ substrates," *J. Crystal Growth* **231**, 493–497 (2001).
- [120] D. H. A. Blank, G. J. H. M. Rijnders, G. Koster, and H. Rogalla, "A new approach in layer-by-layer growth of oxide materials by pulsed laser deposition," *J. Electroceramics* **4**, 311–318 (2000).
- [121] D. H. A. Blank, G. Koster, G. A. J. H. M. Rijnders, E. van Setten, P. Slycke, and H. Rogalla, "Epitaxial growth of oxides with pulsed laser interval deposition," *J. Crystal Growth* **211**, 98–105 (2000).
- [122] B. Dam, J. H. Rector, J. M. Huijbregtse, and R. Griessen, "The transition from 2D-nucleation to spiral growth in pulsed laser deposited YBa₂Cu₃O_{7- δ} films," *Physica C* **305**, 1–10 (1998).
- [123] J. Choi, C. B. Eom, G. Rijnders, H. Rogalla, and D. H. A. Blank, "Growth mode transition from layer by layer to step flow during the growth of heteroepitaxial SrRuO₃ on (0 0 1) SrTiO₃," *Appl. Phys. Lett.* **79**, 1447–1449 (2001).
- [124] G. Koster, K. Verbist, G. Rijnders, H. Rogalla, G. van Tendeloo, and D. H. A. Blank, "Structure and properties of (Sr,Ca)CuO₂-BaCuO₂ superlattices grown by pulsed laser interval deposition," *Physica C* **353**, 167–183 (2001).
- [125] D. Q. Shi, M. Ionescu, T. M. Silver, and S. X. Dou, "Relationship between epitaxial deposition and growth modes of CeO₂ films," *Physica C* **384**, 475–481 (2003).

- [126] L. Chen, "Particulates generated by pulsed laser ablation" in *Pulsed Laser Deposition of Thin Films*, D. B. Chrisey and G. K. Hubler (editors), (Wiley, New York, 1994).
- [127] J. D. Suh, G. Y. Sung, K. Y. Kang, H. S. Kim, J. Y. Lee, D. K. Kim, and C. H. Kim, "Cubic Y–Ba–Cu–O thin films by high speed pulsed laser deposition," *Physica C* **308**, 251–256 (1998).
- [128] S. Kahl and A. M. Grishin, "Pulsed laser deposition of $Y_3Fe_5O_{12}$ and $Bi_3Fe_5O_{12}$ films on garnet substrates," *J. Appl. Phys.* **93**, 6945–6947 (2003).
- [129] A. Klini, A. Manousaki, D. Anglos, and C. Fotakis, "Growth of ZnO films by ultraviolet pulsed-laser ablation: study of plume dynamics," *J. Appl. Phys.* **98**, 123301-1–8 (2005).
- [130] F. M. Dickey, "Laser beam shaping," *Optics and Photonics News*, April 2003, 30–35 (2003).
- [131] F. Nikolajeff, S. Hård, and B. Curtis, "Diffractive microlenses replicated in fused silica for excimer laser-beam homogenizing," *Appl. Opt.* **36**, 8481–8489 (1997).
- [132] P. E. Dyer and C. D. Walton, "VUV laser ablation of insulators," *Appl. Phys. A* **79**, 721–727 (2004).
- [133] J. A. Greer, "Commercial scale-up of pulsed laser deposition" in *Pulsed Laser Deposition of Thin Films*, D. B. Chrisey and G. K. Hubler (editors), (Wiley, New York, 1994).
- [134] A. Hakola, *Large-Area Deposition of High-Temperature Superconducting Thin Films Using Laser Ablation*, Master's Thesis (Helsinki University of Technology, 2001), Chapter 3.5.
- [135] R. H. Lehmberg and S. P. Obenschain, "Use of induced spatial incoherence for uniform illumination of laser fusion targets," *Opt. Commun.* **46**, 27–31 (1983).
- [136] Y. Kato, K. Mima, N. Miyanaga, S. Arinaga, Y. Kitagawa, M. Nakatsuka, and C. Yamanaka, "Random phasing of high-power lasers for uniform target acceleration and plasma-instability suppression," *Phys. Rev. Lett.* **53**, 1057–1060 (1984).
- [137] J. Turunen and F. Wyrowski (editors), *Diffractive Optics for Industrial and Commercial Applications* (Wiley, Berlin, 1997).

- [138] K. Jasper, S. Scheede, B. Burghardt, R. Senczuk, P. Berger, H.-J. Kahlert, and H. Hügel, "Excimer laser beam homogenizer with low divergence," *Appl. Phys. A* **69**, S315–S318 (1999).
- [139] C. Kopp, L. Ravel, and P. Meyrueis, "Efficient beamshaper homogenizer design combining diffractive optical elements, microlens array and random phase plate," *J. Opt. A: Pure Appl. Opt.* **1**, 398–403 (1999).
- [140] Q. Lin and L. Wang, "Optical resonators producing partially coherent flat-top beams," *Opt. Commun.* **175**, 295–300 (2000).
- [141] D. Schäfer, "Design concept for diffractive elements shaping partially coherent laser beams," *J. Opt. Soc. Am. A* **18**, 2915–2922 (2001).
- [142] S. Zhang, G. Neil, and M. Shinn, "Single-element laser beam shaper for uniform flat-top profiles," *Opt. Express* **11**, 1942–1948 (2003).
- [143] Y. Matsuura, D. Akiyama, and M. Miyagi, "Beam homogenizer for hollow-fiber delivery system of excimer laser light," *Appl. Opt.* **42**, 3505–3508 (2003).
- [144] S. Bollanti, P. di Lazzaro, D. Murra, E. Tefouet Kana, and G. Felici, "Edge steepness and plateau uniformity of a nearly flat-top-shaped laser beam," *Appl. Phys. B* **78**, 195–198 (2004).
- [145] M. Tuohiniemi, *Laser Ablation System for Depositing High-Temperature Superconducting $YBa_2Cu_3O_{7-\delta}$ Thin Films*, Master's Thesis (Helsinki University of Technology, 1999).
- [146] I. Jantunen, *Measuring the Intensity Distribution of a High-Power Laser Pulse with Polymer Film Ablation*, Special Assignment (Helsinki University of Technology, 1999).
- [147] V. Kekkonen, *Magnetization Measurements of Thin Films at Different Temperatures*, Special Assignment (in Finnish) (Helsinki University of Technology, 2005).
- [148] F. Gori, G. Guattari, and C. Padovani, "Bessel–Gauss beams," *Opt. Commun.* **64**, 491–495 (1987).
- [149] K. Uehara and H. Kikuchi, "Generation of nearly diffraction-free laser beams," *Appl. Phys. B* **48**, 125–129 (1989).
- [150] A. N. Khilo, E. G. Katranji, and A. A. Ryzhevich, "Axicon-based Bessel resonator: analytical description and environment," *J. Opt. Soc. Am. A* **18**, 1986–1992 (2001).

- [151] Z. Jaroszewicz, A. Burvall, and A. T. Friberg, "Axicon — the most important optical element," *Optics and Photonics News*, April 2005, 34–39 (2005).
- [152] G. Häusler and W. Hesel, "Light sectioning with large depth and high resolution," *Appl. Opt.* **27**, 5165–5169 (1988).
- [153] J. Arlt and K. Dholakia, "Generation of high-order Bessel beams by use of an axicon," *Opt. Commun.* **177**, 297–301 (2000).
- [154] J. Arlt, T. Hitomi, and K. Dholakia, "Atom guiding along Laguerre–Gaussian and Bessel light beams," *Appl. Phys. B* **71**, 549–554 (2000).
- [155] M. Lei and B. Yao, "Characteristics of beam profile of Gaussian beam passing through an axicon," *Opt. Commun.* **239**, 367–372 (2004).
- [156] Z. Jaroszewicz, V. Climent, V. Duran, J. Lancis, A. Kolodziejczyk, A. Burvall, and A. T. Friberg, "Programmable axicon for variable inclination of the focal segment," *J. Mod. Opt.* **51**, 2185–2190 (2004).
- [157] J. Lu, T. K. Song, R. R. Kinnick, and J. F. Greenleaf, "*In vitro* and *in vivo* real-time imaging with ultrasonic limited diffraction beams," *IEEE Trans. Med. Imaging* **12**, 819–829 (1993).
- [158] M. Saffman, "Addressing atoms in optical lattices with Bessel beams," *Opt. Lett.* **29**, 1016–1018 (2004).
- [159] R. B. Charters, B. Luther-Davies, and F. Ladouceur, "Improved performance of laser written channel waveguides using a TEM₀₁* beam," *IEEE Photon. Technol. Lett.* **11**, 1617–1619 (1999).
- [160] Q. Ren and R. Birngruber, "Axicon: a new laser beam delivery system for corneal surgery," *IEEE J. Quant. Electr.* **26**, 2305–2308 (1990).
- [161] R. Tremblay, Y. D'Astous, G. Roy, and M. Blanchard, "Laser plasmas optically pumped by focusing with an axicon a CO₂-TEA laser beam in a high-pressure gas," *Opt. Commun.* **28**, 193–196 (1979).
- [162] M. O'Scullly and M. S. Zubairy, "Simple laser accelerator: optics and particle dynamics," *Phys. Rev. A* **44**, 2656–2663 (1991).
- [163] Y. Li, H. Lee, and E. Wolf, "New generalized Bessel–Gaussian beams," *J. Opt. Soc. Am. A* **21**, 640–646 (2004).
- [164] R. Simon and N. Mukunda, "Twisted Gaussian Schell-model beams," *J. Opt. Soc. Am. A* **10**, 95–109 (1993).

- [165] A. T. Friberg, E. Tervonen, and J. Turunen, "Interpretation and experimental demonstration of twisted Gaussian Schell-model beams," *J. Opt. Soc. Am. A* **11**, 1818–1826 (1994).
- [166] J. W. Goodman, *Introduction to Fourier Optics* (McGraw–Hill, New York, 1996).
- [167] L. Mandel and E. Wolf, *Optical Coherence and Quantum Optics* (Cambridge University Press, New York, 1995), Chapter 5.
- [168] J. T. Foley and M. S. Zubairy, "The directionality of Gaussian Schell-model beams," *Opt. Commun.* **26**, 297–300 (1978).
- [169] A. T. Friberg and R. J. Sudol, "Propagation parameters of Gaussian Schell-model beams," *Opt. Commun.* **41**, 383–387 (1982).
- [170] E. Collett and E. Wolf, "Is complete spatial coherence necessary for the generation of highly directional light beams?," *Opt. Lett.* **2**, 27–29 (1978).
- [171] P. de Santis, F. Gori, G. Guattari, and C. Palma, "An example of a Collett–Wolf source," *Opt. Commun.* **29**, 256–260 (1979).
- [172] F. Gori, "Collett–Wolf sources and multimode lasers," *Opt. Commun.* **34**, 301–305 (1980).
- [173] H. P. Herzig, D. Prongué, and R. Dändliker, "Design and fabrication of highly efficient fan-out elements," *Jpn. J. Appl. Phys.* **29**, L1307–L1309 (1990).
- [174] P. Laakkonen, J. Lautanen, V. Kettunen, J. Turunen, and M. Schirmer, "Multilevel diffractive elements in SiO₂ by electron beam lithography and proportional etching with analogue negative resist," *J. Mod. Opt.* **46**, 1295–1307 (1999).
- [175] J. Durnin, "Exact solutions for nondiffracting beams. I. The scalar theory," *J. Opt. Soc. Am. A* **4**, 651–654 (1987).
- [176] J. Durnin, J. J. Miceli, Jr., and J. H. Eberly, "Comparison of Bessel and Gaussian beams," *Opt. Lett.* **13**, 79–80 (1988).
- [177] W. D. Montgomery, "Self-imaging objects of infinite aperture," *J. Opt. Soc. Am.* **57**, 772–778 (1967).
- [178] V. Bagini, F. Frezza, M. Santarsiero, G. Schettini, and G. S. Spagnolo, "Generalized Bessel–Gauss beams," *J. Mod. Opt.* **43**, 1155–1166 (1996).

- [179] A. J. Cox and J. D'Anna, "Constant-axial-intensity nondiffracting beam," *Opt. Lett.* **17**, 232–234 (1992).
- [180] Z. Jiang, Q. Lu, and Z. Liu, "Propagation of apertured Bessel beams," *Appl. Opt.* **34**, 7183–7185 (1995).
- [181] R. Borghi, M. Santarsiero, and F. Gori, "Axial intensity of apertured Bessel beams," *J. Opt. Soc. Am. A* **14**, 23–26 (1997).
- [182] C. J. R. Sheppard and A. Choudhury, "Annular pupils, radial polarization, and superresolution," *Appl. Opt.* **43**, 4322–4327 (2004).
- [183] G. Martínez-Niconoff, J. C. Ramírez-San-Juan, P. Martínez-Vara, A. Cabarjal-Domínguez, and A. S. Ostrovsky, "Generation of partially coherent diffraction-free fields with tunable geometry," *J. Opt. Soc. Am. A* **21**, 546–551 (2004).
- [184] M. Santarsiero, "Propagation of generalized Bessel–Gauss beams through ABCD optical systems," *Opt. Commun.* **132**, 1–7 (1996).
- [185] C. Palma, R. Borghi, and G. Cincotti, "Beams originated by J_0 -correlated Schell-model planar sources," *Opt. Commun.* **125**, 113–121 (1996).
- [186] J. H. McLeod, "The axicon: a new type of optical element," *J. Opt. Soc. Am.* **44**, 592–597 (1954).
- [187] J. H. McLeod, "Axicons and their uses," *J. Opt. Soc. Am.* **50**, 166–169 (1960).
- [188] A. Vasara, J. Turunen, and A. T. Friberg, "Realization of general nondiffracting beams with computer-generated holograms," *J. Opt. Soc. Am. A* **6**, 1748–1754 (1989).
- [189] S. Yu Popov and A. T. Friberg, "Apodization of generalized axicons to produce uniform axial line images," *Pure Appl. Opt.* **7**, 537–548 (1998).
- [190] S. Yu Popov, A. T. Friberg, M. Honkanen, J. Lautanen, J. Turunen, and B. Schnabel, "Apodized annular-aperture diffractive axicons fabricated by continuous-path-control electron beam lithography," *Opt. Commun.* **154**, 359–367 (1998).
- [191] I. Kallioniemi, J. Saarinen, K. Blomstedt, and J. Turunen, "Polygon approximation of the fringes of diffractive elements," *Appl. Opt.* **36**, 7217–7223 (1997).


- [192] M. Honkanen and J. Turunen, "Tandem systems for efficient generation of uniform-axial-intensity Bessel fields," *Opt. Commun.* **154**, 368–375 (1998).
- [193] A. G. Sedukhin, "Beam-preshaping axicon focusing," *J. Opt. Soc. Am. A* **15**, 3057–3066 (1998).
- [194] J. Lautanen, V. Kettunen, P. Laakkonen, and J. Turunen, "High-efficiency production of propagation-invariant spot arrays," *J. Opt. Soc. Am. A* **17**, 2208–2215 (2000).
- [195] G. Indebetouw, "Nondiffracting optical fields: some remarks on their analysis and synthesis," *J. Opt. Soc. Am. A* **6**, 150–152 (1989).
- [196] J. K. Jabczyński, "A 'diffraction-free' resonator," *Opt. Commun.* **77**, 292–294 (1990).
- [197] P. Muys and E. Vandamme, "Direct generation of Bessel beams," *Appl. Opt.* **41**, 6375–6379 (2002).
- [198] J. Rogel-Salazar, G. H. C. New, and S. Chávez-Cerda, "Bessel–Gauss beam optical resonator," *Opt. Commun.* **190**, 117–122 (2001).
- [199] J. C. Gutiérrez-Vega, R. Rodríguez-Masegosa, and S. Chávez-Cerda, "Bessel–Gauss resonator with spherical output mirror: geometrical- and wave-optics analysis," *J. Opt. Soc. Am. A* **20**, 2113–2122 (2003).
- [200] N. Chattapiban, E. A. Rogers, D. Cofield, W. T. Hill, III, and R. Roy, "Generation of nondiffracting Bessel beams by use of a spatial light modulator," *Opt. Lett.* **28**, 2183–2185 (2003).
- [201] C. L. Tsangaris, G. H. C. New, and J. Rogel-Salazar, "Unstable Bessel beam resonator," *Opt. Commun.* **223**, 233–238 (2003).
- [202] P. A. Bélanger and C. Paré, "Optical resonators using graded-phase mirrors," *Opt. Lett.* **16**, 1057–1059 (1991).
- [203] J. R. Leger, D. Chen, and Z. Wang, "Diffractive optical element for mode shaping of a Nd:YAG laser," *Opt. Lett.* **19**, 108–110 (1994).
- [204] Z. H. Yang, J. R. Leger, and A. V. Shchegrov, "Three-mirror resonator with aspheric feedback mirror for laser spatial mode selection and mode shaping," *IEEE J. Quant. Electr.* **40**, 1258–1269 (2004).
- [205] A. Shevchenko, S. C. Buchter, N. V. Tabiryán, and M. Kaivola, "Creation of a hollow laser beam using self-phase modulation in a nematic liquid crystal," *Opt. Commun.* **232**, 77–82 (2004).

- [206] A. Shevchenko, S. C. Buchter, N. V. Tabiryan, and M. Kaivola, "Self-focusing in a nematic liquid crystal for measurements of wavefront distortions," *Opt. Commun.* **232**, 439–442 (2004).
- [207] J. J. Zayhowski, "Passively Q -switched Nd:YAG microchip lasers and applications," *J. Alloys and Compounds* **303–304**, 393–400 (2000).
- [208] B. Braun, F. X. Kärtner, G. Zhang, M. Moser, and U. Keller, "56-ps passively Q -switched diode-pumped microchip laser," *Opt. Lett.* **22**, 381–383 (1997).
- [209] G. J. Spühler, R. Paschotta, R. Fluck, B. Braun, M. Moser, G. Zhang, E. Gini, and U. Keller, "Experimentally confirmed design guidelines for passively Q -switched microchip lasers using semiconductor saturable absorbers," *J. Opt. Soc. Am. B* **16**, 376–388 (1999).
- [210] J. J. Zayhowski, " Q -switched operation of microchip lasers," *Opt. Lett.* **16**, 575–577 (1991).
- [211] J. J. Zayhowski and C. Dill III, "Diode-pumped passively Q -switched picosecond microchip lasers," *Opt. Lett.* **19**, 1427–1429 (1994).
- [212] J. J. Degnan, "Optimization of passively Q -switched lasers," *IEEE J. Quant. Electr.* **31**, 1890–1901 (1995).
- [213] W. Koechner, *Solid-State Laser Engineering* (Springer, Berlin, 1992).
- [214] W. A. Clarkson, P. J. Hardman, and D. C. Hanna, "High-power diode-bar end-pumped Nd:YLF laser at 1.053 μm ," *Opt. Lett.* **23**, 1363–1365 (1998).
- [215] X. Peng, L. Xu, and A. Asundi, "High-power efficient continuous-wave TEM₀₀ intracavity frequency-doubled diode-pumped Nd:YLF laser," *Appl. Opt.* **44**, 800–807 (2005).
- [216] W. A. Clarkson, "Thermal effects and their mitigation in end-pumped solid-state lasers," *J. Phys. D* **34**, 2381–2395 (2001).
- [217] P. J. Hardman, W. A. Clarkson, G. J. Friel, M. Pollnau, and D. C. Hanna, "Energy-transfer upconversion and thermal lensing in high-power end-pumped Nd:YLF laser crystals," *IEEE J. Quant. Electr.* **35**, 647–655 (1999).
- [218] A. Hakola, S. C. Buchter, T. Kajava, H. Elfström, J. Simonen, P. Pääkkönen, and J. Turunen, "CW and pulsed operation of a diode-pumped Bessel–Gauss laser", *Proc. CLEO/Europe-EQEC 2005 Int. Conf., Europhysics Conference Abstracts* **29B** (Munich, Germany, 2005), p. CA7-3-THU.

- [219] T. Y. Fan and R. L. Byer, "Diode laser-pumped solid-state lasers," *IEEE J. Quant. Electr.* **24**, 895–912 (1988).
- [220] M. Arvidsson, "Far-field timing effects with passively Q-switched lasers," *Opt. Lett.* **26**, 196–198 (2001).

Abstracts of publications I–VI

- I. Thin films of the magnetic shape-memory (MSM) material Ni–Mn–Ga have been deposited on Si(100) substrates using pulsed laser deposition. The 200–300-nm-thick films were prepared at substrate temperatures ranging from 450 °C to 650 °C and at different background Ar pressures. Large saturation magnetizations, up to 60% of the bulk value, were measured for the films. Only the films deposited in vacuum or at Ar pressures below 10^{-3} mbar and at temperatures between 500 °C and 600 °C were ferromagnetic. The films are mainly crystallized in the austenitic phase and they have a smooth surface with a low droplet density ($0.01 \mu\text{m}^{-2}$). The magnetization and surface quality are sufficient that the films could be utilized in the realization of thin-film MSM devices.
- II. We report the deposition of thin films of the magnetic shape-memory (MSM) alloy Ni–Mn–Ga on different substrates by pulsed laser deposition (PLD). Both standard semiconductors — Si and GaAs — and Ni–Mn–Ga single crystals were used. The films on silicon had a relatively smooth surface and showed large saturation magnetizations, up to 60% of the bulk value, when deposited at substrate temperatures between 500 and 600 °C. The films on GaAs, on the contrary, were non-ferromagnetic with a granular surface. In addition, preliminary results of films deposited on Ni–Mn–Ga single crystals indicate that the Ni–Mn–Ga film exhibits the same 6% strain in the magnetic field as the bulk.
- III. We discuss the preparation of thin films of the ferromagnetic shape-memory Ni–Mn–Ga alloys on NaCl using pulsed laser deposition and present a simple way to release the film from its substrate and to realize free-standing Ni–Mn–Ga structures.
- IV. With applications of pulsed laser deposition in mind, we demonstrate a simple and efficient solution for the beam-shaping problem, in which a wide, typically rectangular spatial distribution of an excimer-laser beam should be transformed into a flat-top distribution, a few mm wide in both directions.
- V. We demonstrate a simple and compact laser source that directly produces a Bessel–Gauss beam. The laser resonator consists of a diode-end-pumped Nd:YAG crystal, a planar mirror, and a diffractive mirror designed to phase-conjugate only the lowest-order Bessel–Gauss beam.
- VI. We present a simple and efficient method to convert a Gaussian laser beam into a Bessel-like beam with a long and narrow focal line by using a nematic liquid crystal with a high third-order nonlinearity.



ISBN 951-22-8282-8
ISBN 951-22-8283-6 (PDF)
ISSN 1795-2239
ISSN 1795-4584 (PDF)